ABSTRACT

Title of Dissertation: MICROSCALE STUDY OF NUCLEATION PROCESS IN BOILING OF LOW-SURFACE-TENSION LIQUIDS

Saeed Moghaddam, Doctor of Philosophy, 2006

Dissertation directed by: Associate Professor Kenneth T. Kiger
Department of Mechanical Engineering

A novel MEMS device has been developed to study some of the fundamental issues surrounding the physics of the nucleation process intrinsic to boiling heat transfer. The study was focused on boiling of FC-72 liquid.

Over the past 50 years, scientists have developed several competing mechanistic models to predict the boiling heat transfer coefficient. Although the developed models are intended to predict the heat transfer coefficient at macroscales, their fundamental assumptions lie on complex microscale sub-processes that remain to be experimentally verified. Two main unresolved issues regarding these sub-processes are: 1) bubble growth dynamics and the relative importance of different mechanisms of heat transfer into the bubble and 2) vapor/liquid/surface thermal interactions and the bubble's role in heat transfer enhancement during the nucleation process.

The developed device generates bubbles from an artificial nucleation site centered within a radially distributed temperature sensor array (with 22-40 μm spatial resolution) while the surface temperature data and images of the bubbles are recorded. The

temperature data enabled numerical calculation of the surface heat flux. Using the test results, the microlayer contribution to the bubble growth was determined to increase from 11.6% to 22% when surface temperature was increased from 80 °C to 97 °C. It was determined that the transient conduction process occurs predominantly at the bubble/surface contact area, and before the bubble departure, contrary to what has been commonly assumed in classical boiling models. For the first time, the convection heat transfer outside the contact area (often known as microconvection) and transient conduction within the contact area were differentiated. The microconvection heat flux was found to be relatively close to that of the equivalent natural convection produced by the same geometry, but becomes significantly stronger than natural convection at higher surface temperatures.

Test results under saturation conditions showed that when surface temperature is increased from 80 °C to 97 °C, the contribution of the different mechanisms of heat transfer within a circular area of diameter equal to that of the bubble changes from: 1) 28.8% to 16.3% for microlayer, 2) 45.3% to 32.1% for transient conduction, and 3) 25.8% to 51.6% for microconvection.

MICROSCALE STUDY OF NUCLEATION PROCESS IN BOILING OF LOW-SURFACE-TENSION LIQUIDS

by

Saeed Moghaddam

Dissertation submitted to the Faculty of the Graduate School of the
University of Maryland, College Park in partial fulfillment
of the requirements for the degree of
Doctor of Philosophy
2006

Advisory Committee:

Associate Professor Kenneth Kiger, Chair/Advisor
Professor Michael Ohadi, co-Advisor
Professor Avram Bar-Cohen
Associate Professor Jungho Kim
Associate Professor Reza Ghodssi

Dedication

To my late parents and my wife for their sacrifices and unconditional love

ACKNOWLEDGEMENTS

First and foremost I would like to thank my advisor Dr. Kenneth T. Kiger, whom I am indebted to for his encouragements, counsel and support throughout the course of my study and research.

I also extend my appreciation to the other members of my advisory committee who provided constructive advice and guidance, including Dr. Avram Bar-Cohen, Dr. Michael Ohadi, Dr. Jungho Kim, and Dr. Reza Ghodssi. I am grateful to Dr. Reza Ghodssi for providing me with access to his microfabrication lab and productive interactions with his team. I would also like to thank Dr. Jungho Kim, for his suggestions and interactions, and providing me with material and equipment. I greatly thank Dr. James Duncan for providing me with opportunity to use his high speed digital camera. I wish to thank Dr. Elizabeth Smela and Dr. Donald DeVoe for providing me with access to their microfabrication facilities.

Finally, I sincerely appreciate endless support and great encouragements of Mr. Tom Laughran and Mr. John Hummel throughout the years of using ECE and IREAP clean room facilities.

TABLE OF CONTENTS

LIST OF TABLES

LIST OF FIGURES

NOMENCLATURE

A	Non-dimensional factor in Eq. (2-16)
b	Bubble/boundary layer height ratio
B	Non-dimensional factor in Eq. (2-16)
C	Specific heat [J/(kg.K)]
D_b	Bubble diameter
f	Bubble departure frequency
Fo	Fourier number
g	Gravitational acceleration [m/s^2]
h	Heat transfer coefficient [$W/m^2.K$]
h_{fg}	Heat of vaporization [J/kg]
H	Heated wall thickness
Ja	Jakob number
k	Thermal conductivity [W/m.K]
n	Nucleation site density
Nu	Nusselt number
P_i	Pressure inside the bubble [Pa]
P_∞	Liquid pressure [Pa]
r	Radial coordinate
R	Bubble radius
$\dot{R}$	Bubble growth rate
R_o	Initial bubble radius

Re	Reynolds number
t	Time [sec]
t_g	Bubble growth time [sec]
T	Temperature [°C]
T_0	Initial temperature [°C]
T_∞	Bulk liquid temperature [°C]
T_{sat}	Saturation temperature [°C]

Greek Letters

α	Thermal diffusivity [m^2/s]
β	Constant in Eq. (2-11)
δ	Microlayer thickness
δ_0	Initial microlayer thickness
μ	Dynamic viscosity of fluid [Pa.s]
ν	Kinematic viscosity of fluid [m^2/s]
ρ	Density [kg/m^3]
σ	Surface tension [dyne/cm]
γ	Coefficient in Eq. (2-12)
χ	Constant factor in Table 7-1

Subscripts

b	Bubble
l	Liquid

sat	Saturation
v	Vapor
w	Wall

CHAPTER 1: INTRODUCTION

The growth in computational power and functionality of Integrated Circuits (ICs) in recent years has led to an increasing level of heat generation. Thermal management is now the limiting factor in the design of many high heat flux electronics; approaching, or even surpassing, heat fluxes on the order of 100 W/cm^2 (1 MW/m^2). Using a combination of conduction through a solid medium and subsequent heat removal through air cooling is no longer sufficient for handling this level of heat flux. The shortcomings of air cooled systems have led to an increasing demand for systems capable of meeting the emerging thermal demands. Nucleate boiling has been considered as a strong candidate for meeting the emerging demands. Boiling heat transfer is one the most efficient mechanisms of heat transfer for three main reasons. First, prior empirical studies have shown that relatively high heat transfer coefficients could be achieved in boiling process. Second, the fluid volume in a two-phase system can be significantly less than in a single phase system due to the latent heat contribution in energy transfer. Third, heat absorbed by the bulk liquid is eventually released as latent heat during the phase change process and prevents an increase in bulk fluid temperature beyond the equilibrium saturation point. In contrast, in a single phase liquid system, the bulk liquid temperature continuously increases as heat gets absorbed by the liquid.

Nucleate boiling is a complex heat transfer process that has been studied for more than half a century. The problems that contribute to its complexity are the nucleation, growth, and detachment of the individual bubbles, as well as their collective behavior. The ability to predict the nucleate boiling heat transfer rate for any combination of

surface and liquid depends on having a knowledge of the four following factors,

1- The number of active nucleation sites on the surface
2- Dynamics of the bubble formation and departure at these sites
3- The heat transfer associated with the nucleation, growth, and detachment of the individual bubbles underneath and at the vicinity of the bubble
4- The heat transfer associated with interactions between the bubbles

These fundamental sub-processes of boiling have been the subjects of numerous studies throughout the topic's history and numerous models have been developed to explain their nature. Many analogies have been presented to explain the collective behavior of the boiling process and to develop correlations that can predict the boiling heat transfer coefficient.

In spite of the vast amount of effort devoted to boiling studies, there is still no definitive, comprehensive explanation for the actual mechanism of bubble nucleation, growth, and departure that controls the heat transfer field in the vicinity of the nucleation site. Lack of experimental data concerning the details of these processes have caused continuous proliferation of models and unresolved issues. In a growing effort in recent years, scientists have tried to resolve these issues by experimental and numerical study of the bubbling process. Unfortunately, only a handful of experimental data are available due to the difficulties of making quantitative observations of the essential microscale dynamics. The goal of this dissertation is to study the dynamics of bubble formation and its associated heat transfer mechanisms throughout the bubble formation and detachment processes. This study is conducted through fabrication of a MEMS device that can

generate single bubbles and measure the surface temperature and heat flux directly underneath and around the bubble. The experimental results will then be used to analyze shortcomings of the existing bubble growth models and analogies/models developed for predicting the surface heat transfer. The heat transfer models have been commonly used on large boiling surfaces which simultaneously generate numerous bubbles. But, their development has been solely based on assumptions concerning the heat transfer processes involved in single bubble boiling and they do not have built-in mechanisms to model the heat transfer processes resulted from interactions between the bubbles. The utility of the current work, therefore, is in testing the fundamental mechanistic assumptions upon which the models are based, while ignoring higher order effects due to multiple bubbles interactions.

The selection of the fluid in this study was motivated by the requirements of electronic cooling applications. Proximity of the cooling system to the electronics dissuades the use of electrically conductive fluids. In addition, in applications such as personal computers (PCs) and laptops, which have close contact with humans, the use of toxic, flammable, and high pressure fluids raises serious safety concerns. These limitations automatically disqualify a majority of fluids with an inherent high boiling performance. A general list of the desired liquid properties for most electronic cooling applications should include:

- proper heat transfer properties
    - high thermal conductivity
    - large heat of vaporization
- dielectric

- non-toxic
- non-flammable
- dielectric
- non-corrosive
- proper working temperature and pressure
    - Operation of a system at atmospheric pressure improves its safety and reliability and reduces its manufacturing cost
- low freezing point
- environment friendly
    - low Ozone Depletion Potential (ODP)
    - low Global Warming Potential (GWP)
    - low Atmospheric Life Time (ALT)

In recent years, 3M^{TM} electronic liquids have emerged as strong candidates that can satisfy the majority of the above requirements. In a two-phase system, it is desirable to use a liquid with a boiling temperature sufficiently above the ambient temperature (30-35 °C) to allow the cooling system to deposit heat into the ambient without using a heat pump cycle. The boiling temperature should also be sufficiently below the junction temperature (85-125 °C) to allow heat removal from the semiconductor. Considering these two bounding temperatures, a limited number of 3M^{TM} electronic liquids can be used for a two-phase system. Table 1-1 lists thermophysical properties of some of these liquids. As can been seen in the table, liquids FC-72 and HFE-7100 with boiling temperatures of 56 °C and 61 °C, respectively, are good candidates for this application.

The second chapter of this thesis provides an overview of the existing knowledge available in the literature about the formation and growth process, and the associated heat transfer mechanisms, that are essential to nucleate boiling. The discussions provided in chapter 2 are focused on the sub-processes that define the bubble dynamics. The effect of different analogies on the heat transfer field of the bubble and its surrounding environment will be discussed. Within this context, a review of the existing boiling models will be presented and their fundamental assumption will be analyzed. The third chapter presents different design aspects of the MEMS device to study some of the outstanding issues in boiling process discussed in chapter 2. Details design, microfabrication, and packaging of the sensor and test setup are presented in chapters 3 to 5. The test results and their analysis are provided in chapter 6. Chapter 7 provides the comparison of the experimental results with the boiling literature.

Table 1-1: Thermophysical properties of some of the 3M^{TM} fluorinert liquids.

	FC-87	HFE-7000	FC-72	HFE-7100	FC-84	FC-3283	FC-40	FC-43	FC-70
Boiling Point (°C)	30	34	56	61	80	128	155	174	215
Thermal Conductivity (W/m.K)	0.056	0.075	0.057	0.061	0.06	0.066	0.066	.065	.07
Heat of Vaporization (kJ/kg)	103	142	87.9	125.6	79.5	78	71.2	71.2	69
Specific Heat (J/kg.K)	1100	1300	1100	1214	1100	1100	1100	1100	1100
Surface Tension (dynes/cm)	9	12.4	12	13.6	13	___	16	16	18
Viscosity (cSt)	0.27	0.32	0.4	0.32	0.55	0.75	2.2	2.5	12

CHAPTER 2: EXISTING BOILING THEORIES

Within this chapter, a survey of the existing knowledge in boiling literature concerning the bubble growth and heat transfer mechanisms during the boiling process is provided. The survey is intended to evaluate the fundamental assumptions of the existing models and their ability to predict the experimental results. A general description of the boiling process and associated heat transfer events is provided. The review of the bubble growth studies is started with the simplified case of a spherical vapor bubble in an infinite liquid pool (homogenous bubble growth). This is followed by highlighting the similarities and differences between the homogeneous and heterogeneous bubble growth mechanisms. The two existing theories concerning the heterogeneous bubble growth, including growth due to heat transfer through the relaxation layer and through microlayer evaporation, are presented. The fundamental assumptions of the existing models for predicting the surface heat transfer during the nucleation process are reviewed and their differences are discussed.

2-1- Boiling Heat Transfer

Formation of bubbles at the interface of a heated wall and liquid results to a mode of heat transfer called boiling. Boiling takes place in different regimes, depending on the wall superheat temperature (difference between the wall and the liquid temperatures). Figure 2-1 shows a typical boiling curve for nucleate boiling on a horizontal surface (gravitational body force is normal to the heated wall, in the direction opposite to the surface normal vector). As the wall superheat temperature is increased, natural

convection is the first mode of heat transfer that occurs. At a certain value of the wall superheat, bubbles start to form on the surface. Formation of the bubbles is associated with a sudden increase of the heat transfer coefficient at the surface. The cumulative effect of individual bubble formation across the surface establishes a regime of heat transfer that is called the partial nucleate boiling regime (region II in Figure 2-1). In this boiling regime, interactions between the neighboring bubbles are considered to be minimal. Further increase of the surface superheat temperature results in an increase in the number of bubbles (i.e. activation of more nucleation sites) and their departure frequency. The increased bubble density and frequency leads to interactions between the bubbles. This interaction appears in the form of bubble mergers and formation of vapor columns that are characteristics of the fully developed boiling regime (region III in Figure 2-1). This regime is considered to be the upper operating margin for all practical boiling applications. The upper limit of this regime is called critical heat flux (point “c”) at which the surface temperature becomes unstable and quickly proceeds to film boiling, if the surface temperature isn’t actively controlled. This is due to the generation of a significant amount of vapor at the surface of the heated wall that reduces the flow of liquid towards the surface. At the film boiling regime, a vapor blanket covers the surface and heat transfer from the surface takes place primarily through conduction and radiation via the vapor medium.

The importance of boiling in thermal systems has been an incentive for the heat transfer community to study the nature of this phenomenon for more than half a century. Since bubble nucleation is the fundamental element of the boiling heat transfer process, it has become the focus of many studies. The primary goal of these studies has been to

construct boiling heat transfer models based on the physical sub-processes associated with the bubbling events. Although the developed models are intended to predict the heat transfer coefficient at macroscales, their fundamental assumptions are founded on complex microscale sub-processes that remain to be experimentally verified. Two main unresolved issues regarding these sub-processes are: 1) the dynamics of bubble growth and associated heat transfer processes and 2) the bubble's role in surface heat transfer during the boiling process.

Survey of the prior studies on the bubble growth along with studies on bubble role in the overall boiling heat transfer from the surface are presented in the following sections. It has been tried to limit the discussions about these studies to their main

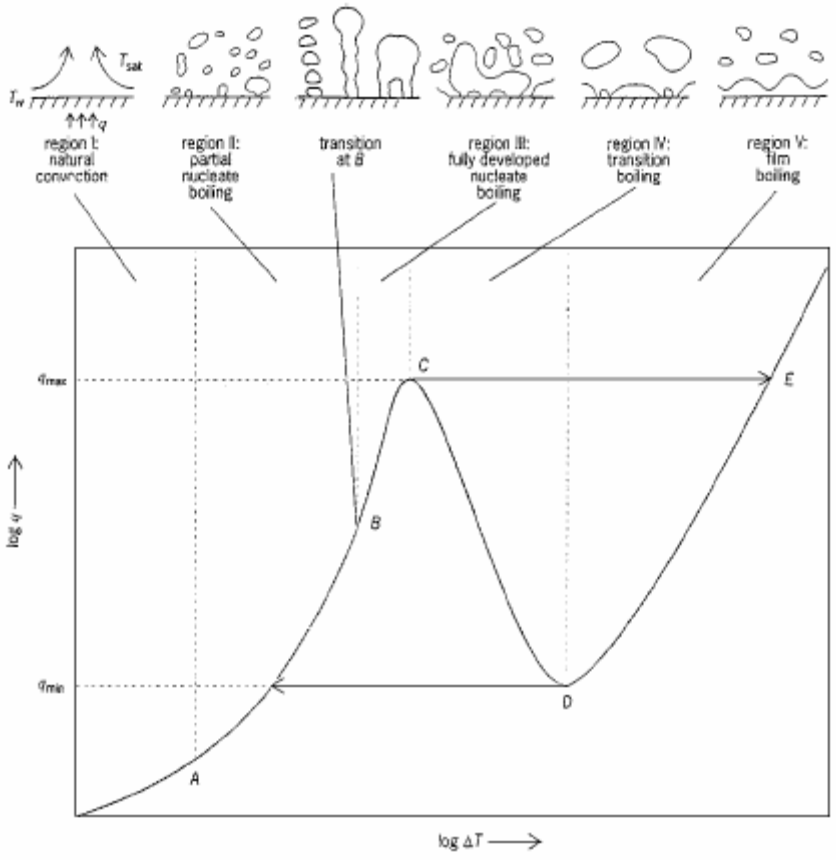

Figure 2-1: Boiling regimes at different surface superheat temperatures (Dhir (1998)).

analogy and fundamental assumptions. Further discussions about the developed models/correlations and their evaluation will be presented in later chapters when the experimental data are discussed.

2-2- Bubble Growth Mechanism

2-2-1- Bubble Growth in Infinite Liquid Pool

The existing knowledge on bubble growth in an infinite pool of liquid has been established since Rayleigh (1917) presented the first model for growth of a bubble in an inviscid, incompressible, and infinitely extended liquid:

$$\frac{1}{2R^2\dot{R}}\frac{d}{dt}\left(R^3\dot{R}^2\right)=R\ddot{R}+\frac{3}{2}\dot{R}^2=\frac{P_i-P_\infty}{\rho_l} \tag{2-1}$$

This equation shows a balance between inertia ($R\ddot{R}+\frac{3}{2}\dot{R}^2$) and pressure ($P_i-P_\infty$) forces during the bubble growth (P_i is pressure at the vapor/liquid interface). For the special case of constant pressure term, Rayleigh (1917) arrived at the following solution for Equation 2-1.

$$\dot{R}(t)=\left\{\frac{2\Delta P}{3\rho_l}\left[1-\left(\frac{R_0}{R}\right)^3\right]\right\}^{1/2} \tag{2-2}$$

For the asymptotic case of $R/R_0\to\infty$, where in R_0 is the initial bubble radius, solution simplifies to the following form

$$R(t)\cong\left(\frac{2\left(P_i-P_\infty\right)}{3\rho_l}\right)^{1/2}t \tag{2-3}$$

The growth of a bubble in a superheated liquid was first studied by Bosnjakovic

(1930) and Fritz and Ende (1936). They assumed that the heat required for liquid evaporation at the bubble/liquid interface is supplied by conduction through a thermal boundary layer surrounding the bubble (see Figure 2-2). Following equation represents this analogy.

$$\rho_v h_{fg} \frac{dR}{dt} = h\left(T_\infty - T_i\right) \tag{2-4}$$

where in T_∞ and T_i are liquid and vapor/liquid interface temperatures, respectively, and h is the heat transfer coefficient. They suggested that since the thermal boundary layer thickness is small compared to the bubble radius, heat transfer to the interface can be approximated using the solution of transient heat conduction in a semi-infinite solid. They also assumed that the vapor/interface is at saturation temperature. Using these simplification results in the following expression for the bubble growth rate.

$$h\left(T_\infty - T_i\right) = k\left(\frac{\partial T}{\partial r}\right)_{r=R} \cong k\frac{T_\infty - T_{sat}}{\sqrt{\pi\alpha t}} \tag{2-5}$$

$$R(t) \cong \frac{2}{\pi^{1/2}} Ja\left(\alpha t\right)^{1/2} \tag{2-6}$$

Solutions of Rayleigh (1917) and Bosnjakovic (1930) and Fritz and Ende (1936) for bubble growth represented two limits of the bubble growth process that are now commonly known as *inertia-controlled* and *heat transfer-controlled* regimes. It is widely argued that at the early stages of the bubble growth, when bubble is very small, its growth is primarily limited by the inertia of the surrounding liquid (i.e. *inertia-controlled regime*) whereas growth of a large bubble is limited by heat transfer to the bubble from its surrounding liquid (i.e. *heat transfer-controlled regime*). Note that Equation 2-6 suggests

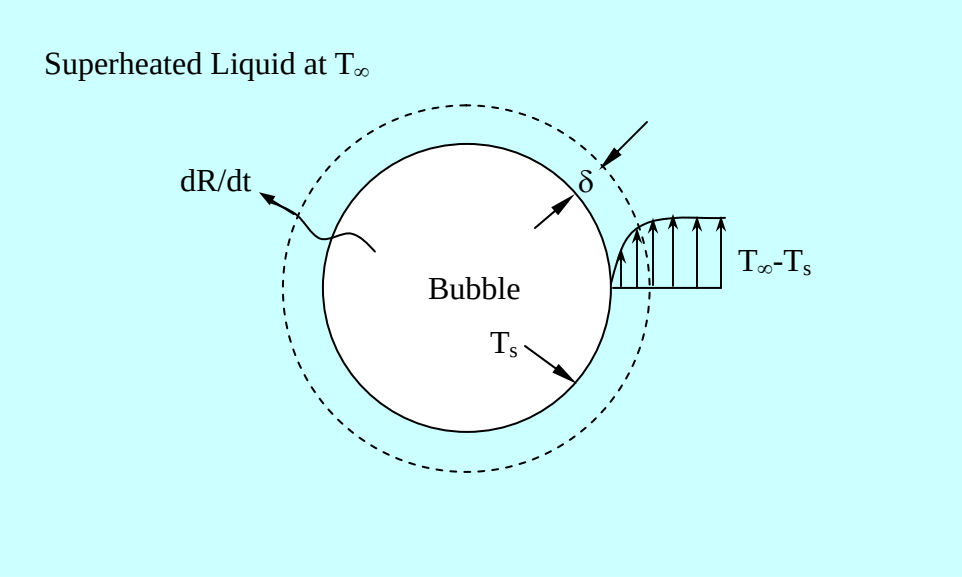

Figure 2-2: Growth of a bubble in a superheated pool of liquid.

that $R \sim t^{1/2}$, which is characteristics of heat diffusion, and Equation 2-3 suggests that $R \sim t$.

Forster and Zuber (1954) and Plesset and Zwick (1954) presented the first analysis of the bubble growth in a superheated liquid that incorporated both momentum and energy transfer effects. They started their solution with the *Extended Rayleigh* equation (presented by Plesset (1949)) as follows

$$R\ddot{R} + \frac{3}{2}\dot{R}^2 = \frac{1}{\rho_l}\left[\left(P_v(t) - P_\infty\right) - \frac{2\sigma}{R} - \frac{4\mu\dot{R}}{R}\right] \tag{2-7}$$

where in P_v is pressure inside the bubble and $2\sigma/R$ and ($4\mu\dot{R}/R$) are surface tension and viscosity forces, respectively. They neglected the viscous term due to its relatively small value and used the Clausius-Clapeyron equation to relate the pressure term ($P_v - P_\infty$) to the bubble excess temperature ($T_v - T_\infty = \Delta T_b$). They developed different models to determine ΔT_b. In both models, they assumed that the decrease in temperature from T_v to

T_∞ at the bubble boundary takes place in a layer of liquid adjacent to the bubble that has a small thickness compare to the bubble radius. They argued that the approximation of the "thin thermal boundary layer" is justified physically because the thermal diffusivity of the liquid is small. Forster and Zuber (1954) approximated ΔT_b by solving the governing heat-conduction equation in spherical coordinates, in which the liquid evaporating at the bubble wall was considered as a spherically distributed heat sink. The solution of this problem is simply given by the well-known Green's function for the domain (see Carslaw and Jaeger (1946)).

$$\Delta T_b = -\frac{\rho_v h_{fg}}{\rho_l C_l (\pi\alpha)^{1/2}} \int_0^t \frac{R(t')\dot{R}(t')}{R(t)(t-t')^{1/2}} \times \left\{ \exp\left[-\frac{(R-R')^2}{4\alpha(t-t')} \right] - \exp\left[-\frac{(R+R')^2}{4\alpha(t-t')} \right] \right\} dt' + (T_0 - T_\infty) \tag{2-8}$$

where in T_0 is the initial temperature of the bubble (with an initial radius of R_0). Forster and Zuber (1954) argued that the second exponential term under the integral is very small (compared to 1) in the entire interval of integration, while the first exponential term and $R(t')/R(t)$ are close to unity. They integrated the simplified equations numerically to determine the bubble growth during the inertia-controlled regime. They also determined an asymptotic solution for the later bubble growth stage, at which both $R\ddot{R}$ and $\dot{R}^2 \sim 1/t$ and $1/R \sim 1/t^{1/2}$ approach to zero as $t \to \infty$ and hydrodynamics no longer controls the bubble growth:

$$R(t) \cong \pi^{1/2} Ja(\alpha t)^{1/2} = 1.77\, Ja(\alpha t)^{1/2} \tag{2-9}$$

Plesset and Zwick (1952) solved the energy equation to determine ΔT_b:

$$\frac{\alpha}{r^2}\frac{\partial}{\partial r}\left(r^2\frac{\partial T}{\partial r}\right)=\frac{\partial T}{\partial t}+\frac{R^2}{r^2}\frac{dR}{dt}\frac{\partial T}{\partial r} \tag{2-10}$$

with initial and boundary conditions:

$$T(r,0)=T_\infty$$

$$4\pi R^2 k\left(\frac{\partial T}{\partial r}\right)_{r=R(t)}=h_{fg}\frac{d}{dt}\left[\frac{4}{3}\pi R^3\rho_v(T_s)\right]$$

$$T(r,t)\to T_\infty \qquad as \qquad r\to\infty$$

Through some simplifying assumptions in solving Equation 2-10, Plesset and Zwick (1952) arrived at the following expression for ΔT_b:

$$\Delta T_b \cong -\frac{R_0^2\alpha^2}{A}\frac{2\gamma(1-\beta^2)}{\beta(3\beta^2+1)}e^{\alpha\beta t} \tag{2-11}$$

The constant β is the root of equation $\beta^2+3\mu(\pi\beta)^{1/2}-1=0$ and $\gamma=Aa/\alpha^2R_0^2k$, where A stems from the assumption $P_v(t)-P_\infty=A\rho_l\Delta T_b$ in the model. Also, a is the strength of a constant heat source per unit volume considered in the solution to initiate the growth of the bubble form its unstable equilibrium. Plesset and Zwick's (1954) solution suggested that the forced growth of a bubble away from the equilibrium has an exponential behavior as follows

$$R\cong R_0\left\{1+\frac{2\gamma}{\beta(3\beta^2+1)}e^{\alpha\beta t}\right\} \tag{2-12}$$

They determined the following asymptotic solution for the bubble growth at its later stage.

$$R(t)\cong\left(\frac{12}{\pi}\right)^{1/2}Ja(\alpha t)^{1/2}=1.95Ja(\alpha t)^{1/2} \tag{2-13}$$

As can be seen, Equations 2-9 and 2-13 are very similar except for a difference of approximately 10% in their constant coefficients. Forster and Zuber (1954) and Plesset and Zwick (1954) showed that their asymptotic solution (heat transfer-controlled) can closely predict the experimental data of Dergarabedian (1953) for water at atmospheric pressure and superheat of less than 5 °C. Dalle Donne and Ferranti (1975) solved the complete set of the governing differential equations (Equations 2-7 without the viscous term and Equation 2-10) by numerical integration and found their results in close agreement with Plesset and Zwick (1954) solution for heat transfer-controlled regime (Equation 2-13).

Scriven (1959) extended the energy equation to establish the effect of radial convection resulting from unequal phase densities:

$$\frac{\alpha}{r^2}\frac{\partial}{\partial r}\left(r^2\frac{\partial T}{\partial r}\right)=\frac{\partial T}{\partial t}+\left(1-\frac{\rho_v}{\rho_l}\right)\frac{R^2}{r^2}\frac{dR}{dt}\frac{\partial T}{\partial r} \tag{2-14}$$

His solution for the governing equations suggested that at moderate to high superheats (large Jakob numbers), the thin film boundary layer assumption is valid, but at large vapor densities and small liquid superheats (small Jakob numbers) the Plesset and Zwick (1954) and Forster and Zuber (1954) models have considerable error. He determined the exact form given by Plesset and Zwick (1954) for the limiting case of large Jakob numbers, and suggested the following expression for small Jakob numbers:

$$R(t)=\left(2Ja\alpha t\right)^{1/2} \tag{2-15}$$

Although the expression of Scriven (1959) shows the same dependence of the bubble growth on time as of the Plesset and Zwick (1954) and Forster and Zuber (1954), it shows a different dependency of bubble growth on Jakob number. Riznic et al. (1999)

suggested that bubble growth follows Equation 2-13 for $Ja > 2$ and Equation 2-15 for $Ja < 2$.

In an effort to provide a single correlation that could cover both inertia- and heat transfer-controlled growth regimes, Mikic et al. (1970) obtained an expression by interpolating between the limiting solutions for large and small times given by Equations 2-3 and 2-13. They presented their correlation in the form of scaled radius and time variables:

$$R^+ = \frac{2}{3}\left[\left(t^+ + 1\right)^{3/2} - \left(t^+\right)^{3/2} - 1\right] \tag{2-16}$$

where the scaled variables are given by

$$R^+ = \frac{RA}{B^2},\ t^+ = \frac{tA^2}{B^2}, B = \left(\frac{12\alpha_l}{\pi}\right)^{1/2} Ja, \text{ and } A^2 = \frac{bh_{fg}\rho_v\left(T_w - T_{sat}\right)}{\rho_l T_{sat}} \text{ with } b = \frac{2}{3}$$

Mikic et al. (1970) model (also known as MRG model) is simply an interpolation formula that bridges the gap between the two limiting regimes, and is not a solution to the governing equation at the intermediate stage. Therefore, there is no physics built into the model for the transition period between the two limits. Mikic et al. (1970) found their model in good agreement with Lien (1969) experimental data in uniformly superheated water at the later, but not at the initial stage of the bubble growth. Also, since they used the limiting solution of Plesset and Zwick (1954) for the heat transfer-controlled regime, the range of applicability of their model is limited to that of the Plesset and Zwick (1954). Shortly after Mikic et al. (1970) presented their model, Theofanous and Patel (1976) found that evaluation of $\Delta P_v / \Delta T_b \equiv dP_v / dT_b$ at $T_{sat}\left(P_\infty\right)$ in using Clausius-Clapeyron equation (as in MRG model) results in an underestimation of the bubble pressure during

the early growth stage. Figure 2-3 depicts a qualitative representation of the Theofanous and Patel's (1976) argument.

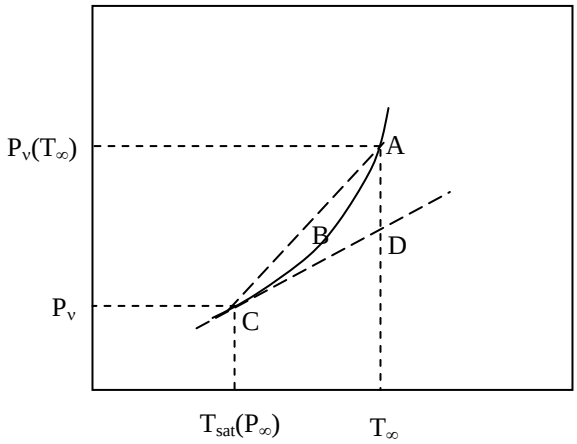

Figure 2-3: Qualitative comparison of using two different slopes A-C and D-C for calculating the pressure term using Clausius-Clapeyron equation.

The ABC curve represents the vapor pressure curve. Point "A" represents the initial state of the vapor/bubble and point "C" represents the final state. During the bubble growth, the vapor state monotonically changes from "A" to "C". The line DC is the type of linearization utilized in the MRG solution. As can be seen in Figure 2-3, the DC line always underestimates the vapor pressure. This leads to underestimation of the bubble growth rate within the inertia-controlled regime. Theofanous and Patel (1976) used the following approximation for evaluation of dP_v/dT_b .

$$dP_v/dT_b \cong \left(P_v\left(T_\infty\right) - P_\infty\right)/\left(T_\infty - T_{sat}\left(P_\infty\right)\right) \tag{2-17}$$

Theofanous and Patel (1976) found that this approximation substantially improves the ability of the MRG model in predicting the growth rate at the early growth stages. They found a close agreement between the results of the modified model, results of the numerically solved set of equations, and their experimental data for water, sodium, and

refrigerants R11 and R113. Later, Prosperetti and Plesset (1978) endorsed the Theofanous and Patel's (1976) modification and suggested further modifications to the Mikic and Rohsenow (1970) model by introducing scaled variables to describe the growth under any conditions. Prosperetti and Plesset (1978) noted that the scaled description is not valid during the very early (prior to inertia-controlled dominancy), surface-tension-dominated, portion of the growth.

In order to examine the simplification assumptions introduced in the aforementioned models, several numerical studies (i.e. numerically solving the governing equations) were conducted by Dalle Donne and Ferranti (1975), Lee and Merte (1996), and Robinson and Judd (2001, 2004). Lee and Merte (1996) found an excellent agreement between their results and the numerical results of Dalle Donne and Ferranti (1975). They also compared their results with the existing analytical models and found an excellent agreement with Mikic et al.'s (1970) model. Figure 2-4 shows this comparison. They noted that although use of Clausius-Clapeyron equation in the Mikic et al.'s (1970) model results to 39% error at the very early portion of the inertia-controlled regime, it can successfully predict the later bubble growth stages. They found that the modified solution of Prosperetti and Plesset (1978) always overestimates the bubble size considerably. Lee and Merte (1996) selected a wide range of experimental data from different liquids and superheat levels and compared them with the model of Mikic et al. (1970) and the asymptotic solutions of Rayleigh (1917) and Plesset and Zwick (1954). As can be seen in Figure 2-5, they found Mikic et al.'s (1970) model in excellent agreement with the experimental data shown in the figure.

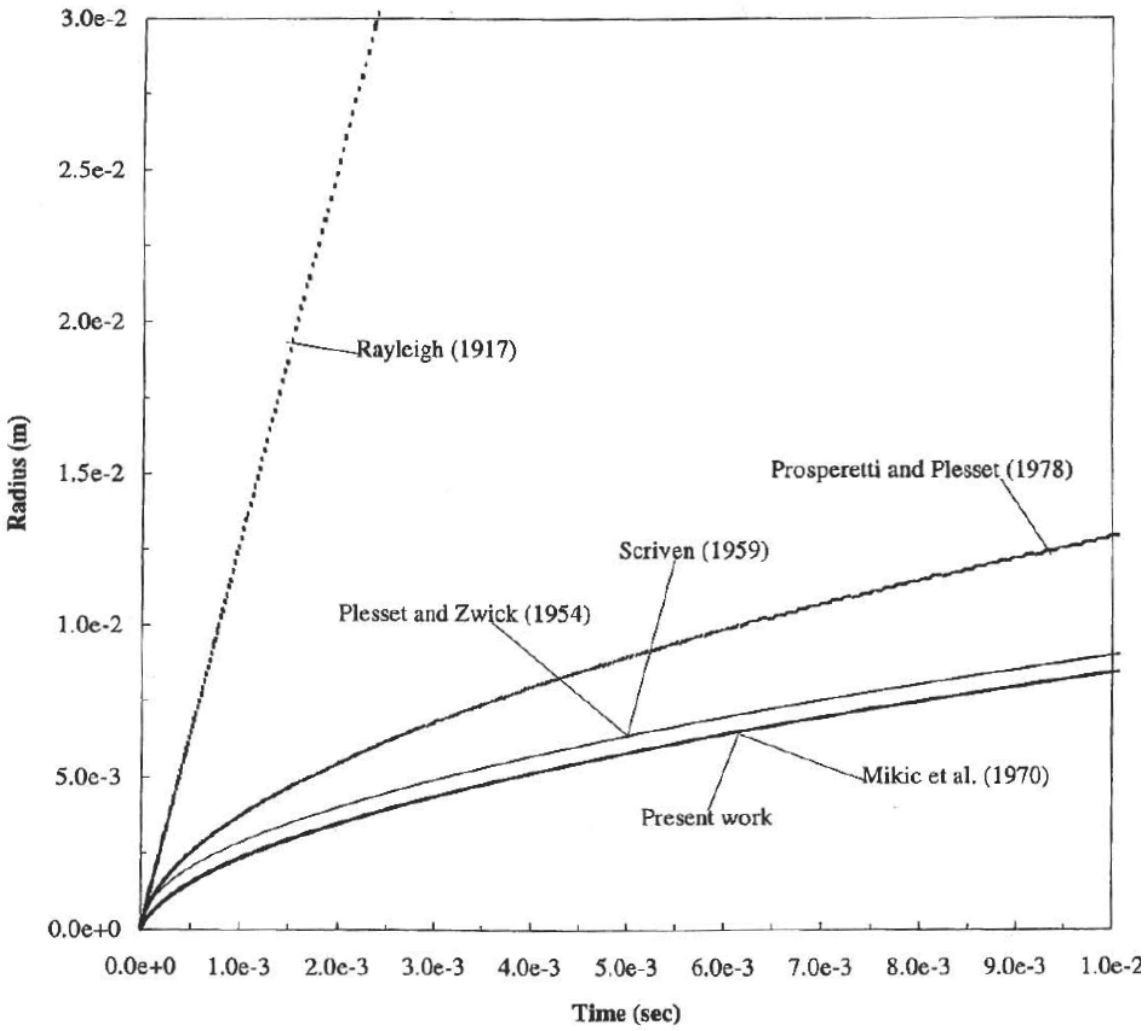

Figure 2-4: Comparison of the Lee and Merte (1996) numerical results for bubble growth with different models (Lee and Merte (1996)).

2-2-2- Heterogeneous Nucleation Process

The growth of a bubble on a heat transfer surface (heterogeneous nucleation) can be considered as one of the most complicated aspects of the boiling process. As a result, heterogeneous nucleation is not understood nearly as well as the bubble growth in an infinite liquid pool. The existence of the heating surface in heterogeneous bubble growth leads to:

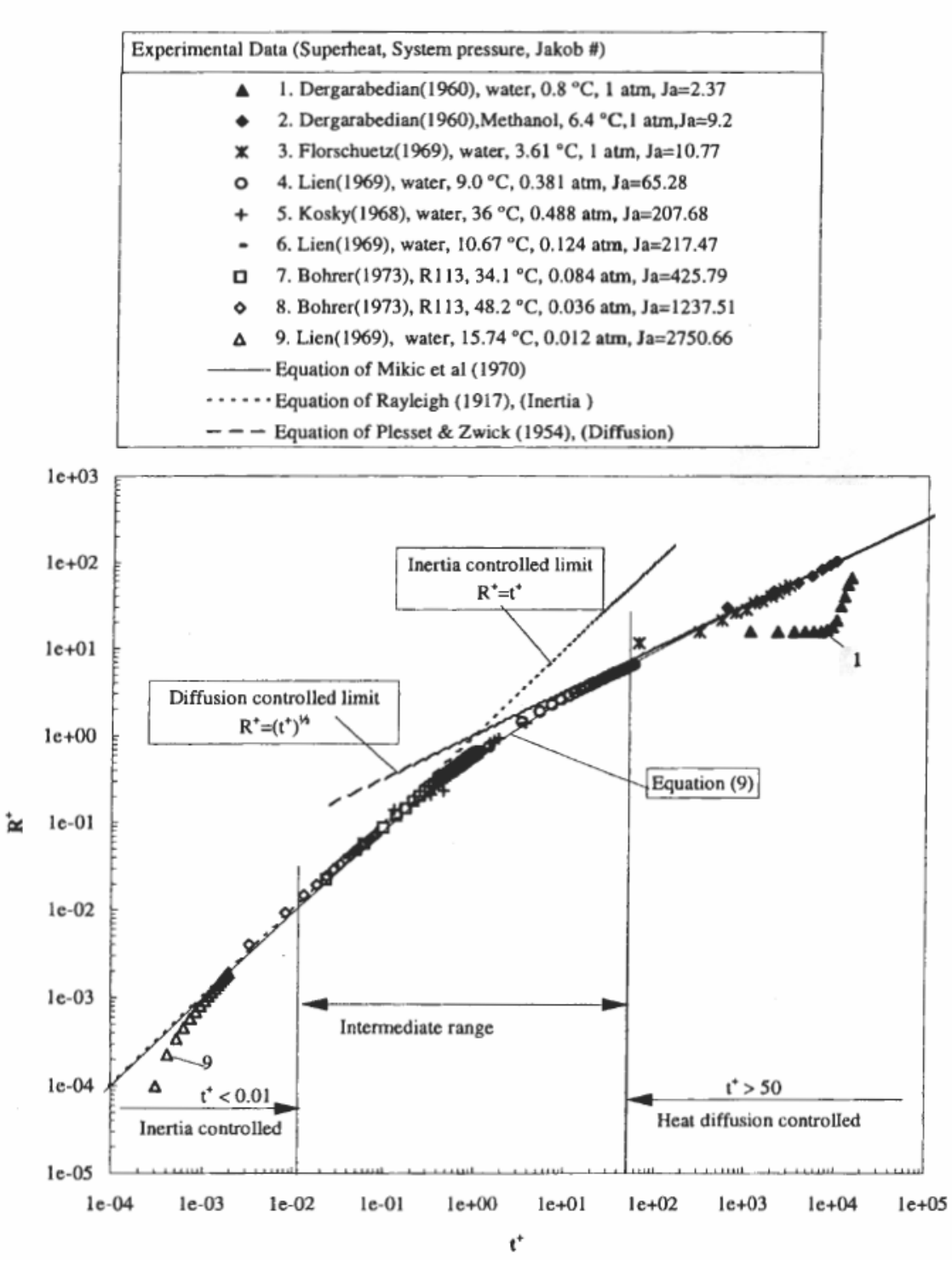

Figure 2-5: Comparison of the Mikic et al. (1970) model and asymptotic solutions of Rayleigh (1917) and Plesset and Zwick (1954) with experimental data (Lee and Merte (1996)).

1- The lack of spherical symmetry

2- The presence of non-uniform temperature field surrounding the bubble

3- The formation and evaporation of a thin liquid film under the bubble known as the microlayer

The lack of understanding of the physics of these contributing factors has made it very difficult to predict the bubble growth in the heterogeneous boiling process. Aside from the modeling difficulties, significant issues exist on the way of conducting controlled experiments with known thermal conditions around the bubble. This has made the examination of the developed theories and their fundamental assumptions a difficult task. In a practical boiling case, natural convection and liquid motion induced by neighboring bubbles alter the bubble growth conditions. Due to the rapidly varying temperature and flow fields, scatter is observed in the available bubble growth data. This makes comparison with theoretical expressions very difficult because of the uncertainty involved in matching the initial and boundary conditions.

Numerous studies have been conducted in the past to understand the physics of the heterogeneous bubble growth. Johnson et al. (1966) provided images of bubbles generated under a wide range of conditions on a heated wall. They classified the bubbles shapes as spherical, hemispherical, and oblate. Johnson et al. (1966) suggested that the bubble shape at any moment of its growth process is determined by relative magnitude of inertia and surface tension forces. If the inertia term predominates, as in the case of a rapidly growing bubble, the bubble growth will be nearly hemispherical. If the surface tension force predominates, bubble tends towards the spherical shape. It is commonly expressed in the literature that at high superheat temperatures, bubble exhibits explosive/inertia-controlled growth. Surface tension forces are considered to play an

important role at low superheat temperatures. Johnson et al. (1966) noted that all bubbles finally approach a spherical shape before departure, regardless of their initial shape. Study of the Johnson et al. (1966) is of important value, since it is a prerequisite for any modeling of heat transfer to a growing bubble, as will be discussed later in this section.

2-2-2-1- Bubble Growth Due to Heat Transfer from Relaxation Layer

Bubble growth in a non-uniform temperature field was first considered by Griffith (1958), Savic (1958), and Bankoff and Mikesell (1958). The main approach in their analysis has been to define several complex geometrical factors that can accommodate for heat transfer into a non-spherical bubble surrounded by a non-uniform superheated liquid layer (see Figure 2-6). Their solutions for bubble growth have often led to complex expressions that are impractical to use. The complexity of the provided solutions has prompted some authors to consider more simplified models. Cole (1966) accounted for non-uniformity of the temperature by using half of the wall actual superheat in the formula for bubble growth in a uniformly superheated liquid.

In another approach, Mikic and Rohsenow (1969) determined the temperature profile of the liquid adjacent to the wall during the waiting period, and then used that subsequently to calculate the heat transfer into the bubble when the bubble growth is initiated. They avoided the complexity of using several geometrical factors introduced in

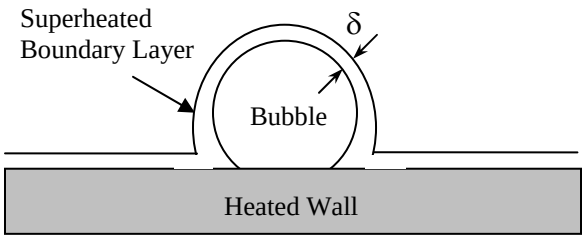

Figure 2-6: A schematic of bubble and its surrounding environment during the growth process.

the Han and Griffith model (1965) by providing a 1D approximation for the entire heat conduction process. Based on this model, heating of the liquid starts at $t = -t_w$, which is defined as the beginning of the waiting period. During this period, the temperature distribution in the liquid is determined through solution of the 1D heat diffusion equation describing transient conduction into a semi-infinite body:

$$\frac{\partial^2 T}{\partial^2 y} = \frac{1}{\alpha}\frac{\partial T}{\partial t} \tag{2-18}$$

with the initial and boundary conditions:

$$T(y,-t_w) = T_\infty$$

$$T(0,t) = T_w \;\&\; T(\infty,t) = T_\infty \text{ at } -t_w \le t < 0 \tag{2-19}$$

At the second stage of the process, when a bubble forms on the surface ($t > 0$), heat transfers from the semi-infinite body of liquid to the bubble/liquid interface that is taken to be at $T_{sat}(P_\infty)$. Boundary conditions in this case corresponds to

$$T(0,t) = T_{sat}(P_\infty) \;\&\; T(\infty,t) = T_\infty \text{ at } t > 0 \tag{2-20}$$

Mikic and Rohsenow (1969) determined the following solution for Equation 2-18 with boundary conditions 2-19 and 2-20 at $t > 0$.

$$T(y,t) - T_\infty = (T_w - T_\infty)\,erfc\left[\frac{y}{2\sqrt{\alpha(t+t_w)}}\right] - (T_w - T_{sat})\,erfc\left[\frac{y}{2\sqrt{\alpha t}}\right] \tag{2-21}$$

Heat flux at the bubble/liquid interface was then determined by taking the first derivative of the temperature profile at the bubble/liquid interface, giving:

$$\left(\frac{q}{A}\right)_{x=0} = k\left(\frac{\partial T}{\partial x}\right)_{x=0} = k\left\{\frac{T_w - T_{sat}}{\sqrt{\alpha\pi t}} - \frac{T_w - T_\infty}{\sqrt{\alpha\pi(t+t_w)}}\right\} \tag{2-22}$$

Since the developed model was one dimensional, Mikic and Rohsenow (1969) modified Equation 2-22 by multiplying it by a correction factor. They also argued that when the waiting time approaches infinity, the heat flux should approach the value corresponding to a bubble growth in a uniformly heated liquid. Using the result of Plesset and Zwick (1954), they suggested a correction coefficient of $\sqrt{3}$ and derived the following expression for the bubble growth rate.

$$\rho_v h_{fg} \frac{dR}{dt} = \sqrt{3}k\left\{\frac{T_w - T_{sat}}{\sqrt{\alpha\pi t}} - \frac{T_w - T_b}{\sqrt{\pi\alpha\left(t + t_w\right)}}\right\} \tag{2-23}$$

and after integration (using $R = 0$ at $t = 0$):

$$R = \left(\frac{12}{\pi}\right)^{1/2}\left\{1 - \frac{T_w - T_\infty}{T_w - T_{sat}}\left[\left(1 + \frac{t_w}{t}\right)^{1/2} - \left(\frac{t_w}{t}\right)^{1/2}\right]\right\} Ja\sqrt{\alpha t} \tag{2-24}$$

Note that if $t_w = 0$ and $T_\infty = T_{sat}$, Equation 2-24 predicts that $R = 0$ and when $t_w \to \infty$ it approaches to the Plesset and Zwick (1954) correlation (Equation 2-13) for homogeneous bubble growth. Mikic and Rohsenow (1970) compared their model with the experimental results of Han and Griffith (1965) for water with a wall superheat of $T_w - T_{sat} = 10$ °C with a subcooled of about $T_{sat} - T_\infty = 4$ °C. Although their model closely followed the experimental results in the early growth stage, it underpredicted the bubble diameter at the later bubble growth stage by an average of about 20%. In a later study, Mikic and Rohsenow (1970) suggested that their developed model for homogenous bubble growth (Equation 2-16) is also valid for heterogeneous bubble growth, provided $b = \pi/7$ is used in the expression for A in Equation 2-16. They didn't compare their model with experimental data.

Van Stralen et al. (1975) suggested that the superheated liquid adjacent to the surface is normally thin and doesn't necessarily cover the entire bubble. Figure 2-7 depicts the Van Stralen et al. (1975) analogy.

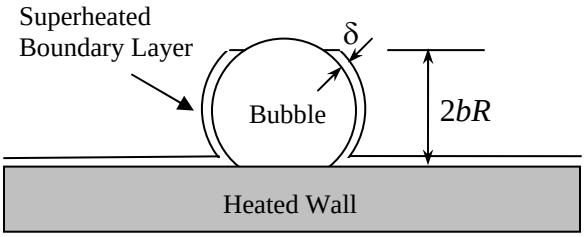

Figure 2-7: A schematic representing the Van Stralen (1966) analogy for the superheated liquid around a bubble.

Van Stralen et al. (1975) multiplied the growth correlation of Plesset and Zwick (1954) by correction factor b:

$$R(t) \cong \left(\frac{12}{\pi}\right)^{1/2} bJa(\alpha t)^{1/2} \tag{2-25}$$

They also suggested a time-dependent Ja number as follow

$$Ja = \frac{\rho_l c_l (T_w - T_{sat})}{\rho_v h_{fg}} \exp - \left(\frac{t}{t_g}\right)^{1/2} \tag{2-26}$$

where in t_g is the growth period of the bubble. Van Stralen et al. (1975) suggested that b is time-independent. They suggested $b = 0.794$ for hemispherical and $b \leq 1$ for spherical bubbles, respectively. They didn't compare their model with experimental data.

As one might have realized up to this point of discussion, both of the discussed models only treat the energy equation and don't incorporate the motion/momentum equation. As was pointed out in the previous section for the homogeneous bubble growth, during the early portion of the growth process inertia force controls the bubble growth,

not the heat transfer into the bubble. In an effort to determine a solution that incorporates both momentum and energy balances, Robinson and Judd (2001) presented a solution analogous to the homogeneous bubble growth solution. They developed their model for a hemispherical bubble (see Figure 2-8). They argued that although a viscous boundary layer exists in the liquid above the wall, the thickness of this layer is thin relative to the size of the bubble and its overall influence on the bubble can be neglected. They also assumed liquid flow symmetry about the r-axis. Through these simplifications, they modeled the bubble growth as a half segment of the spherical case. Therefore, they could use Equation 2-7, without the viscous term, for the bubble motion. As for the temperature distribution around the bubble, they solved the two-dimensional energy equation numerically in axisymmetric cylindrical coordinate for the moving liquid. Robinson and

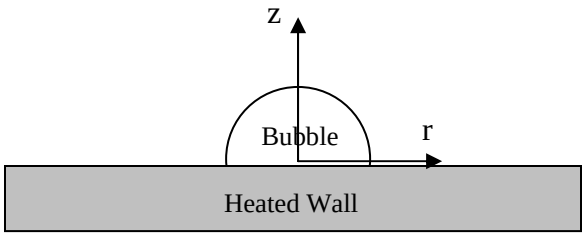

Figure 2-8: Schematic of a hemispherical bubble growing on the surface.

Judd (2001) found their results in a fair agreement with Merte et al.'s (1995) test results on R-113 in microgravity.

2-2-2-2- Bubble Growth Due to Heat Transfer from Microlayer

As the hypothesis of bubble growth due to heat transfer from the surrounding superheated liquid was being investigated by numerous authors during the 1960s, an interesting set of experimental observations led to a new theory for bubble growth that reshaped the discussion about the bubble growth mechanism/modeling over the following

years. Through direct measurement of the surface temperature, Hsu and Schmidt (1961), Moore and Mesler (1961), Rogers and Mesler (1964), Hendricks and Sharp (1964), Torikai et al. (1965), Hospeti and Mesler (1965), and Katto and Yokoya (1966) discovered that the surface temperature beneath a bubble significantly drops at the onset of nucleation. They postulated that this quick cooling process is caused by evaporation of a thin layer of liquid that gets trapped beneath the bubble during the initial phases of the bubble growth. The first actual verification of the microlayer existence was conducted by Sharp (1964) using interferometric techniques coupled with high speed photography. Using a similar technique, Jawurek (1968) measured the microlayer thickness in boiling of methanol and ethanol at a pressure range of 20-50 kPa, a heat flux range of 3-10 W/cm^2, and subcooling of 0-20 °C. The bubbling events started with initial departure of a large bubble after a long waiting time and subsequent departure of several smaller bubbles with zero waiting time. He determined that the microlayer was wedge-shaped for all bubbles with a thickness at the outer edge ranging from 0.2 to 0.8 μm.

In an effort to carefully examine/model the nature of this phenomenon, Cooper and Lloyd (1969) conducted an experimental/analytical study, in which they measured the surface temperature of a heated glass substrate beneath a bubble generated in boiling of toluene at sub-atmospheric pressures (7-14 kPa). The generated bubbles were hemispherical during the growth process and grew to a diameter of about 20 mm before departure. Cooper and Lloyd (1969) calculated the heat flux at the bubble/surface interface using the surface temperature data. The calculated heat flux was used to determine the microlayer thickness. Their measurements indicated a wedge-shaped microlayer, increasing from the bubble center to the bubble edge with a maximum

thickness of about 30-50 μm. Comparison of the calculated heat flux values with the total energy transferred into the bubble (determined using the bubble volume) suggested that microlayer played a predominant role in the bubble growth. In describing the physics of the microlayer formation, they argued that a growing bubble overtakes some of the boundary layer liquid and a balance between the inertia, viscosity, and surface tension forces determines the thickness of the trapped liquid layer. Their solution led to the following approximate expression for the microlayer thickness

$$\delta_0 = 0.8\sqrt{v_l t_g} \tag{2-27}$$

where in v_l is the liquid viscosity and t_g is the bubble growth time.

Although the Cooper and Lloyd's theory (1969) well agreed with their experimental results (a difference of ±25%), they argued that "no firm conclusions can be drawn" from their limited data, and the theory outlined in their work "contains so many approximations that the agreement with observations may be partly due to cancellation of errors". The authors stressed that their results may not apply to widely different conditions of boiling. They argued that factors tending to make bubbles grow rapidly to large size would tend to encourage formation of a microlayer and also make the bubble of hemispherical shape, with a large area of contact at the wall, hence giving a large area for microlayer development. Also, if a force proportional to $\sigma\cos\theta$ in the advancing direction is present to compensate for the momentum deficit in the viscous boundary layer, the motion of the triple interface (vapor/liquid/solid) leaves no microlayer behind.

Cooper (1969) furthered the development of the microlayer concept and its role in bubble growth by presenting a model solely based on microlayer evaporation. Since

surface cool down during the microlayer evaporation affects the rate of microlayer evaporation, Cooper (1969) provided separate solutions for the two extreme cases: either a poorly conducting liquid on a highly conducting wall, in which case the wall temperature will remain nearly constant during the evaporation period, or at the other extreme, a highly conducting liquid and poorly conducting wall, in which case the wall temperature will soon fall nearly to the liquid saturation temperature. In the case of the highly conducting wall, he determined the following correlation for bubble radius in boiling of non-metallic liquids.

$$R^*(t) = 2.5\,\mathrm{Pr}_l^{-1/2}\,Ja(\alpha_l t)^{1/2} \quad \xrightarrow{R=R^*/2^{1/3}} \quad R(t) = 1.98\,\mathrm{Pr}_l^{-1/2}\,Ja(\alpha_l t)^{1/2} \tag{2-28}$$

where in R^* is the hemispherical bubble radius. Cooper (1969) also determined the following correlation for bubble growth on a poorly conducting wall.

$$R(t) = 1.12\left\{\frac{k_s\rho_s C_s}{k_l\rho_l C_l}\right\}^{1/2} Ja(\alpha_l t)^{1/2} \tag{2-29}$$

It is quite interesting that the Cooper's (1969) model also shows that the bubble growth rate is proportional to $Ja(\alpha_l t)^{1/2}$, a conclusion reached by models that assume bubble growth is controlled by heat transfer from the superheated liquid surrounding the bubble dome. Cooper compared his model summarized by Equations 2-28 and 2-29 with the prior experimental results of Cooper and Lloyd (1966) and Cole and Shulman (1966). Figure 2-9 shows this comparison. As mentioned earlier, differences in surface and fluid properties have caused the scattered observed in the experimental data. Cooper (1969) suggested that his model is in fair agreement with the experimental data.

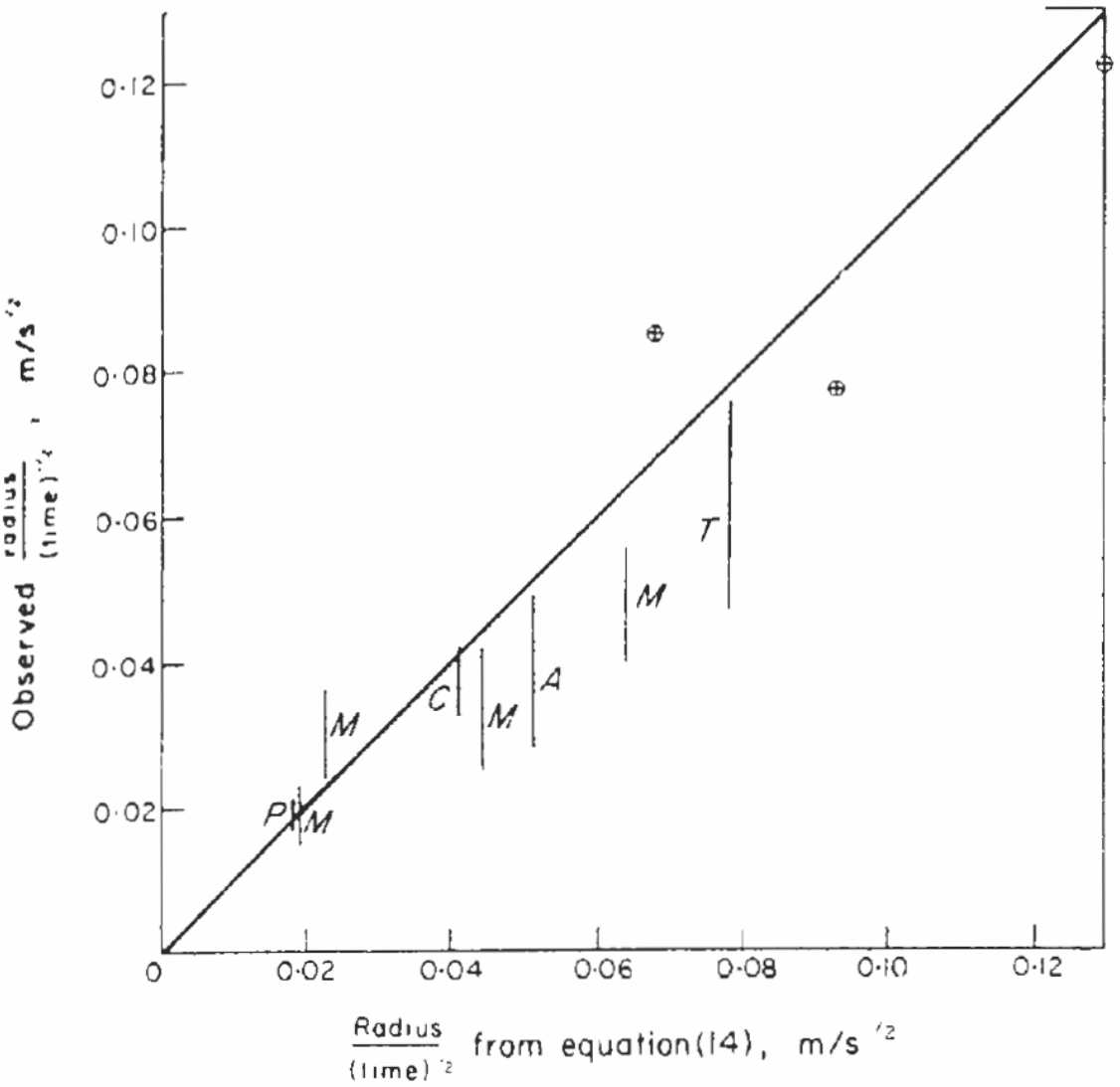

Figure 2-9: Comparison of Cooper's prediction for $R/t^{1/2}$ and experimental data of Cooper and Lloyd (1966) on toluene (⊕) and Cole and Shulman (1966) on acetone (A); carbon tetrachloride (C); methanol (M); n-pentane (P); toluene (T).

In an effort to combine the effect of heat transfer from the thermal boundary layer and microlayer, Van Ouwerkerk (1971) first determined an expression for the thermal microlayer thickness. He assumed a self-similar bubble growth equation as $R^* \propto t^{1/2}$ and conducted an elaborate analysis of the Navier-Stokes equations to determine the boundary layer thickness. He found the initial microlayer thickness

as $\delta_0(r) = 1.27(r/R^*)(vt)^{1/2}$, where in $R^*\left(=\sqrt[3]{2}R\right)$ is radius of the hemispherical bubble. Van Ouwerkerk (1971) connected the final bubble growth relation to diffusion from the thermal boundary layer for the case of a uniformly superheated liquid, cf. Equation 2-13 for the uniform bulk temperature. For a highly conducting wall he determined:

$$R^*(t) \cong \frac{2}{\pi^{1/2}}\left(1+3^{1/2}\right)Ja(\alpha t)^{1/2} = 1.128(1+1.73)Ja(\alpha t)^{1/2} = 3.08Ja(\alpha t)^{1/2} \qquad (2\text{-}30)$$

in which case microlayer evaporation accounts, independent of pressure, for 37% of the bubble radius, i.e. only for 5% of total bubble volume. One should notice that in a real situation liquid isn't uniformly at the wall temperature.

One of the unsettled issues introduced in this section is the qualitative characterization of poor and highly conducting walls and Cooper's (1969) suggestion about invariance of surface temperature of highly conducting walls. In light of the fact that large surface temperature variations has been observed in many prior experimental investigations on high thermal conductivity walls (e.g. Hendricks and Sharp (1964) observed a temperature drop of 22 °C in boiling of water on nichrome heated wall), it is necessary to further discuss this issue. The significance of this discussion lies in the fact that the surface temperature drop can reduce the microlayer evaporation rate thereby resulting to an error in bubble growth predictions of the microlayer theory. In fact, Cooper (1969) used the average surface temperature reported by Cole and Shulman (1966) in analysis of his results (using Equation 2-18 for highly conducting walls) without discussing the consequences. In an effort to quantify the effect of wall/liquid properties on bubble growth, Mei et al. (1995) developed a set of equations for the conjugate problem of heat transfer in microlayer and wall. In their model, they assumed

that microlayer accounts for 100% of the bubble growth. They used Cooper's (1969) microlayer theory to determine the initial microlayer thickness. They solved the set of equations numerically to determine the rate of evaporation of the microlayer and suggested that bubble growth (i.e. rate of microlayer evaporation) is a function of factors: $Ja = \rho_l C_l (T_w - T_{sat}) / \rho_v h_{fg}$, $Fo = \alpha_w t_d / H^2$, $k = k_l / k_w$, and $\alpha = \alpha_l / \alpha_w$. Figure 2-10 shows a parametric study of their results showing how the variation of different parameters affects the bubble growth rate.

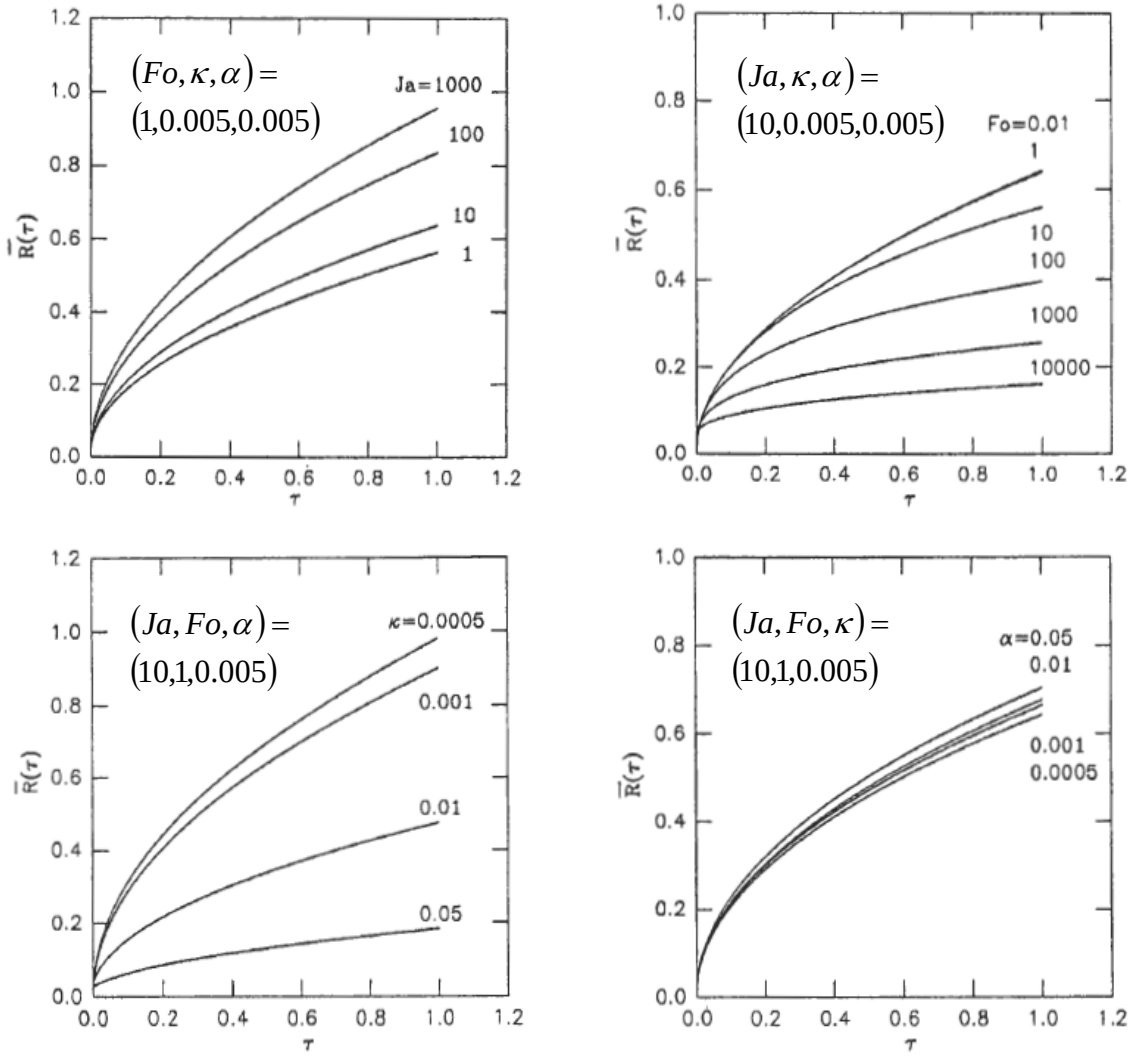

Figure 2-10: Parametric dependence of the normalized growth rate $\tilde{R}(\tau) = R(t)/R_c(t_d)$, where in R_c is bubble radius assuming constant surface temperature.

In the several decades since these ideas for bubble growth were put forth, there is still no consensus in the contribution of these competing mechanisms for a given set of fluid and surface conditions. For example, Demiray and Kim (2004) conducted an experiment on a micro heater array with FC-72 liquid at temperature 52 °C with an isothermal surface at a constant and uniform temperature of 76 °C. Their test produced a set of dissimilar bubbles. They compared the growth rate of one bubble with the total increase in surface heat transfer during the bubble growth. Their results showed that the increased heat transfer during the bubble growth is only equal to about 12% of the total bubble energy. They attributed the increase in heat transfer to the microlayer evaporation energy and thereby suggested that the microlayer contribution to the bubble growth is about 12%. In another study, Myers et al. (2005) conducted a test on FC-72 liquid at a temperature of 52.3 °C with a nominal constant heat flux surface at a temperature of about 96 °C. Their analysis of the bubble growth rate and the surface heat transfer during the growth process suggested that the microlayer contribution to bubble growth is about 50%. Thus given only slight differences in the surface boundary condition, vastly different inferences about the microlayer's contribution seem to be implied. Even with the advances provided by the novel instrumentation used in the above work, details about the microscale physics occurring around an individual bubble currently remain unresolved. To make further progress with this issue, a continued refinement of the measurement tools in terms of spatial resolution is needed.

2-3- Heat Transfer in Boiling Process

So far in this chapter we have discussed dynamics of the bubble growth and some

aspects of its associated heat transfer processes. The next important question is that how a bubble affects the heat transfer field at the nucleation site or in a broader sense how the individual bubbles construct the boiling heat transfer process. In this section, we discuss the existing analogies concerning the role of bubbles in boiling heat transfer process. From a broad perspective, boiling models can be classified into two following categories:

1- Single phase convection models

2- Combined single phase convection and latent heat transfer models

The first group of models suggests that the heat transferred from the surface is dominated by convection into the liquid phase, and the role of the bubbles is to simply induce strong convective motions within the liquid. This analogy was first presented by Jakob et al. (1935). Although experimental studies support the single-phase convection analogy in general, the exact nature of this convection process is still unknown. Different analogies suggested convection at macro- and micro-scales. The macro-scale models suggest that heat transfer to the liquid is the result of local agitation generated by the wake of departing bubbles from the heat transfer surface. The most popular model developed on this basis is that of Rohsenow (1951). He adapted a single-phase convection correlation for heat transfer ($Nu = C_1 \,\mathrm{Re}^{m_1} \,\mathrm{Pr}^{n_1}$), in which the bubble diameter and vapor superficial velocity were used as characteristic length and velocity in defining the Re number. Forster and Zuber (1955) used Rohsenow's model (1951) as the mechanism of heat transfer from the surface, but modified the expression for the bubble diameter and velocity ($R = \sqrt{\pi} Ja(\alpha_l t)^{1/2}$ and $\dot{R}$). In a similar analogy, Tien (1962) suggested that the wake generated behind a bubble possess the same velocity distribution as an

inverted stagnation point flow, except with an opposite sign. He then used the heat transfer correlation for an inverted stagnation flow (1960) to develop a correlation for the heat transfer coefficient at the bubble departure site. This correlation was then multiplied by the nucleation site density to determine a general correlation for the boiling heat transfer coefficient. Zuber {1962) also assumed a similarity between the boiling and turbulent natural convection flow to develop his version of boiling correlation based on single phase heat transfer analogy. His analysis substantiated Jakob's (1935) description of natural flow circulation and concluded that the fluid motion is similar to flow described by Malkus (1954), Thomas and Townsend (1957), and Townsend (1959) in turbulent natural convection.

The micro-scale analogy of Forster and Greif (1959) postulates that bubbles act as micropumps that remove the superheated liquid from the surface as the bubbles grow and depart from the nucleation site. The total heat transferred through subsequent pumping action was calculated using the volume of the bubble and its frequency. Forster and Greif used the difference between the bulk liquid temperature and the average of surface and bulk liquid temperatures to define the energy transported in the pumping action ($q"=(\rho c_p)\ V_b\ f\ n\Delta T$). Han and Griffith (1965) furthered the Forster and Greif (1959) analogy to a more comprehensive model. They considered the effective heat transfer surface as two parts; the bulk convection area and the natural convection area. The area influenced by the bubble was considered as the bulk convection area and the rest of the surface as natural convection area. They assumed that each bubble pumps a piece of the superheated liquid layer from the surface to the bulk liquid, and the cold bulk liquid subsequently flows on to the influenced area to replace the displaced liquid. The diameter

of the influenced area was considered to be twice as much as the bubble diameter for isolated bubble regime. Han and Griffith (1965) used natural convection correlations to calculate the transient heat transfer to the liquid adjacent to the surface during the bubble waiting period. Their final correlation accounts for the heat transfer from the influenced area and the rest of surface (for which they used natural convection heat transfer correlations). Mikic and Rohsenow (1969) modified the correlation of Han and Griffith (1965) by approximating the transient heat transferred into the liquid superheat layer using the transient conduction solution through a semi-infinite body (the liquid), while simultaneously excluding heat transfer from areas outside the bubble influence region.

Although the aforementioned models resulted in different correlations, they are all explicitly or implicitly a function of wall superheat, bubble diameter, bubble departure frequency, and nucleation site density. For instance, the nucleation site density explicitly appears in the final form of the correlation developed by Tien (1962), whereas in the Rohsenow's correlation (1951), the effect of the surface and its combination with the liquid appears as an empirically derived constant. Real evaluation of the individual models and their comparison requires more detailed information about the sub-processes of boiling. Given the wall superheat, bubble diameter, bubble departure frequency, and nucleation site density on the surface, one can calculate the heat transfer coefficient directly using any of the developed correlations. To the best of our knowledge, none of the discussed models have been tested against the four quantities measured simultaneously. The complexity of the boiling process and the inherent difficulties of isolating the important parameters of real boiling surfaces in a way that they can be measured, has overshadowed an accurate account of the different models based on the

single phase convection analogy. Although the single-phase convection analogy has been supported by experimental evidence in general, there are still questions surrounding the models developed based on these assumptions. For instance, from the aforementioned discussion, the dominance of the single-phase heat transfer mechanism and the continuous renewal of the boundary layer by the cold bulk liquid also implies that the heat flux in subcooled pool boiling should be a function of the temperature difference between the wall and the bulk liquid. As noted by Forster and Greif (1959), this trend is not observed in experimental data. Carey (1992) mentions that the boiling experimental data generally correlate better with the difference between the wall temperature and the saturation temperature (surface superheat, T_w-T_{sat}), even when the liquid pool is significantly subcooled. Forster and Greif (1959) found that a change of 300% in subcooled temperature increases the heat transfer rate only by 20%. This has prompted the use of surface superheat temperature even for subcooled boiling. Forster and Greif (1959) speculated that under subcooled conditions the increase in maximum bubble radius and decrease in bubble frequency compensates for the increase in temperature difference, and as a result the heat transfer rate doesn't significantly change.

The second group of models that was mentioned earlier account for latent heat transfer from the surface along with the single-phase convection. Contribution of the latent heat in the total heat transfer from the surface has been investigated in many studies, and different models for calculating the amount of vapor generated and departed from the surface have been developed. Graham et al. (1967) showed that a combined correlation of the microlayer evaporation mechanism at the bubble growth site along with a turbulent natural convection model for the rest of heat transfer surface would

adequately predict heat transfer from the surface. Judd et al. (1976) furthered the proposed analogy, showing that the microlayer evaporation could account for up to one-third of the total heat transfer at high heat fluxes. He also found that the contribution of the microlayer to the total heat flux is independent of subcooling.

CHAPTER 3: DESIGN OF THE TEST DEVICE

In order to study different aspects of the nucleation process and boiling heat transfer discussed in the previous chapter, a MEMS device has been developed. The design process of the device and its fabrication are discussed in this chapter.

3-1- Design Strategy

The device is intended to generate single bubbles from a fixed nucleation site and measure the wall temperature and heat flux underneath and around the bubble during the entire process of growth and departure. The temperature data are to be measured using Resistance Temperature Detectors (RTDs). This temperature measurement technique was selected for its fabrication facility and accuracy. The images of the bubbles are to be captured from the side using a high speed camera synchronized with the temperature measurement system.

3-2- Sensor Array Geometry

The primary objective in design of the sensor pattern was to achieve maximum temperature resolution using a limited number of sensors. The number of sensors in the device was limited by the number of pins of an available Pin Grid Array (PGA) and the capability of an available Analog-to-Digital (A/D) board (model CIO-DAS6402/12 manufactured by Measurement Computing Inc.) to read the sensors. Since the bubbles are to be viewed by the camera from a lateral perspective, the bond pads and wire bonds should only be placed on two sides of the device die to avoid blocking the view of the camera. Therefore, the PGA could only accommodate 48 sensors. As shown in Figure 3-1, the PGA has a total of 96 pond pads on the two sides of the die area. The A/D board

has 64 channels and a maximum sampling frequency of 330 kHz. Therefore, it can theoretically achieve a sampling frequency of approximately 5 kHz per channel (although higher rates can be achieved if only a subset of sensors is sampled).

The sensor resolution is limited by several factors including the microfabrication capabilities, temperature sensitivity, and sensors self-heating. Since the sensors are

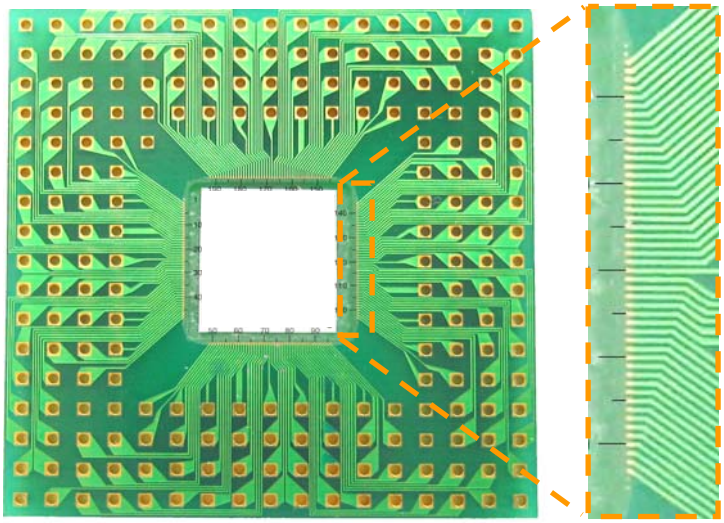

Figure 3-1: Front view of the Pin Grid Array (PGA).

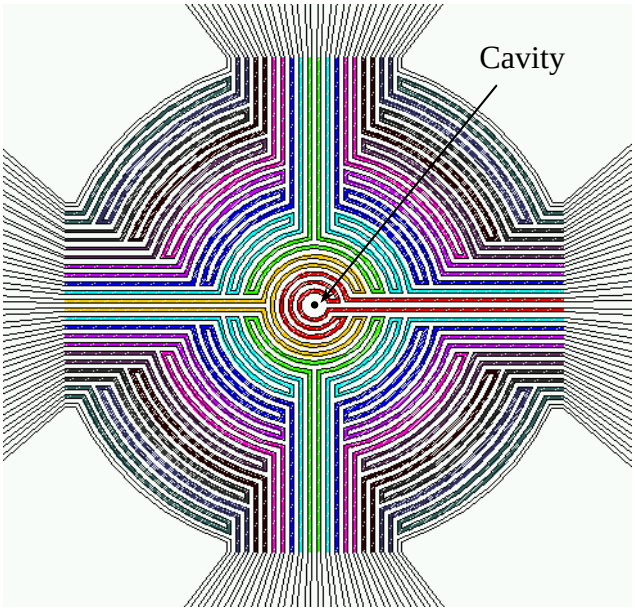

Figure 3-2: Schematic view of the sensor array around a cavity (array diameter is 1 mm).

installed in a Wheatstone bridge, their resistance and contact area with the surface determine their sensitivity and self-heating. As will be shown in the next chapter when the design of the electronics are discussed, higher sensor resistance allows for better temperature resolution and less self-heating. The sensors are designed with a resistance of approximately 1 kΩ. Figure 3-2 shows a schematic of the sensor array with the cavity at its center. The circular geometry of the sensor array is inspired by the nominally axisymmetric shape of a bubble and the fabrication of a fixed nucleation site, which allows for a high spatial resolution in the radial direction with a minimal number of sensors. The sensor array covers a circular area of 1 mm in diameter. This is about twice the bubble diameter reported by Demiray and Kim (2002) for boiling of FC-72. The spatial resolution of the sensors is between 24 to 41 μm in the radial direction. The sensors have a serpentine shape (as can be seen in the figure) with a line width of 7 μm and a distance between the neighboring lines of 10 μm. The radial distance between two neighboring sensors is also 10 μm.

3-3- Heater Size

The size of the heater is an important aspect of the device design. In most practical boiling applications with many nucleation sites, the area surrounding a nucleation site is also heated. Therefore, the liquid that replaces the displaced liquid due to bubble departure is likely to be superheated. In order to ensure that liquid over the area neighboring the sensor array is also heated, the heater size was designed larger than the sensor array area. The surface is heated by a 3×3 mm^2 square shape heater. The sensor array is centered in the middle of the heater, ensuring it is one array diameter away from the edges of the heated area.

3-4- Wall Properties

The wall thermal and geometrical properties are the most critical aspects of the device design. The wall should enable accurate measurement of the surface temperature and heat flux at the nucleation site with a minimum interference with the physics of the nucleation process. Two different design options for the wall will be discussed in the following and eventually the most appropriate design option will be selected.

3-4-1- Quartz Wall

As can be seen in the schematic of Figure 3-3, the sensor and the heater can be installed on a low thermal conductivity quartz wall. Depending on the wall thickness, the heater can be fabricated on the frontside or the backside of the wall. If a thick wall (e.g. 500-µm thick wall) is used, heater should be fabricated on the frontside of the wall (as can be seen in Figure 3-3) to reduce the heat spreading losses. However, the heater can be fabricated on either side of a thin wall (e.g. a 50-µm thick wall), since heat loss from the sides is relatively small.

Figure 3-3: Cross section of two designs on a quartz wall.

In this design, the surface temperature is directly measured by the sensor array and the local heat flux can be determined numerically. The main issue with this design is that the thermal boundary condition outside the sensor array area is unknown and either needs to be determined via an additional measurement or through simulation of a well-controlled experimental environment. Any assumption in this regard increases the uncertainty of the heat flux calculations within the sensor array region. In order to

quantify the sensitivity of the heat flux calculations within the sensor area to different boundary conditions outside the array, a numerical study has been conducted using the commercial package Icepak. The numerical study was intended to determine the actual average heat flux at the sensor array (q_{actual}) area and compare that with the applied heat flux ($q_{applied}$) to the surface. The difference between the two values represents the amount of lateral conduction within the solid. The numerical models of the thick and thin walls have been prepared. The first numerical model is a 3×3 mm^2 quartz wall with a thickness of 500 μm. Figure 3-4 shows the domain of the numerical model. Adiabatic boundary conditions were applied to the back and the four lateral edges of the model. The front side of the model was divided into two different regions including a circular area with a diameter of 1 mm at the center that resembles the sensor array area, and an outer region

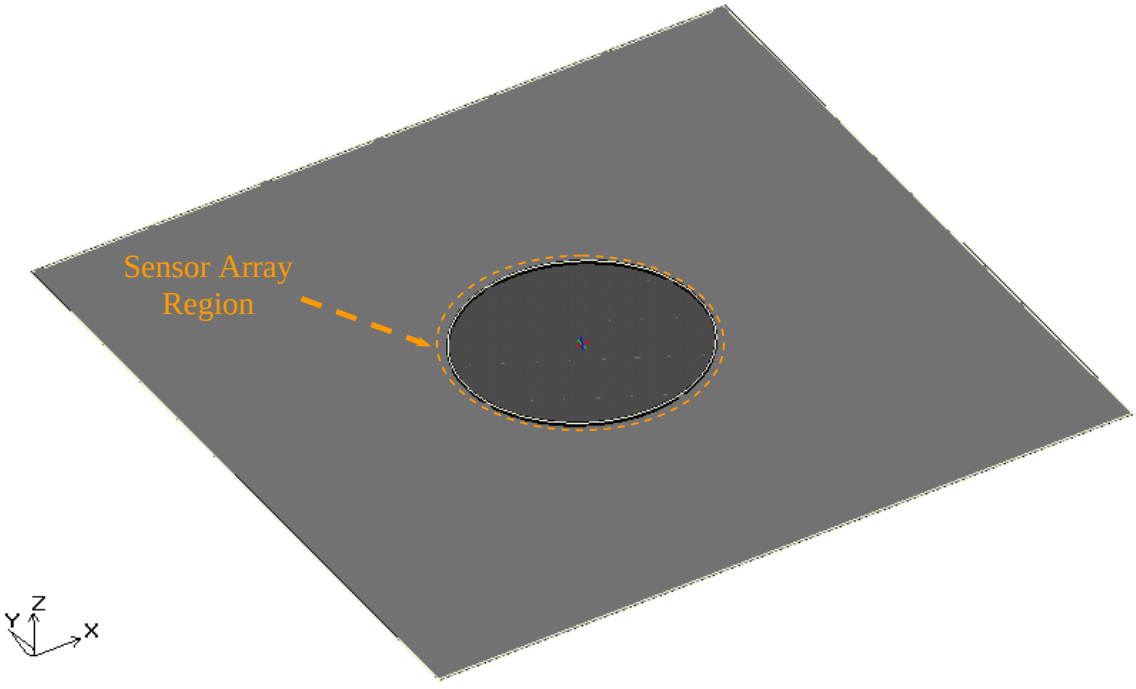

Figure 3-4: Numerical model of the quartz wall. The sensor array is shown as the dark disk.

covering the rest of the surface. A heat source with 5 W/cm^2 strength ($q_{applied}$) was defined at the front surface of the block. The heat transfer coefficient at the sensor array was set at 5000 W/m^2.K and the heat transfer coefficient outside the sensor array was set at four different values 100, 500, 2000, and 5000 W/m^2.K. The actual average surface heat flux at the sensor array area (q_{actual}) was determined. Figure 3-5 shows the ratio $q_{actual}/q_{applied}$. Figure 3-5 also shows the same ratio for the 50-μm thick wall. As can be seen in the figure, the actual average heat flux at the sensor array area is far greater than the applied heat flux even for a 50 μm thick glass substrate. This suggests a significant uncertainty in the heat flux value at the sensor array area.

Another potential issue with the thin wall design is that during the surface dry out underneath the bubble, the temperature of the substrate could significantly rise. In most applications, the high thermal conductivity of the wall does not allow the temperature of

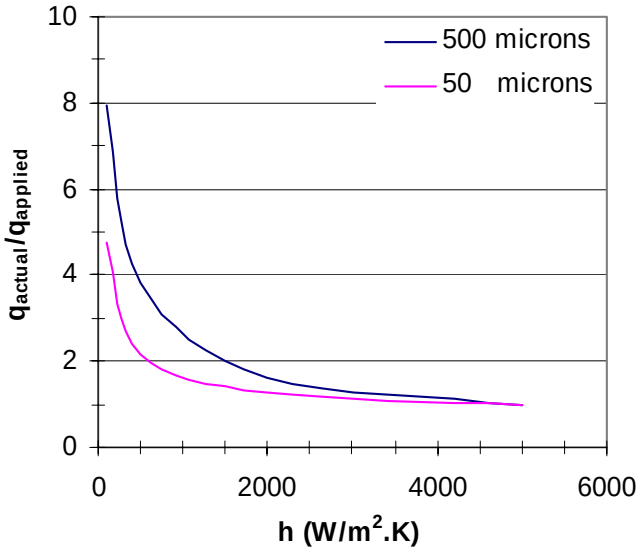

Figure 3-5: Ratio between the actual and applied heat fluxes at the sensor array area as a function of heat transfer coefficient outside the sensor array (heat transfer coefficient at the sensor array was kept constant at 5000 W/m^2.K).

the dried out region underneath the bubble to significantly increase. Excessive temperature increase at the dried out region in the test article can significantly increase the transient conduction heat transfer during the rewetting phase of the process.

3-4-2- Silicon Wall with a Thin Benzocyclobutene (BCB) Coating

The second design option is to have a highly conducting wall, such as silicon, covered with a thin coating of a thermally insulating material such as Benzocyclobutene (BCB). BCB has an order of magnitude lower thermal conductivity than quartz (0.202 W/m.K). Figure 3-6 shows a schematic cross section of this composite wall. The wall can be heated either at the top or the bottom of the silicon layer, since the through-thickness thermal resistance of the wall is insignificant. For instance, a heat flux of 5 W/cm^2 generates less than 0.02 °C temperature difference across a 50-μm thick silicon wall (a thermal conductivity of 150 W/m.K was assumed for silicon). The highly conductive layer of the wall maintains a constant temperature beneath the insulating layer throughout the nucleation process. The temperature difference between the top and the bottom of the BCB layer is a function of heat flux. Considering that the bottom temperature of the insulating layer is constant, any change in heat flux directly changes the temperature of the top of the BCB layer. In an ideal situation (when the insulating layer is very thin and can quickly reach to a steady state condition), the heat flux can also be directly calculated using temperature difference between the two sides of the BCB layer. Otherwise, the heat

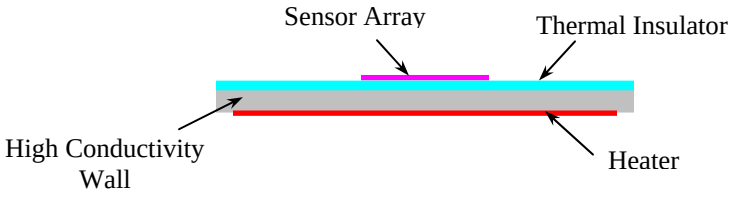

Figure 3-6: Cross section of a design with a highly conductive wall coated with a thermal insulator.

flux can be simply determined numerically by modeling the heat transfer within the BCB layer, as the lower wall boundary condition is well approximated by a constant temperature (temperature of the bottom of the BCB layer should be measured). The boundary condition at the periphery of the sensor array region can also be considered adiabatic, since the BCB layer is very thin and has a very low thermal conductivity.

Another interesting aspect of this design is that when a local dryout occurs, the insulating layer temperature only increases up to the temperature of its bottom surface (indicating a zero local heat flux). In this case, heat simply transfers to other parts of the wall through the highly conducting layer, much like in an actual heat transfer surface. In a sense, one can consider the thin insulating layer as a local temperature amplifier that enables an accurate measurement of highly resolved (spatially) temperature as well as the heat flux at the surface. This is due to the very low thermal conductivity and thickness of the BCB layer. This configuration of the wall has been selected for the final design of the device. Thickness of the silicon and the BCB layers will be determined later in this chapter.

3-5- Cavity Design

Another critical aspect of the device design is the geometric specification of a cavity that can generate bubbles at the center of the sensor array. The bubbling events should be stable and repeatable for any set of test conditions (surface temperature and liquid temperature and pressure) to allow one or few bubbles to reasonably represent the characteristics of the process at a given test condition. In order to determine the proper size and geometry of the cavity, a survey of the existing knowledge available in the literature has been conducted. Details are provided in the following.

It is widely known that vapor entrapment inside a cavity is responsible for bubble nucleation that would otherwise take place homogenously at a significantly higher temperature than it is seen in most engineering systems. Corty et al. (1955) was probably the first to relate the gas entrapment inside a cavity to the nucleation event. Internal geometry of the surface cavities, their mouth size, and the surface and liquid properties have been commonly considered (Corty et al. (1955), Bankoff (1958), Westwater (1959), Hsu (1962), Singh et al. (1976), Shoukri et al. (1975), Cornwell (1977, 1982), and Tong et al. (1990)) as effective parameters on gas entrapment inside cavities and thereby their nucleation. The nucleation process from cavities can be resolved in two different steps: 1) gas entrapment inside the cavity; 2) the necessary thermal conditions that promotes the bubble growth beyond the cavity mouth.

Understanding of the gas entrapment process enables the prediction of nucleation from a cavity with a known size and geometry. Starting with overall geometrical factors in an effort to correlate the gas entrapment process, Bankoff (1958) suggested that no gas pocket could be entrapped inside a surface cavity if the liquid perfectly wets the surface ($\theta = 0$). He suggested the following criteria for entrapment:

$$\theta \succ 180 - 2\varphi$$

where $180-2\varphi$ is the cavity angle (Figure 3-7-a). Moreover, this equation implies that a cylindrical cavity ($2\varphi=180$) can entrap gas even when a liquid front with a very small contact angle passes over the cavity.

The above-mentioned criterion is not the only one required for gas entrapment inside a cylindrical cavity. As one can guess, a shallow cylindrical cavity can't entrap gas, since the liquid front reaches the bottom of the cavity before the entrapment of a gas

pocket within the cavity can occur. The schematic diagram of Figure 3-7 illustrates such an incidence. So, geometrical factors such as depth/diameter ratio of the cavity should also be taken into account in studying the gas entrapment nature of a cylindrical cavity.

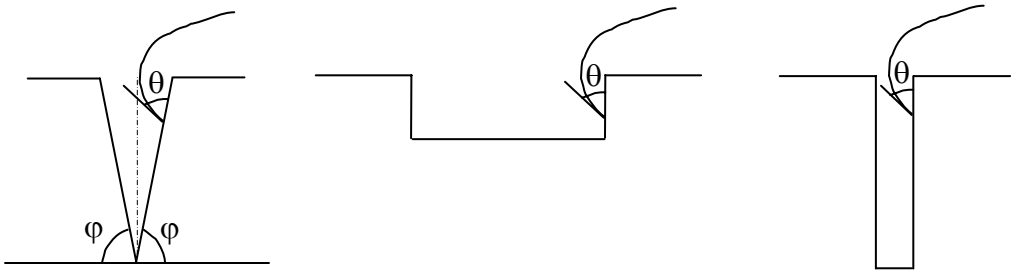

a) b) c)

Figure 3-7: a) A conical cavity; b) A shallow cylindrical cavity; c) A deep cylindrical cavity.

In an effort to understand the relation between the internal geometry of the cavities and their nucleation at different surface temperatures, Singh et al. (1976) conducted a series of tests on a set of naturally formed cavities and cylindrical cavities manufactured through laser drilling. Their studies suggested that the artificial cavities nucleate at a much smaller size than what has been suggested by some prior studies. They tried to explain the difference by arguing that most natural cavities existing on typical surfaces have a small depth/diameter ratio, whereas their laser drilled cavities had a much larger depth/diameter ratio. They supported this argument by testing cavities with different depth against water and methanol. They observed that for a 5 μm in diameter cavity at a depth/diameter ratio of more than 4 for water ($\theta = 45°$) and 8 for methanol ($\theta = 8°$), the required superheat of activation was equal to the value predicted by the static equilibrium criteria. They showed that as the depth of cavity decreased, the required temperature for its activation increased almost exponentially. They speculated that

because of the smaller contact angle, the organic liquids could penetrate more inside the cavities and thereby reduce the chance of gas entrapment at the bottom of the cavity.

It is generally known that small cavities activate at higher surface temperatures than the large cavities. Therefore, it is plausible to suggest that the large and shallow cavities of the Singh et al. (1976) study have eventually become active due to the activation of smaller cavities within them, whereas the small and deep cavities that have become active by themselves. Cornwell (1977) identified this as a source of discrepancy in the literature about the size of active cavities. Before discussing Cornwell (1977) observations, a few of these discrepancies are discussed in the following.

Clark et al. (1958) conducted an experimental study on boiling of pentane and ether. They measured the size of active cavities at different heat fluxes and reported a size range of 8 μm to 208 μm in diameter. Shoukri et al. (1975) investigated the nucleation of cavities under different heat fluxes in boiling of water on a copper surface. The size of active cavities were found to range from 2 to 20 μm. Knowing that the water surface tension is higher than the surface tension of both pentane and ether makes the comparison of the results given by Clark et al. (1958) and Shoukri et al. (1975) controversial in a sense that active cavities in boiling of water were found to be much smaller than in the boiling of pentane and ether. No information on internal geometry of the cavities is provided in the two studies.

In a more careful experimental study, Cornwell (1977) noticed the presence of small micron size cavities inside much larger cavities and argued that gas entrapment can readily occur inside these sub-cavities even though the cavities themselves might be filled with liquid. He criticized the efforts of some of his predecessors for trying to draw

conclusions on nucleation criteria of cavities by comparing the experimental results with the classical theories using the measured diameter of the cavities on the surface.

As mentioned earlier, the second stage in nucleation process is that proper thermal conditions outside the cavity should exist to allow further growth of a bubble beyond the cavity mouth. Hsu (1962) postulated that certain conditions outside a cavity should exist to allow a bubble to continue its growth beyond the cavity mouth. He suggested that the temperature of the liquid surrounding the top of the bubble should exceed the temperature necessary for the bubble nucleus to remain in equilibrium. Using this criterion, Hsu (1962) determined the following correlation for the size range of the active cavities.

$$r_{c,\frac{\max}{\min}} = \frac{\delta}{2C_1}\left[1-\frac{\theta_s}{\theta_w} \pm \sqrt{\left(1-\frac{\theta_s}{\theta_w}\right)^2 - \frac{4AC_3}{\delta\theta_w}}\right] \tag{3-1}$$

where in $\theta_s = T_{sat} - T_\infty$, $\theta_w = T_w - T_{sat}$, and $A = 2\sigma T_{sat}/h_{fg}\rho_v$. Hsu (1962) suggested a set of values for constants $C_1 = 2, C_2 = 1.25$, and $C_3 = 1.6$.

In order to determine the size of active cavities using Equation 3-1, the thermal boundary layer thickness and the surface temperature should be known. The boundary layer thickness can be estimated as $\delta = k/h$, but one needs to know the heat transfer coefficient to calculate the boundary layer thickness. In a recent study by Moghaddam et al. (2003), a heat transfer coefficient of approximately 5200 W/m^{2}K was determined at a superheat temperature of 25 °C in saturated boiling of FC-72 on a plain copper surface. Moghaddam et al. (2003) also measured a heat transfer coefficient of about 15000 W/m^{2}K at 20 °C in boiling of water on the same surface. Using this data, the thermal boundary layer thickness is calculated to be 11 and 42.7 μm for FC-72 and water, respectively. Using Equation 3-1, diameter of the active cavities is determined to be

between 0.08 and 11.9 μm for FC-72 and between 0.4 and 42.2 μm for water. Note that the liquid is at saturation conditions in all the above calculations ($\theta_s = 0$).

In an effort to explore the nucleation stability of cavities, Shoji et al. (2001) studied the effect of cavity geometry on its stability in boiling of water. They manufactured conical, cylindrical, and re-entrant cavities with a mouth diameter of 50 and 100 μm with laser drilling. Their study showed that cylindrical cavities are no different than re-entrant cavities in terms of nucleation stability, while conical cavities generate bubbles intermittently. They provided no data on the depth of cavities, so their results can't be directly compared with those of Singh et al. (1976).

3-6- Device Design

In the previous sections, different elements of the device design including the sensor array geometry, the overall wall configuration (see Figure 3-6), and the geometry of the cavity and its size were discussed. The design of the device was conducted in two stages. First, a 1st generation device was designed and fabricated to measure the temperature variations of a silicon wall during the nucleation process of FC-72 liquid. A general description of the 1st generation device is provided in the following section and the fabrication process is described in Appendix "A". Testing of the 1st generation device indicated that during the nucleation process, temperature of the silicon surface at the center of the sensor array fluctuated approximately 0.8 °C. The average temperature fluctuation of the entire sensor array was approximately 0.4 °C. The test suggested that the temperature of the silicon wall remains nearly isothermal in boiling of FC-72 liquid. This verified that silicon could be used as the material of the highly conductive layer of the device with the configuration shown in Figure 3-6. This led to design and fabrication

of the 2nd generation device. A general description of the device is discussed in this chapter and the fabrication details of the device are provided in chapter 5.

3-6-1- 1st Generation Device

As mentioned earlier, the sensor array was directly fabricated on the silicon surface. The schematic of Figure 3-8 depicts the arrangement of the sensor array and cavity with respect to the silicon wall. The wall is a square membrane measuring 3.6 mm in a side with a thickness of 30 μm. The membrane is uniformly heated from the backside by a 3×3 mm^2 microfabricated square shape thin-film heater. The diameter of the cavity was designed to be 3 μm with a depth of 25 μm. This provided a depth to diameter ratio of about 8. The cavity has a cylindrical geometry. It is important to mention that a smaller cavity size was more desirable to achieve a higher depth/diameter ratio, but the fabrication cost of the photomask required for pattering the cavity was prohibitive. As will be shown in chapter 5, when the fabrication process of the 2nd generation device is

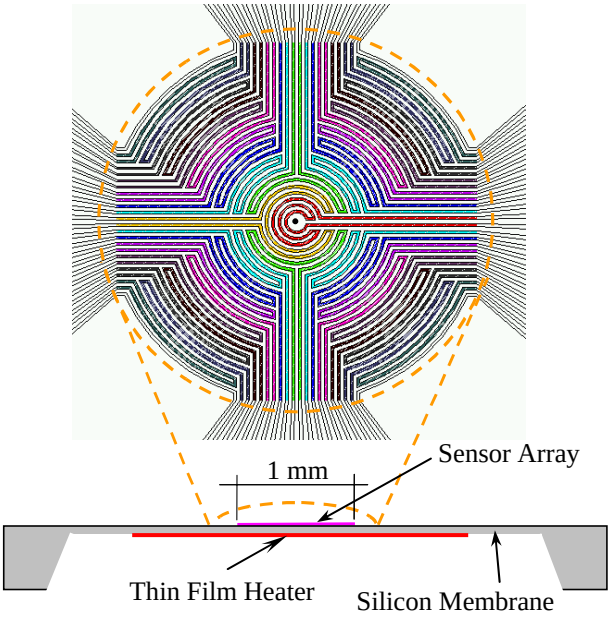

Figure 3-8: Schematic of the 1st generation device.

discussed, much smaller cavities were later fabricated on the 2nd generation of the device using Focused Ion Beam (FIB). Details of the fabrication process of the device are provided is Appendix "A". Figures 3-9 and 3-10 show a front view of the sensor array and a cross section of the membrane, respectively.

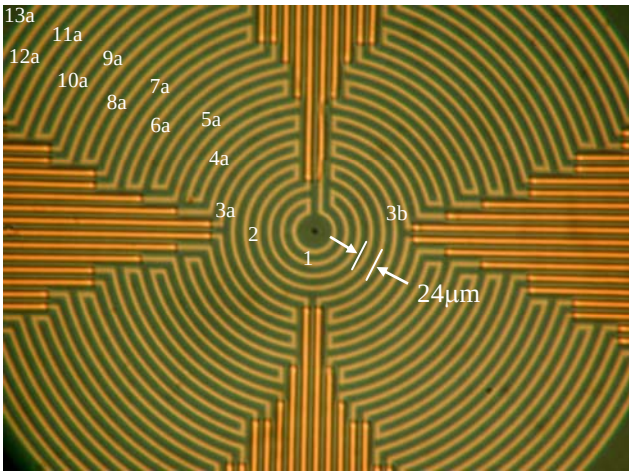

Figure 3-9: Top view of the sensor array.

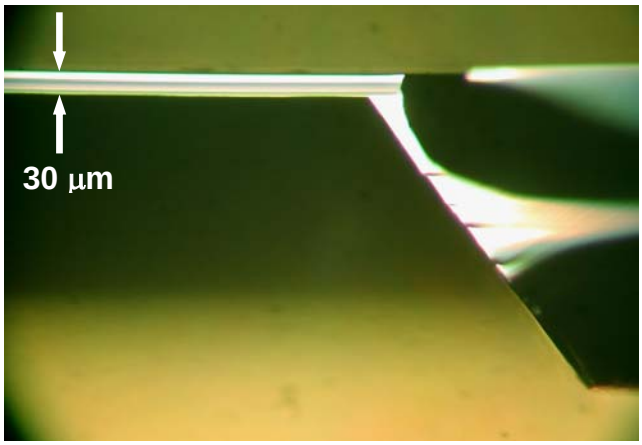

Figure 3-10: Cross section of the silicon membrane.

3-6-2- Design of the 2nd Generation Device

As mentioned earlier, the BCB layer of the 2nd generation device is expected to enable accurate calculation of the local surface heat flux. Therefore, its thickness should be designed to cause a sizable temperature change at the surface during the rapid changes

of the surface heat flux. Assuming a heat flux in the order of 10 W/cm^2 and using an approximate value of 0.2 W/m.K for thermal conductivity of BCB (see Table 3-1 for properties of BCB), the thickness of the BCB layer was selected to be 10 μm to achieve a temperature difference of 5 °C between the top and bottom of the BCB layer (see Figure 3-11). This allows measuring the heat flux with an accuracy of 2.8%, considering a temperature uncertainty of 0.1 °C.

Table 3-1: Thermophysical properties of BCB (Pinel, 2002).

Thermal conductivity [W/m.K]	0.18- 0.24
Thermal capacity [J/Kg.ºC]	1176+3.37*T
Density [Kg/m^3]	1051

Figure 3-11 shows a schematic cross section of the 2nd generation device. Note that the thickness of the silicon layer was increased to 60 μm (instead of 30 μm as in the 1st generation device) to further reduce the temperature fluctuation amplitude at the silicon surface. Also, as can be seen in the figure, in addition to the sensor array at the top surface of the BCB layer, a single temperature sensor (H-1) was placed at the

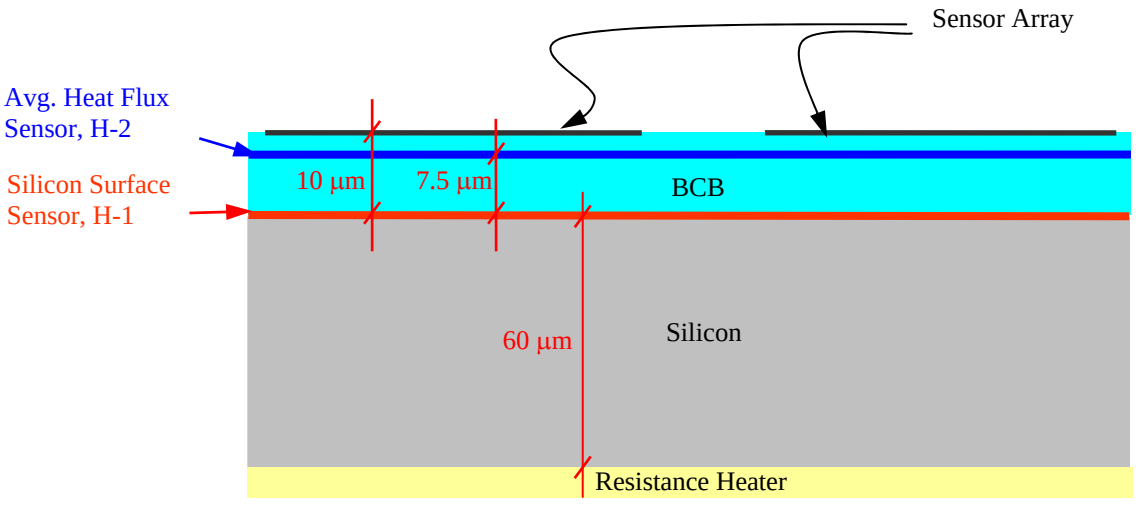

Figure 3-11: Schematic cross section of the 2nd generation device.

BCB/silicon interface to measure the temperature of the silicon surface. Another single sensor (H-2) was designed to measure the total heat flux through the entire sensor array area. The integral of the heat flux values over the entire sensor array should be equal to the heat flux determined using temperature sensors H-1 and H-2.

CHAPTER 4: SIGNAL PROCESSING AND EXPERIMENTAL SETUP

This chapter describes the details of the experimental setup fabricated to conduct boiling tests using the MEMS device described in the previous chapter. Details of the electronic system that was designed and fabricated to read the temperature sensors are first described, followed by detailed descriptions of the test chamber and control systems used to maintain consistent testing conditions.

4-1- Signal Processing

As mentioned in the previous chapter, the temperature sensors of the MEMS device are Resistance Temperature Detectors (RTDs). A circuit has been built to measure the changes in resistance experienced by each sensor in the array as a result of the local changes in temperature. Specific importance was given to three parameters (design drivers):

I) Maximize noise rejection

II) Minimize self-heating

III) Maximize temperature resolution

Each sensor element is read using a single amplifier circuit. Each circuit contains all the required components to amplify and directly feed the signal to the A/D board for measurement. Figure 4-1 shows a typical circuit. The sensor Signal Conditioning Board (SCB) contains 44 copies of this circuit (see Figure 4-2) along with the required power supplies. The selected circuit is a Wheatstone bridge amplifier. Two potentiometers are provided to balance the bridge, thereby zeroing the output of the amplifier at a low temp-

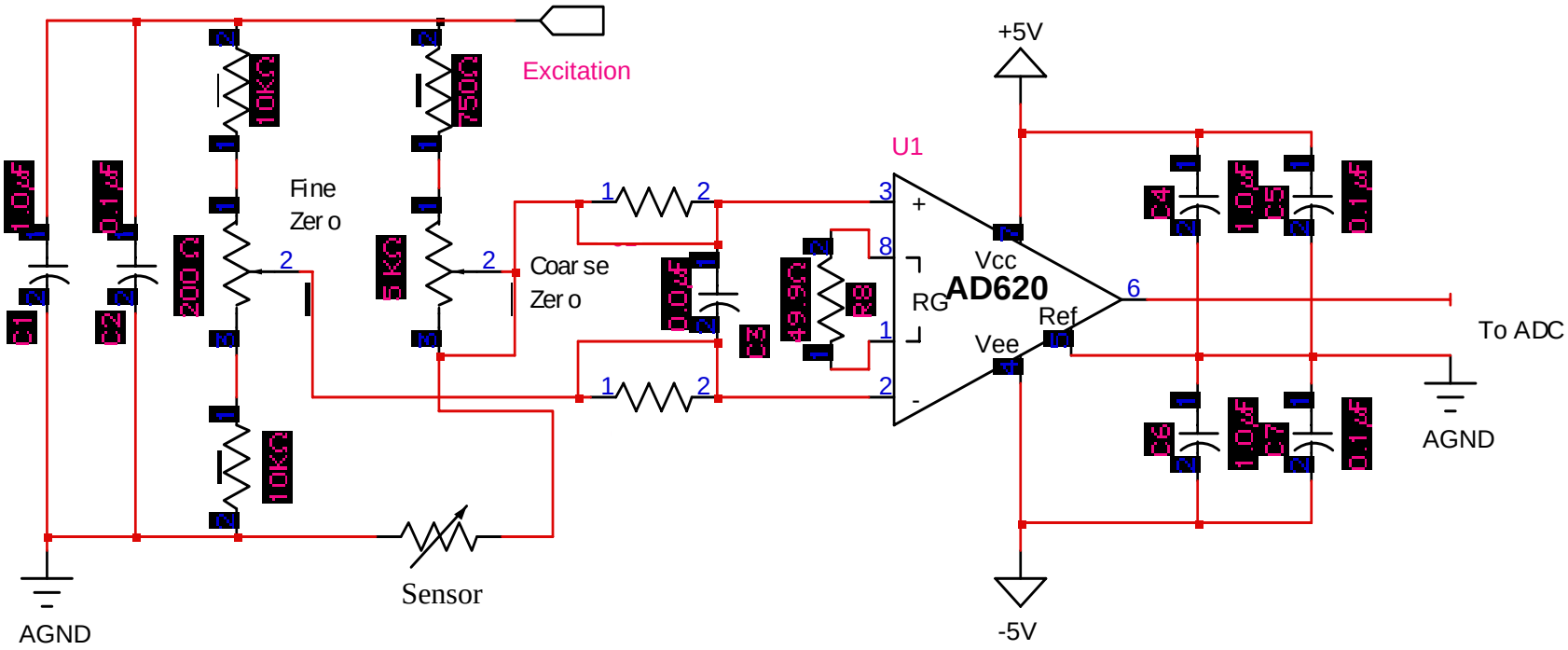

Figure 4-1: Circuitry for each element of the sensor array.

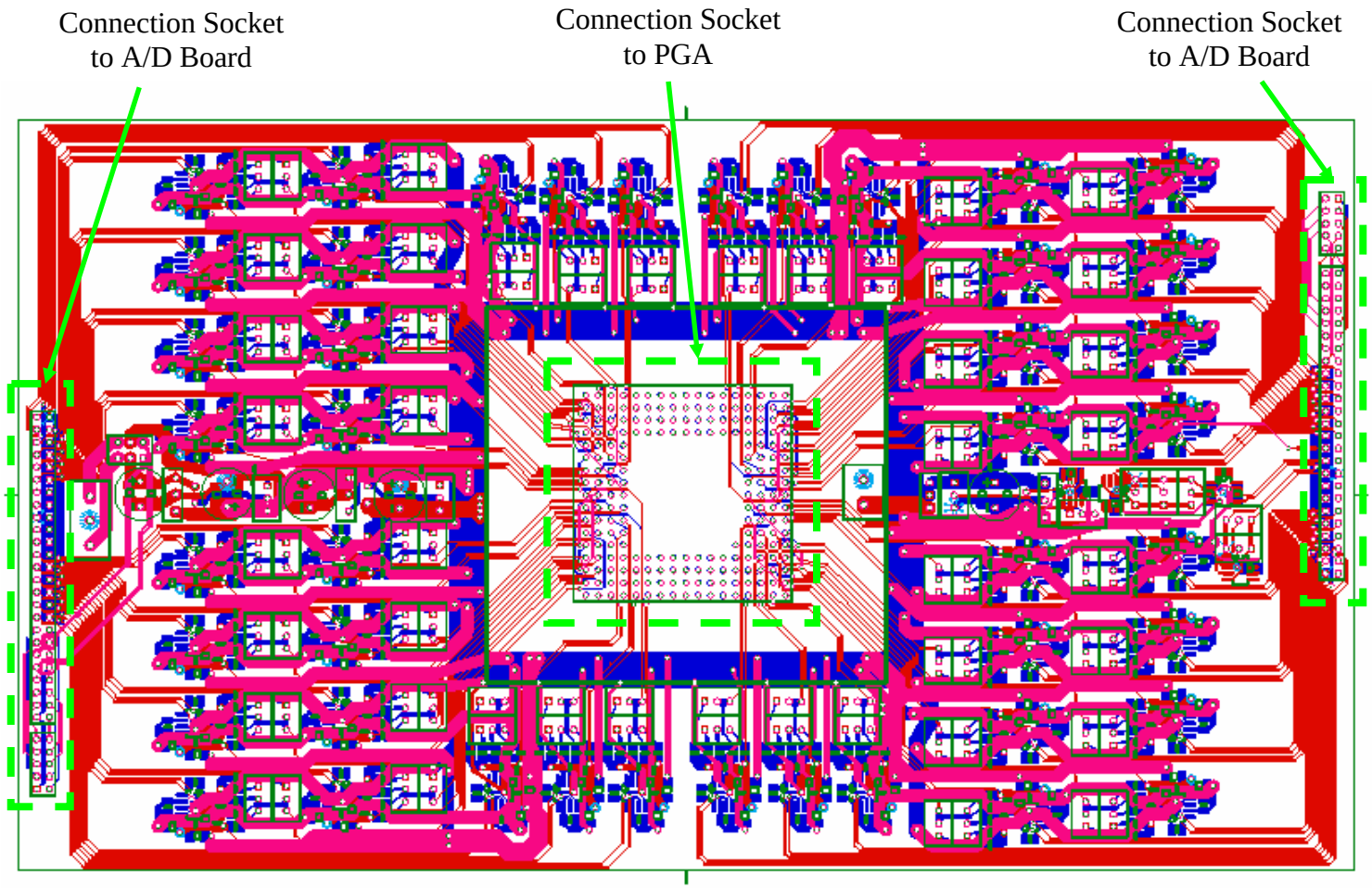

Figure 4-2: Signal conditioning board (SCB).

erature set point. A single instrumentation amplifier (model AD620 from Analog Devices, Inc.) was chosen over the standard 3-amplifier design to maximize common mode rejection and minimize sensor crosstalk. This also helped to minimize board size, component count, and amplifier to sensor distance, thus reducing noise. Additionally, the following measures were taken to optimize the SCB performance:

1- Amplifier to sensor distance was minimized to reduce noise susceptibility
2- Both leads of each RTD were routed next to each other to increase common mode rejection
3- The SCB was routed with a ground plane to minimize the external interference and provide a low impedance ground reference
4- Three low noise power regulators were included directly on SCB to avoid noise due to the use of external power supplies
5- The SCB was powered by the A/D board

4-2- Analysis of the Wheatstone Bridge

As mentioned earlier, a Wheatstone bridge amplifier circuit is used to measure temperature variations of each sensor. The operation of the Wheatstone bridge is analyzed in order to determine the relation between the output voltage of the bridge and the excitation voltage. Figure 4-3-b shows a schematic of the Wheatstone bridge. As can be seen in Figure 4-3, each one of the variable resistances (the 200 Ω and 5 kΩ potentiometers) is divided into two resistances. The bridge is assumed initially be in a balanced state, representing the nominal zero set point corresponding to a sensor resistance R_S. Therefore, the following relation exists between the resistances.

$$R_1 + R_2 = R_3 + R_S = R' \qquad (4\text{-}1)$$

When resistance R_S changes to $R_S + \Delta R_S$, the bridge output can be determined using the following expression.

$$V_o = \frac{R_S + \Delta R_S + R_3}{R_1 + R_2 + R_3 + R_S + \Delta R_S} \times V_e - \frac{V_e}{2} \tag{4-2}$$

Using Equation 4-1, the following algebraically simplified version of Equation 4-2 can be determined:

$$V_o = \left(\frac{R' + \Delta R_S}{2R' + \Delta R_S} - \frac{1}{2} \right) \times V_e = \frac{1}{2} \left(\frac{\Delta R_S}{2R' + \Delta R_S} \right) \times V_e \tag{4-3}$$

Considering that $R_3 + R' = 5750$ and using Equation 4-1, the following expression for R' can be determined.

$$R' = \frac{5750 + R_S}{2} \tag{4-4}$$

By substituting for R' in Equation 4-3, and also knowing that $\Delta R_S = \alpha R_S \Delta T$, the following expression for the output and excitation voltages ratio (V_0/V_e) is determined:

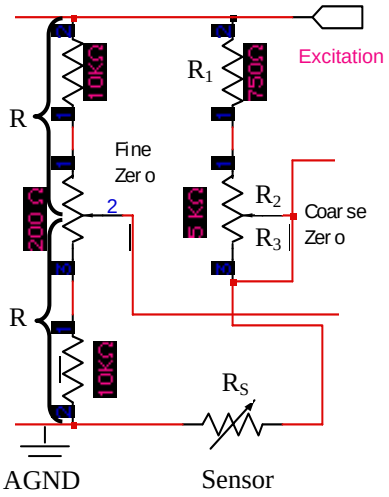

a) Wheatstone bridge as shown in the circuit diagram of Figure 4-1

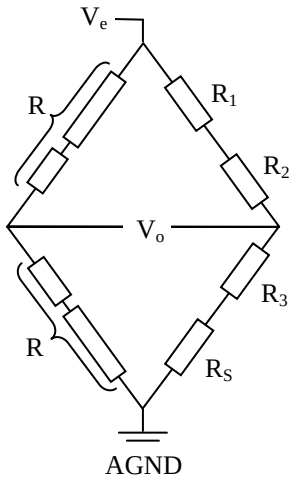

b) Schematic of the Wheatstone bridge

Figure 4-3: Wheatstone bridge.

$$\frac{V_o}{V_e} = \frac{1}{2}\left(\frac{\alpha\Delta T}{5750/R_S + (1+\alpha\Delta T)}\right) \tag{4-5}$$

Unlike in a bridge with equal resistances in all of its legs, the output of this bridge depends on the sensor resistance (R_S). Using $\alpha_{Pt} = 40e-4/^{\circ}C$ and $\Delta T = 1^{\circ}C$, the parameter V_0/V_e was calculated for a resistance range of 1 to 4 kΩ and the results are presented in Figure 4-4. As can be seen in Figure 4-4, ratio V_0/V_e increases with increasing the sensor resistance. However, the increase is not linear. For instance, doubling the sensor resistance from 2 kΩ to 4 kΩ results in an increase of only 59% in V_0/V_e.

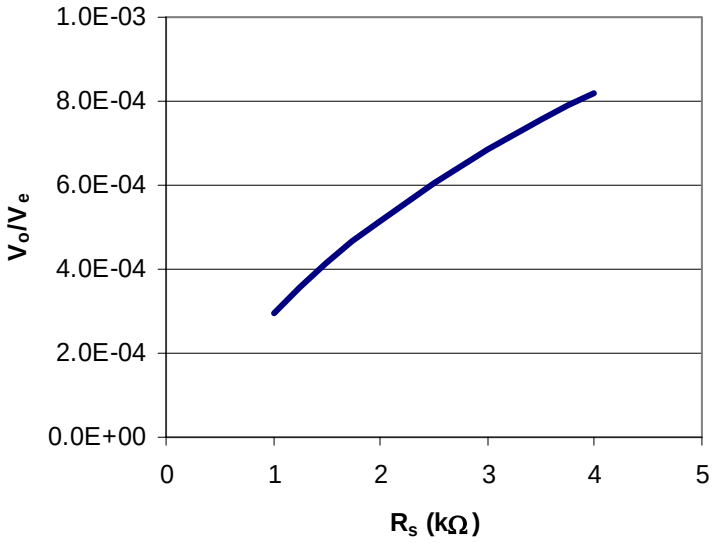

Figure 4-4: Variations of the Wheatstone bridge response with sensor temperature.

4-3- Excitation Voltage, Gain, and Bandwidth

As mentioned earlier, it is desirable to increase the sensor resistance to achieve a higher V_0/V_e. However, fabrication of high resistance sensors in the small available spaces in the sensor array is a challenge. As one can guess, in addition to the sensor width and length, sensor thickness can also be changed to change its resistance. Although it has

not been mentioned in fabrication of the 1st generation device (see Appendix "A"), the proper thickness of the Pt layer used in the fabrication of the sensor array was determined through a trial-and-error process. One aspect of this process was to determine the effect of Pt thickness on temperature sensitivity of the sensor resistance. Two thicknesses were selected for a sensitivity study (20 nm and 5 nm). At room temperature, the low resistance sensor array (20 nm thickness) ranged between 793 Ω and 1923 Ω, depending on the length of the serpentine path. The high resistance sensor array (5 nm thickness) ranged between 1984 Ω and 4882 Ω. Resistances were subsequently measured at temperatures 60 °C and 80 °C. Significant differences were observed between these two sensor arrays; most notably in the average percentage change in resistance over the test temperature range. For the low resistance sensor array, the change in resistance was $\delta_{\Delta T=20} = 1.5\%$ while the high resistance array yielded a 2.6 times smaller variation with $\delta_{\Delta T=20} = 0.56\%$. This suggested that temperature sensitivity of the sensor array (α) was reduced by decreasing the platinum layer thickness. Using the resistance values and α, Equation 4-5 was used to determine V_0/V_e. Results suggested that using the 4882 Ω resistor in the bridge results in a 31.2% smaller V_0/V_e than using the 1923 Ω resistor, and hence a better sensor resolution could be achieved by using the low resistance sensor array.

In order to minimize sensor self-heating, a low excitation voltage of 0.6 Volts was applied to the Wheatstone bridge. Using the following equation, total power dissipation over the entire array was determined to be 0.4 mW.

$$Q_{total} = \sum_{i=1}^{44} \frac{\left(V_e R_{S_i} / \left(R_{S_i} + 5750\right)\right)^2}{R_{S_i}} \tag{4-6}$$

This power dissipation is equivalent to a heat flux of 0.05 W/cm^2 at the surface.

A gain (G) of 1000 was specified for the amplifiers, which gives a closed loop bandwidth of 10 kHz for the selected amplifier. This bandwidth is believed to be sufficient for the purpose of this study.

4-4- Self-heating Error

Power dissipated within the sensor due to the bridge excitation voltage increases the sensor's temperature above that of the surrounding environment. The difference in temperature between the sensor and the surrounding environment is known as the self-heating error. The self-heating error can be estimated using the principle of conservation of energy as expressed in the following simplistic equation.

$$\Delta T_{s-h} = R_T . Q_S = R_T . \frac{V_S{}^2}{R_S} \tag{4-7}$$

where R_T is thermal resistance between the sensor and its environment, Q_S is the heat released in the sensor, V_S is the applied voltage to the sensor, and R_S is the sensor's electrical resistance. For a constant heat release (constant voltage and resistance), reducing the sensor surface area results in an increase of thermal resistance between the sensor and its environment and consequently an increase of its self-heating error.

To evaluate the self-heating error of the sensors, a numerical model of a typical sensor on the silicon membrane was constructed using Icepack software (from Fluent Inc.). The numerical domain (see Figure 4-5) consists of a 30 μm thick, 310×34 μm^2 silicon block (see Table 4-1 for silicon thermophysical properties) with a U-shape strip on its top surface simulating a typical serpentine shape sensor. The sensor has a total length of about 600 μm, width of 7 μm, and spacing between the lines of 10 μm. It is

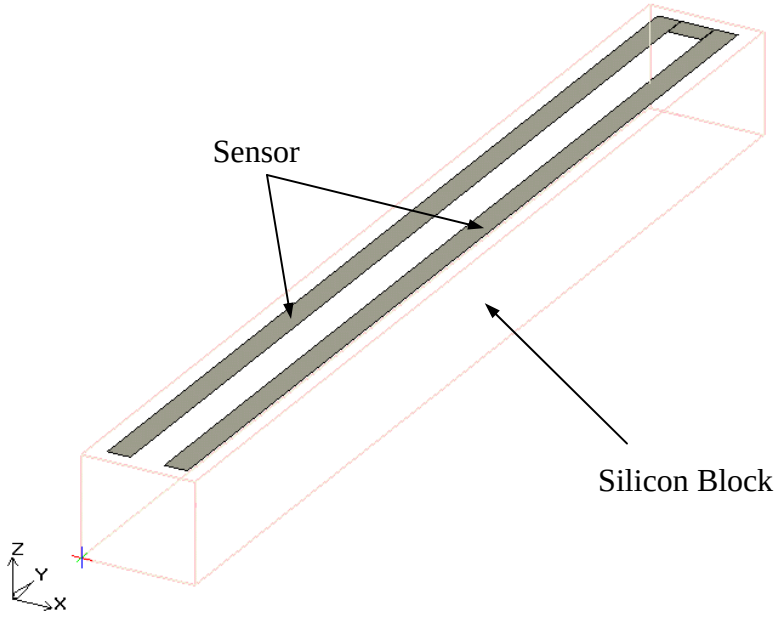

Figure 4-5: Numerical model of a sensor on the silicon block.

spaced 5 μm (half the distance between two neighboring sensors) away from the sides of the silicon block. The sides of the silicon block were assigned symmetry boundary conditions, simulating the existence of similar neighboring sensors. An adiabatic boundary condition was applied to the top surface, conservatively assuming that no heat was conducted into the liquid. The bottom surface was specified a constant temperature of 80 °C, and a total heat generation of 0.01 W was applied to the sensor. The numerical mesh was refined in several steps until a mesh independent solution was achieved. The final node count in the different directions are x_{count}=38, y_{count}=62, and z_{count}=28. The average temperature of the sensor was determined to be 80.297 °C. Using the numerical results, the thermal resistance was determined to be ($\frac{0.297\,^{\circ}C}{0.01W}=$) 29.7 °C/W.

Table 4-1: Thermophysical properties (at T=350 K) of pure single crystal silicon; n-type; electrical resistivity 3 ohm-cm at room temperature (Touloukian, 1970).

Thermal conductivity [W/m.K]	106.7±5%
Thermal capacity [J/Kg.K]	761.5
Density [Kg/m^3]	2329.0

In order to ensure the accuracy of the numerical model, a test case with a known analytical solution was determined. A uniform heat flux was applied over the entire top surface of the silicon block, instead of the sensor area alone, and a thermal resistance of 26.2 °C/W was determined. The exact analytical solution for thermal resistance in this case is ($\frac{\Delta x}{k.A} = \frac{30\times10^{-6}}{106.7\times34\times10^{-6}\times310\times10^{-6}} =$) 26.67 °C/W that is 1.8% higher than the value determined from the numerical simulation. Thus the accuracy of the numerical model in determining the thermal resistance is in the order of 2%. Using the calculated thermal resistance of 29.7 °C/W and an electrical resistance of 1200 Ω for the sensor, the sensor self-heating error as a function of applied voltage was determined as presented in Figure 4-6. As can be seen in the figure, sensor self-heating error is very small in

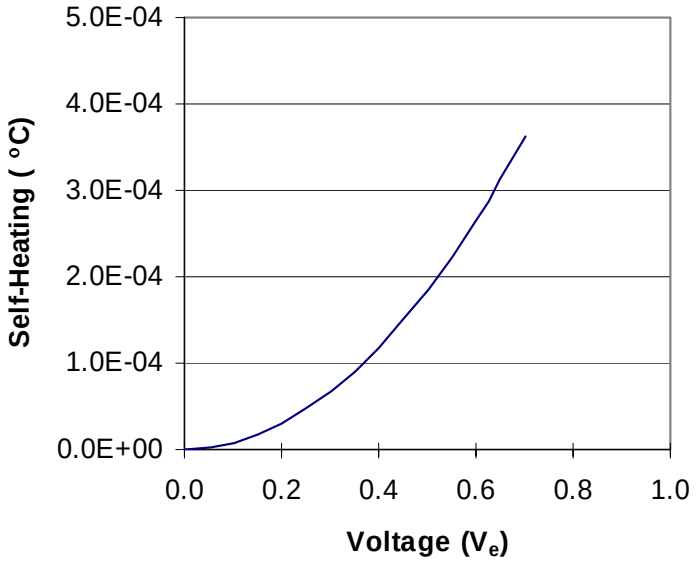

Figure 4-6: Self-heating error as a function of the bridge excitation voltage.

comparison to the expected accuracy of ±0.1 ºC for a well-calibrated RTD. A bridge excitation voltage of 0.6 V was used for the experiments.

4-5- Experimental Apparatus

As can be seen in schematic Figure 4-7, the sensor/PGA package is attached to the bottom cap of the test chamber using Ecobond-285 epoxy. The liquid chamber has double-glass windows on two sides to allow photographing the bubble images. Figure 4-8 shows the actual sensor/PGA package through of a window. As can be seen in Figure 4-7, the liquid chamber is connected to a bellows enclosed within a pressure regulated chamber in order to maintain the liquid at a specified pressure above or below the local atmospheric pressure. A hot water line is connected to the external jacket of the liquid chamber to control the liquid temperature and to provide nominally isothermal conditions, ensuring that liquid stratification is minimized within the chamber. Hot water is supplied to the liquid chamber external jacket by a highly stable (±0.01°C variation in the thermal bath) thermal bath (model EX-7 manufactured by Thermo Electron Corporation). A pressure and a temperature sensor are installed in the liquid chamber to

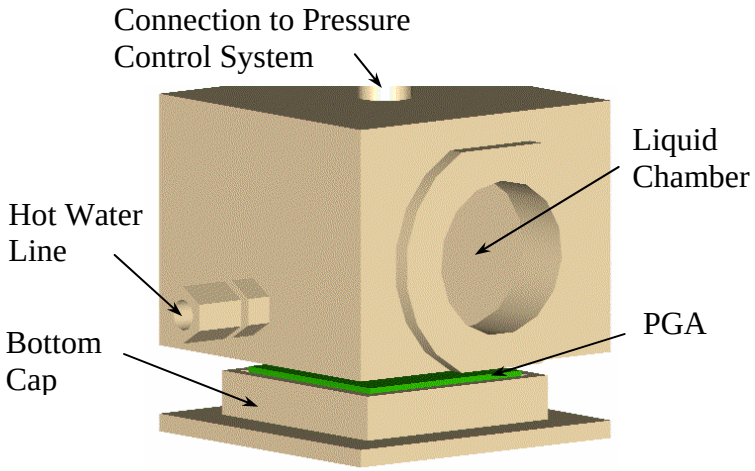

Figure 4-7: 3D schematic of the test chamber assembly.

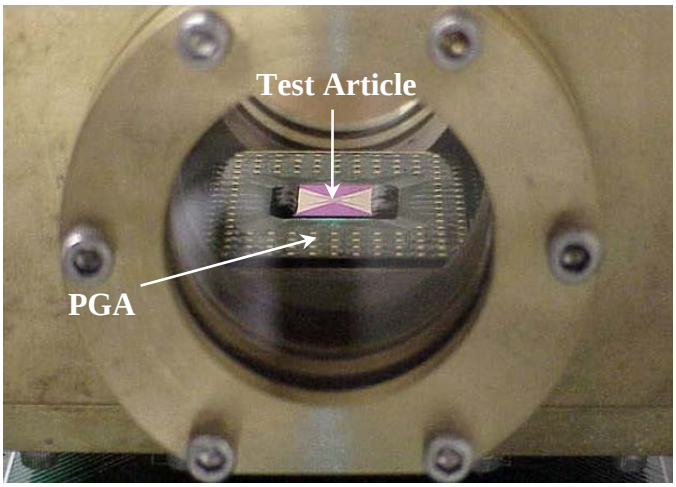

Figure 4-8: Inside view of the liquid chamber showing the sensor/PGA package.

monitor these properties during the experiment, and ensure that the liquid is maintained at proper conditions.

Figure 4-9 shows the experimental setup. As can be seen in the figure, the PGA is connected to the Signal Conditioning Board (SCB) through a stack of sockets. The output of the SCB is supplied to the A/D board (model CIO-DAS6402/12 manufactured by Measurement Computing Inc.) installed in a PC. The LabVIEW software is used to read the sensors with a sampling frequency of 8 kHz. A high speed camera (CMOS Phantom

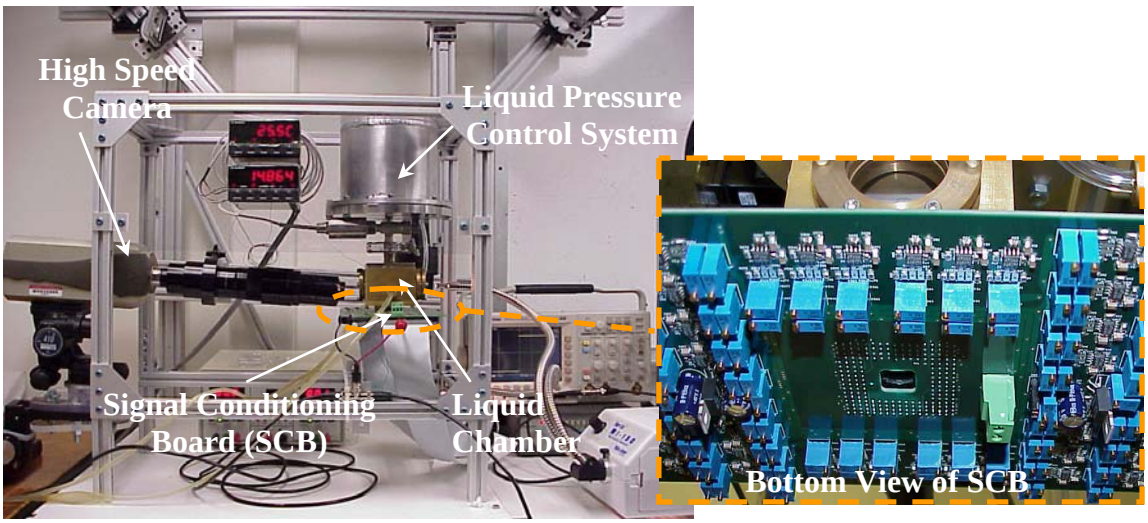

Figure 4-9: Experimental apparatus.

v9.0 camera manufactured by Vision Research, Inc.) capable of taking up to 8000 pictures per second is used to monitor the growth and departure process of the bubbles from the surface. The high speed camera is synchronized with the A/D board using a signal, generated by a function generator, supplied to the triggering channel of the camera as well as a channel of the A/D board.

CHAPTER 5: MICROFABRICATION AND CALIBRATION OF THE 2ND GENERATION DEVICE

This chapter describes details of the microfabrication and packaging of the 2nd generation device. As described in chapters 3, the fundamental difference between the 1st and 2nd generation devices is that in the 2nd generation device the silicon membrane is coated with a layer of BCB to amplify the surface temperature fluctuations and to allow calculating the local surface heat flux. Due to a large uncertainty in the exiting data on the thermal conductivity of the BCB, which was required to calculate the heat flux, a test article was designed and fabricated to accurately measure the thermal conductivity of the BCB. Details of the test article and the test results are described in this chapter. Finally, the calibration procedure of the temperature sensors is discussed.

5-1- Microfabrication Process

The 2nd generation device was fabricated on a 300-μm thick n-type <100> silicon wafer with oxide and nitride layers on both sides. This is similar to the substrate used in fabrication of the 1st generation device. Figure 5-1 shows the microfabrication sequence of the 2nd generation device. A 60-μm thick silicon membrane was fabricated on the substrate through the same set of processes explained in fabrication of the 1st generation device (see Appendix "A"). The first temperature sensor (H-1) of the device was fabricated on the membrane through the lift-off process and e-beam deposition of 2 nm Cr (adhesion layer) and 12 nm Ni (Ni was used because of its higher thermal coefficient of resistivity than that of Pt). A 200-nm thick Cu layer was subsequently deposited on the sensor leads. This thickness of the Cu layer reduced the lead's resistance to less than 2%

of the total sensor resistance. A 10 nm gold layer was subsequently deposited on the Cu layer to prevent its oxidation and also to enable soldering to the bond pads. Fabrication/pattering of the Cu/Au leads was conducted through the lift-off process.

Two layers of 3022-46 BCB (with a thickness range of 2.4-5.8 μm) were spun on the H-1 sensor to achieve a total thickness of 7.5 μm. Each layer was soft baked after spinning to fix the BCB layer. Soft baking is the recommended process for fabrication of the multilayer BCB structures, since a soft baked BCB has a better surface adhesion to a metalization layer as well as the subsequent BCB layers than the surface of a hard baked BCB layer. It is important to mention that this thickness could also be achieved in a one step spinning process using 3022-57 BCB (with a thickness range of 5.7-15.6 μm), but this was not done because of unavailability. The second temperature sensor (H-2) was fabricated on the BCB layer through the lift-off process. In order to improve adhesion between the BCB layer and the metalization layer, the surface of the BCB layer was etched for 10-15 seconds using O_2/CF_4 Reactive Ion Etching (RIE) to increase its roughness. This was conducted after the O_2 plasma descuming of the patterned photoresist. The center of the sensing elements were aligned, but sensor H-2 was rotated by 180 degrees to allow its sensor leads to be placed on the opposite side of the chip. Figure 5-2 depicts the alignment of the two sensors.

a) Pattern nitride, oxide, and anisotropic etch of the membrane.

b) Fabricate H-1 sensor.

c) Spin and soft bake the first BCB layer.

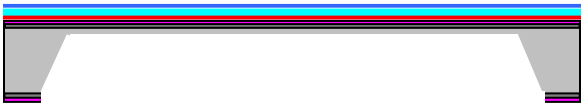

d) Fabricate H-2 sensor.

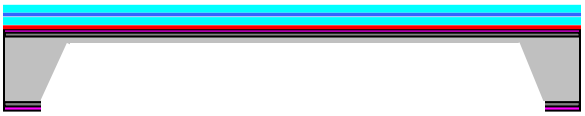

e) Spin and soft bake the second BCB layer.

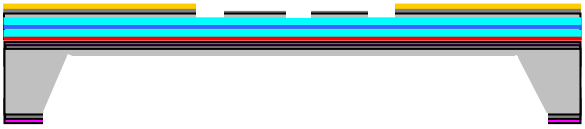

f) Fabricate the sensor array (Cr, Ni, and Au). See chapter 4 for details.

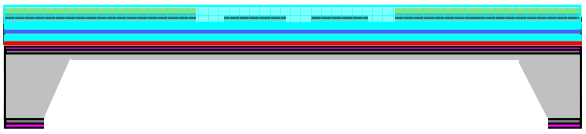

g) Spin and hard bake the third BCB layer on the sensor array.

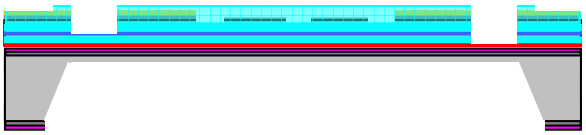

h) Etch the BCB from the bond pad area of sensors.

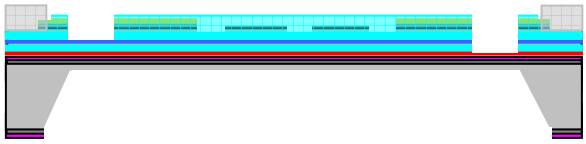

i) Etch the Cr/Ni/Au bond pad and fabricate Ti/Al bond pads.

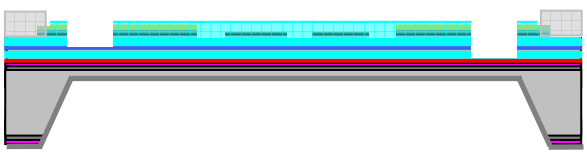

j) Deposit Al_2O_3 (alumina) on the backside of the membrane.

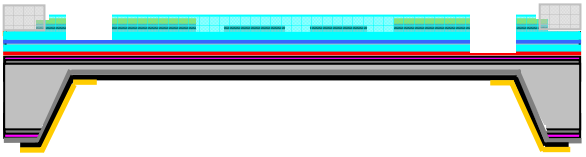

k) Fabricate Cr/Al heater with Cu/Au bond pads.

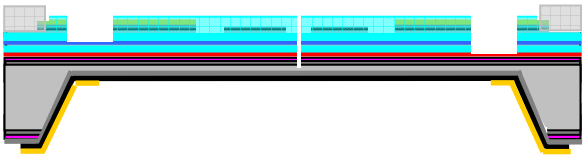

l) Fabricate the cavities using ion mill.

Figure 5-1: Microfabrication sequence of the 2nd generation sensor.

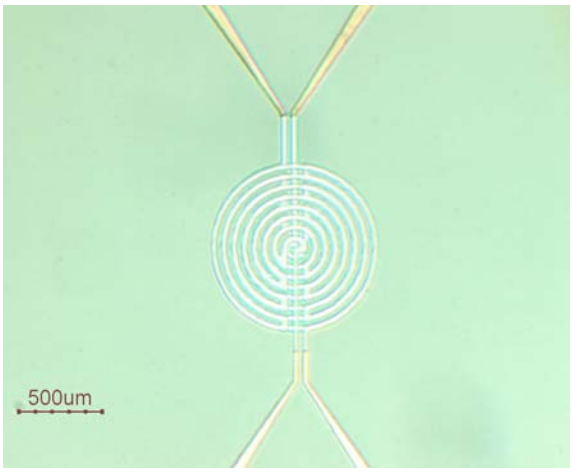

a) wide view

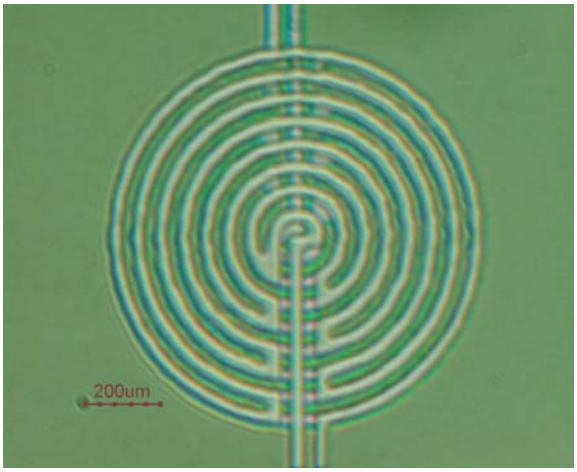

b) close view

Figure 5-2: Main heat flux sensor consists of a BCB layer sandwiched between two temperature sensors H-1 and H-2.

A 2.5-μm thick BCB layer was then spun and soft baked on the H-2 sensor. The temperature sensor array and leads (S-1 to S-13) were then fabricated on the BCB layer through the lift-off process and e-beam deposition of 3 nm Cr, 12 nm Ni (Ni was used because of its higher thermal coefficient of resistivity than Pt), and 200 nm Au. The sensor line width in the 2nd generation device was decreased from 7 μm to 4 μm in order to increase the sensor resistance. Reducing the sensor line width approximately doubled

the resistance of the sensors compared to that of the 1st generation device. In the next fabrication step, Au was etched from the top of the sensors, leaving only the Cr/Ni resistance elements. A 0.3-μm thick BCB layer was then spun over the sensor array and the entire structure was eventually hard baked. Figure 5-1-g shows the schematic cross section of the device up to this fabrication stage. Figures 5-3 and 5-4 show the sensor array that is aligned with the H-1 and H-2 sensors. The BCB layer on the H-1 and H-2 sensors was etched using O_2/CF_4 RIE. A 0.5-μm thick Al layer (as a hard mask) was used to protect the rest of the surface during the RIE process. The Al layer was subsequently etched away from the surface. The BCB layer covering the bond pads of the sensor array was also subsequently etched using O_2/CF_4 RIE. Photoresist was used to mask the rest of the surface during the etching process.

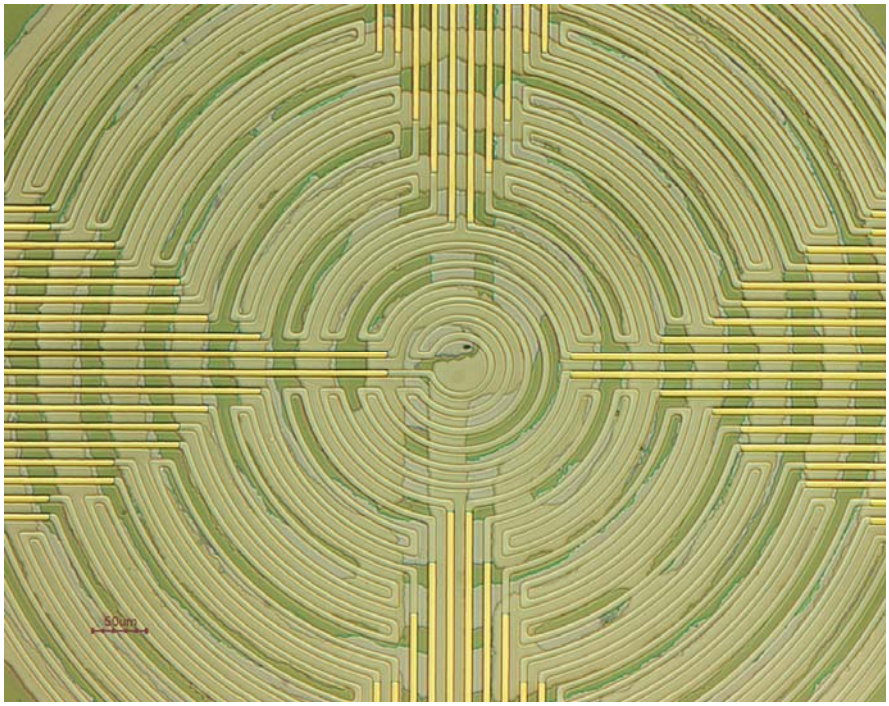

Figure 5-3: Sensor array and its alignment with respect to the H-1 and H-2 sensors.

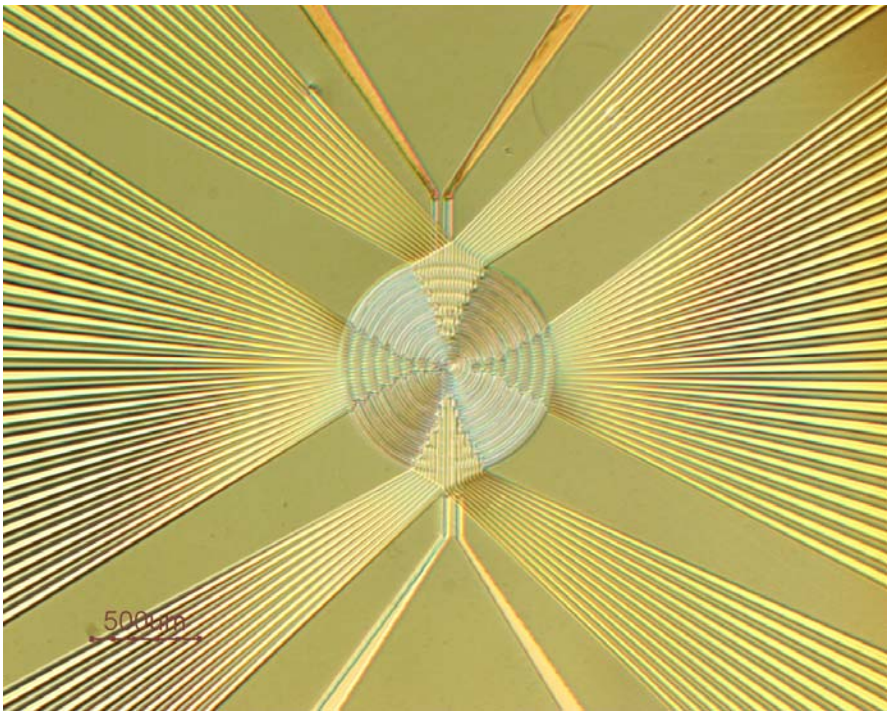

Figure 5-4: Sensors and their leads.

As mentioned in Appendix "A", the bond pads of the 1st generation sensor were made of 5 nm Cr, 20 nm Pt, and 200 nm Au. No difficulties were experienced during the wire bonding to the bond pads of the 1st generation device. In the 2nd generation device,

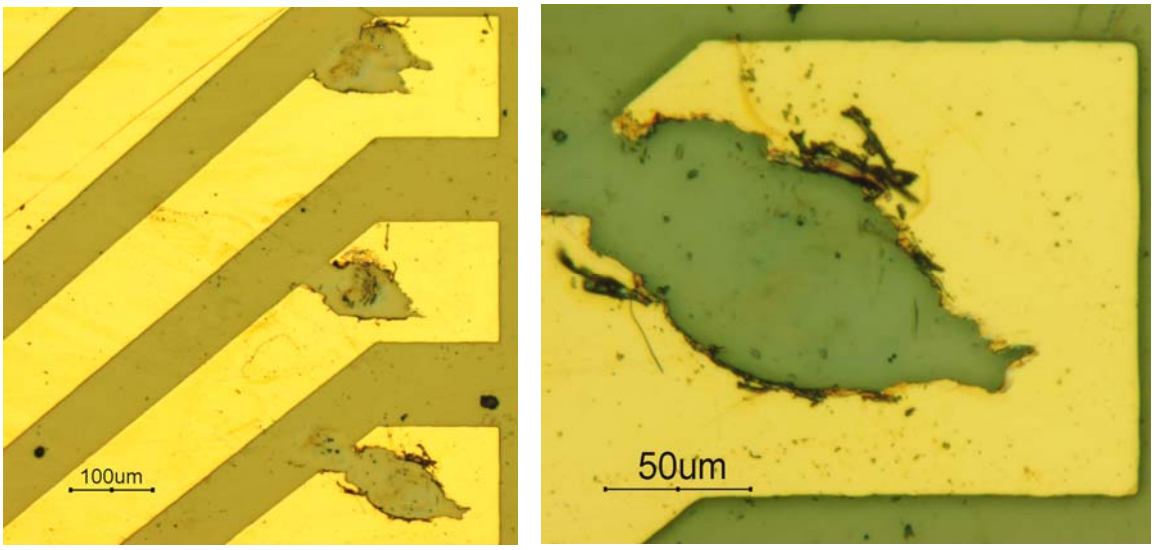

Figure 5-5: Ruptured Cr/Ni/Au bond pads.

however, wire bonding to a similar bond pad failed. As can be seen in Figure 5-5, the bond pads ruptured at the bonding site. Murali et al. (1992) conducted a study concerning wire bonding to bond pads deposited on polyimide films, and have suggested that the compliant nature of the polyimide layer does not allow for efficient coupling of the ultrasonic energy at the bond pad interface (resulting in poor bond quality). They found that using 0.5-μm thick Ti layer between Al pads and the polyimide film significantly improved the wire bonding strength. The compliant nature of the BCB layer was considered to play a similar role in failure of the bond pads as in the case of polyimide. In addition, poor adhesion of the metalization layer to the surface was considered as the second contributing factor in rupture of the bond pads. In order to enhance the adhesion quality between the BCB and the metalization layer, new bond pads were fabricated (see Figure 5-1-i for process sequence) through the sputtering deposition technique. The surface of the BCB layer was cleaned with argon for 1 minute and subsequently 0.5 μm Ti and 0.1 μm Al were deposited on the surface. Deposition through sputtering and using relatively thicker (i.e. stiffer) metallization slightly improved the bond pad quality, but the Al layer thickness had to be increased to 1.5 μm to achieve a reliable wire bonding. Figure 5-6 shows the final Ti/Al bond pads.

The next fabrication step was to make the thin film heater on the backside of the membrane. Before fabricating the heater, a 0.5-μm thick Al_2O_3 layer was deposited on the backside of the membrane to electrically isolate the die from the heater. The Al_2O_3 layer was deposited using RF sputtering technique. The thin film heater was subsequently fabricated on the Al_2O_3 layer through deposition of 3 nm Cr and 6 nm Al using a shadow mask and thermal evaporation deposition. A second shadow mask was used to deposit a

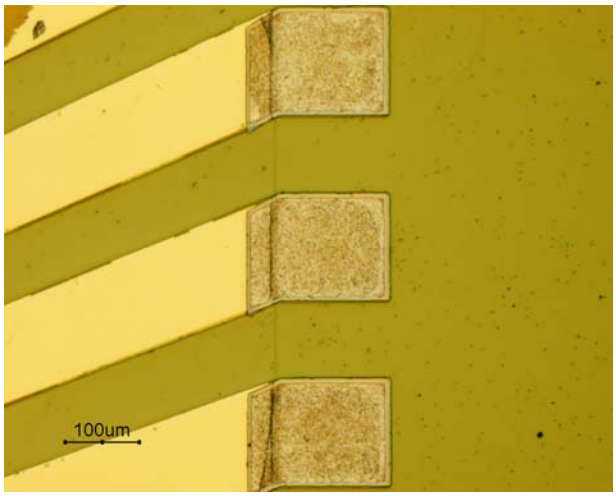

Figure 5-6: 0.5 μm Ti/1.5 μm Al bond pads.

0.5-μm thick layer of Cu on the two sides of the Cr/Al film, leaving a square area of 3×3 mm^2 at the center of the heater/membrane as the actual heater (see Figure 5-7). A 10-nm thick Au layer was subsequently deposited on the Cu layer to prevent Cu oxidation and also enhance soldering to the heater bond pads. The Cu layer reduced the resistance of the heater leads to less than 1% of the total heater resistance thereby diminishing heat release outside the membrane area. Figure 5-7 shows the heater fabricated on the backside of the membrane.

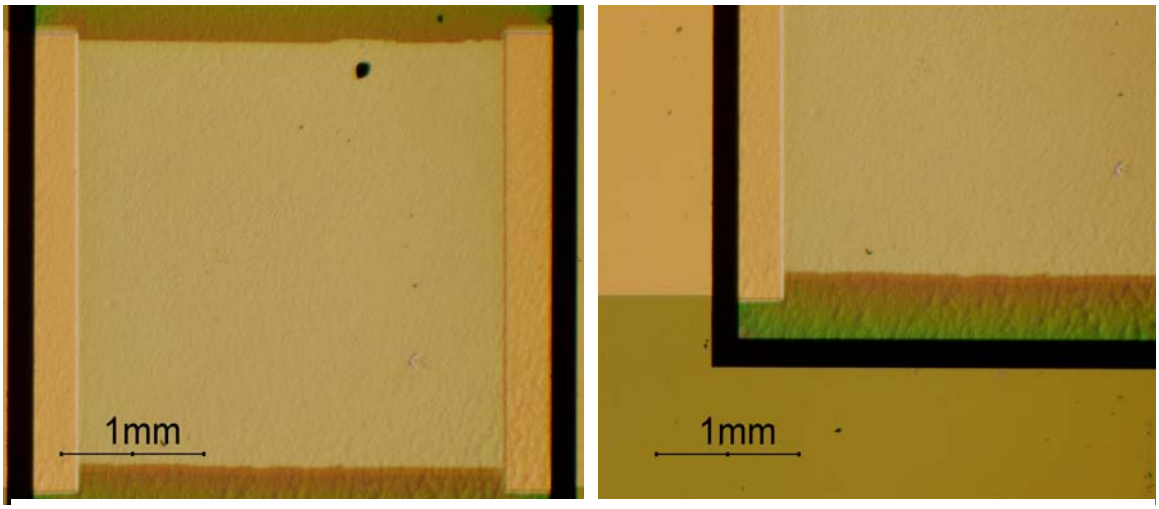

Figure 5-7: Heater on the backside of the membrane.

Lastly, a set of cavities was fabricated at the center of the sensor array. Since microfabrication of high aspect ratio holes in the BCB structure through RIE etching techniques was impractical due to very slow etch rate and some isotropic etching, Focused Ion Beam (FIB) was used to fabricate the cavities. The main issue in using the SEM/FIB machine for this process was that the sensor pattern couldn't be seen inside the machine, preventing the center of the array from being precisely located. This was due to the fact that the conductive sensors were covered by a non-conductive layer of BCB, rendering the sensor array invisible to the scanning electron microscope (SEM). In order to overcome this difficulty, a dummy sensor array was fabricated on the final BCB layer, aligned with the actual sensor array. The dummy sensor array was fabricated by deposition of a 10-nm thick Cr layer through the lift-off process. Figure 5-8 shows a close-up view of the center of the array. The Ion Beam was used to fabricate three

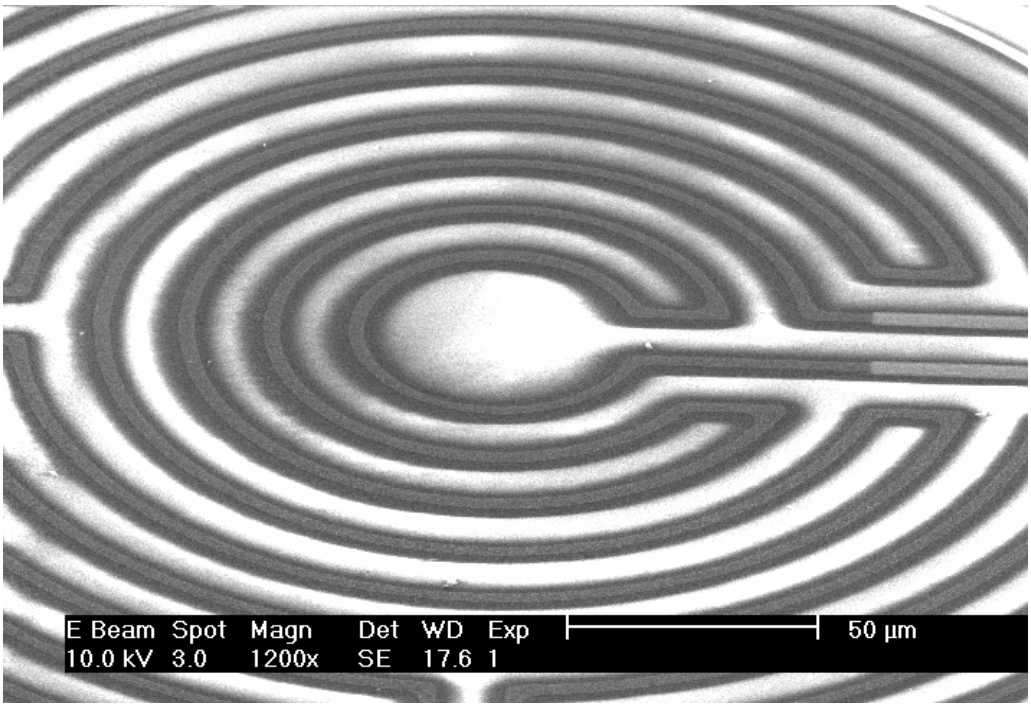

Figure 5-8: SEM image of the dummy sensor array.

cavities at the center of the sensor array. The cavities are 0.7, 1.3, and 2.4 μm in diameter, as shown in Figure 5-9. They are estimated to be approximately 30-μm deep.

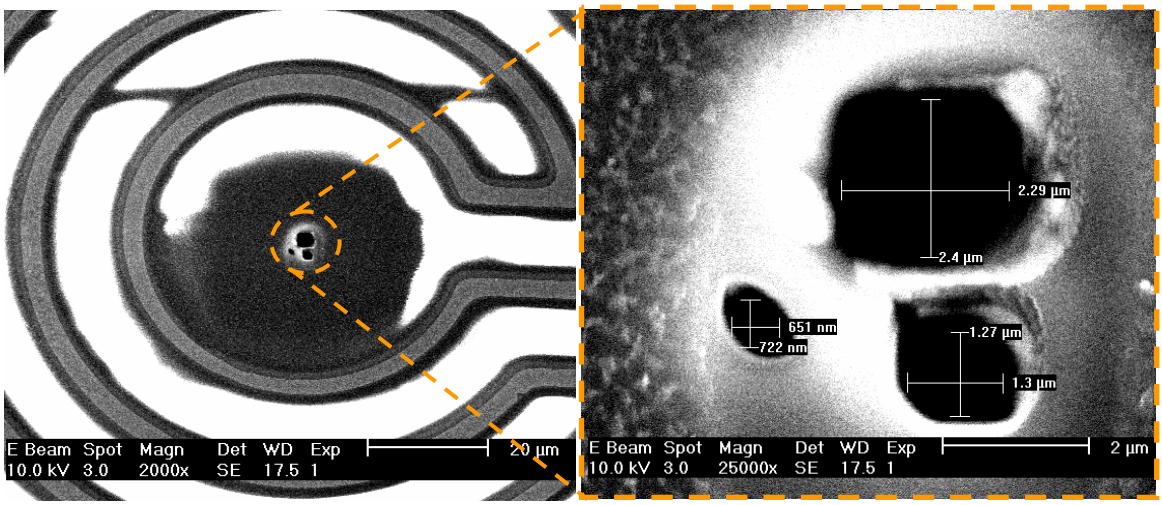

Figure 5-9: SEM image of 0.7, 1.3, and 2.4 μm in diameter cavities fabricated using FIB.

5-2- Measurement of BCB Thermal Conductivity

As shown in Table 3-1, the reported thermal conductivity of BCB varies over a relatively wide range (from 0.18 to 0.24 W/m.K). Using an average value of 0.21 W/m.K results in an uncertainty of 16.6% for a steady state heat flux calculation (i.e. $q = (k_{BCB}/\Delta x)\Delta T$). In order to reduce the heat flux uncertainty, a test article was fabricated to directly measure thermal conductivity of the BCB layer. The measurement concept and details of a test article fabricated for this purpose are discussed in the following.

5-2-1- Fabrication of Test Article

The test article consists of a BCB membrane sandwiched between two temperature sensors. Heat is applied to one side of the membrane and removed from the opposite side. The temperature difference measured between the two sensors and the

applied heat flux are related through $q = (k_{BCB}/\Delta x)\Delta T$, where in k_{BCB} and Δx are thermal conductivity and thickness of the BCB layer between the two sensors, respectively. Measurement of the applied heat flux (q) and the temperature difference between the sensors (ΔT) allows for the calculation of $k_{BCB}/\Delta x$. Since the thickness (Δx) of the BCB layer is known (verified using Veeco NT1100 optical profilometer), its thermal conductivity can be calculated.

Fabrication process of the test article for this measurement is identical to the fabrication process of the 2nd generation device (shown in Figure 5-1) up to step (e). The device at this stage consists of the silicon membrane, H-1 and H-2 sensors with a 7.5-μm thick BCB layer in between, and a 2.5-μm thick BCB layer covering the H-2 sensor. Direct application of heat to the backside of the silicon membrane doesn't provide an accurate account of heat flux passed through the BCB layer, since some of the applied heat dissipates through the sides of the silicon membrane. In order to avoid this problem, the silicon membrane had to be etched and the thin film heater must be fabricated directly on the back of the BCB layer. Figure 5-10 shows the fabrication steps of this device followed after step (e) shown in Figure 5-1. First, a Cr/Au layer was deposited over the BCB layer to protect it from being etched/damaged while the silicon membrane was etched using KOH. The thin film heater was then fabricated on the backside of the remaining BCB membrane. It is important to note that the 0.15-μm thick silicon nitride and the 0.3-μm oxide layers separate the heater from the H-1 sensor. Figure 5-11 shows the top view of the final device.

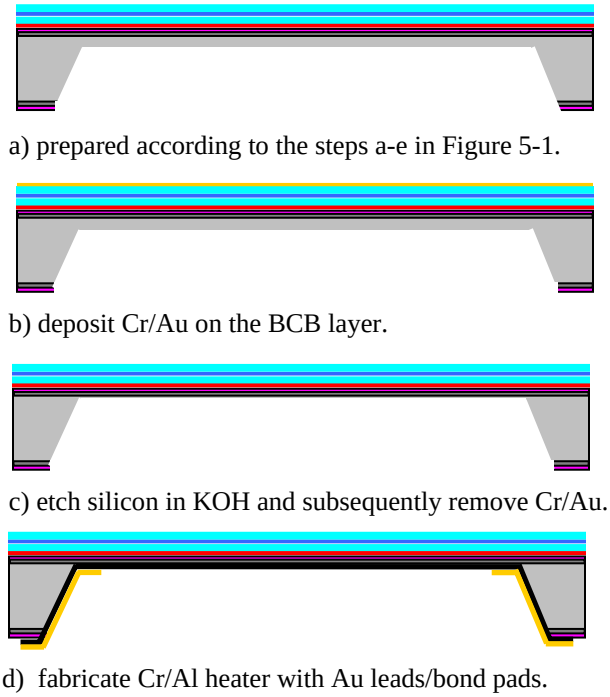

Figure 5-10: Fabrication of test article for thermal conductivity measurement.

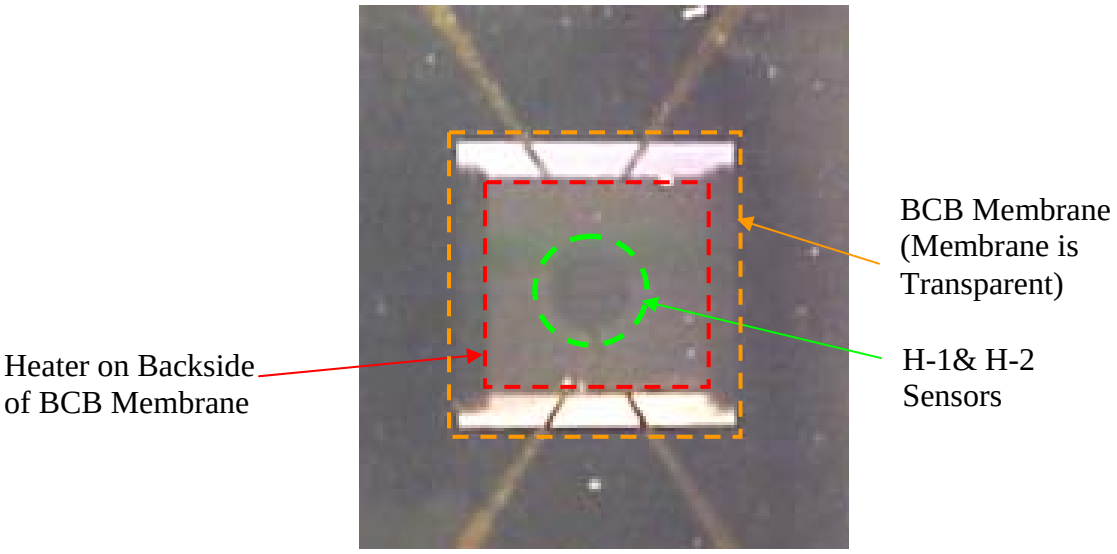

Figure 5-11: Top view of the test device for thermal conductivity measurement (i.e. heat flux measurement calibration).

5-2-2- Test results

The microfabricated test device shown in Figure 5-11 was epoxied to a PGA and the bond pads of sensors H-1 and H-2 were connected to two pairs of PGA pins. The

PGA was then epoxied to the bottom cap of the test chamber (see chapter 4) that is used in the actual boiling tests. The chamber was then assembled and filled with PAO liquid. The two main reasons for selecting this liquid were 1) it doesn't react with BCB and 2) it has a relatively high thermal conductivity (0.136 W/m.K) that allows for better cooling of the BCB surface.

First, temperature sensors H-1 and H-2 were calibrated. An Omega RTD (model DP95-X-RS-41-41-41-41 and probe 438843) temperature calibration device was used for this purpose. This device has an accuracy of 0.01 °C. Resistance of sensors H-1 and H-2 were measured using an Agilent 34401A multimeter. This device can measure resistances of less than 10000 Ω with an accuracy of 0.01Ω. The RTD probe was installed inside the chamber. Temperature of the chamber was adjusted at different levels by adjusting the temperature of the water supplied to the water jacket of the chamber. Resistance of sensors H-1 and H-2 were recorded at each temperature after the temperature readout and the resistance measurement devices were showing a stable reading. The sensors showed a sensitivity of approximately 10 Ω/ºC. The sensors were calibrated with an accuracy of ±0.01 °C.

In order to cool the front surface of the BCB membrane while heat is applied to its backside, a liquid-jet cooling system was added to the setup. As can be seen in Figure 5-12, this system consists of a nozzle, a pre-heater, and a gear pump. The gear pump draws the liquid (PAO) from the chamber and pumps it back over the BCB surface through a supply line. The supply line includes a pre-heater heat exchanger that is immersed in the liquid chamber. The heat exchanger allows the pumped liquid to reach to the chamber liquid temperature before being supplied to the surface. In the absence of the pre-heater,

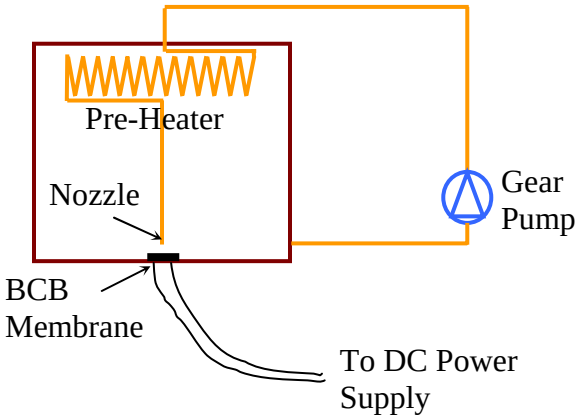

Figure 5-12: Schematic of the test setup for measurement of the BCB thermal conductivity.

the pumped liquid hits the surface with almost the ambient temperature and doesn't allow for testing at elevated temperatures.

Heat was applied to the BCB membrane and temperatures H-1 and H-2 were measured. The minimum temperature difference between sensors H-1 and H-2 was 1.28 °C at a heat flux of 3.28 W/cm^2 and the maximum temperature difference was 4.76 °C at a heat flux of 11.32 W/cm^2. Thickness of the BCB layer between the two sensors (Δx)

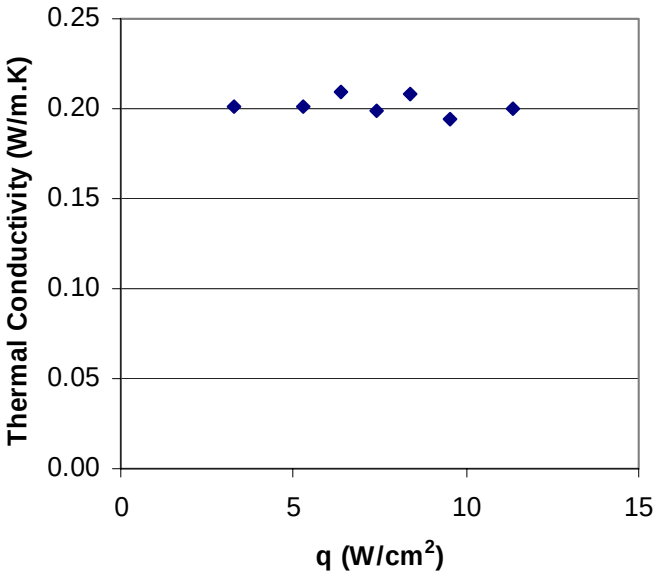

Figure 5-13: Measured thermal conductivity of BCB membrane.

was measured to be 8.3 μm, using Veeco NT1100 optical profilometer. Using these data, thermal conductivity values were calculated. Figure 5-13 shows the results. The average thermal conductivity value was determined to be 0.202 ±0.005 W/m.K.

5-3- Calibration of Bubble Image

To determine the bubble size using the CCD camera images, it was necessary to determine the actual length of a pixel in an image. In order to achieve this, we installed a calibration sphere (see Figure 5-14) with a known diameter at the vicinity of the nucleation site. Knowing the diameter of the sphere (400 μm), we were able to determine the length of an individual pixel within the image (i.e. μm/pixel). The sphere was placed on the surface such that it would be sufficiently far from the cavity to prevent thermal and hydrodynamic interference with the nucleation process, while still remaining within the field of view and at the same focal depth as the nucleation site. Figure 5-15 shows an example image taken during the bubbling process, in which bubble and calibration sphere can be seen.

Figure 5-14: Micro sphere installed at the vicinity of the nucleation site (calibration sphere is manufactured by Small Particles company).

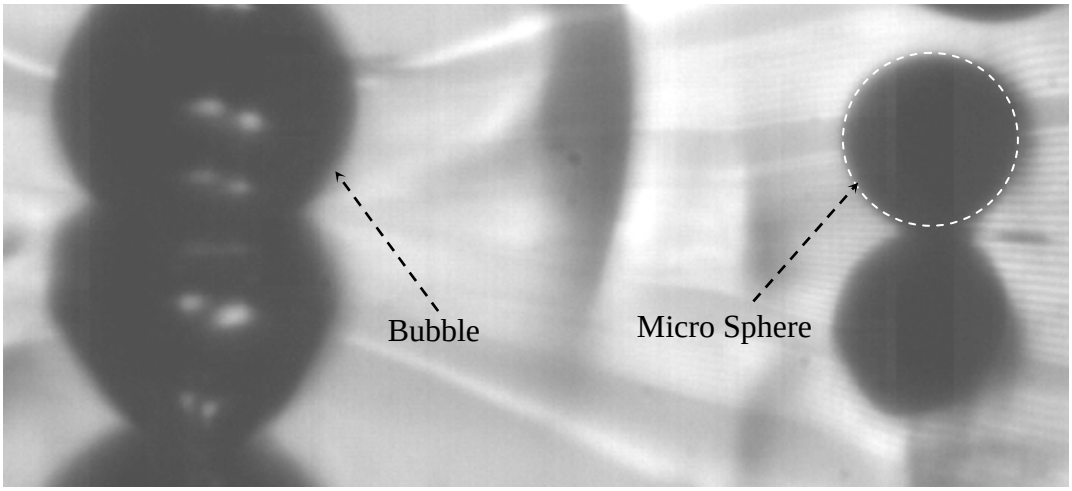

Figure 5-15: Image of the calibration sphere and a bubble during the test.

5-4- Device Packaging

Two wires were soldered to the bond pads of the heater and then the die was epoxied to the PGA. The PGA was eventually epoxied to the bottom cap of the liquid chamber. Figure 5-16 shows the front and back sides of the PGA. Also, a thermocouple wire was attached on a corner of the die to measure its temperature. This thermocouple was used to calibrate all other temperature sensors. Details of the calibration process of

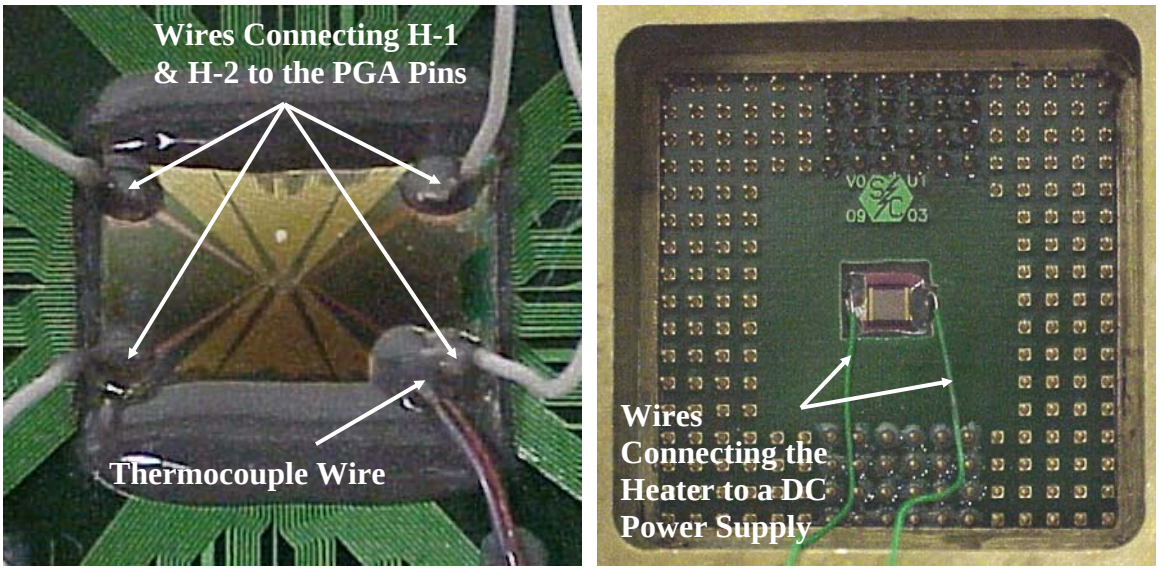

Figure 5-16: Images of the front and back sides of the sensor/PGA.

the sensors are discussed in the following section.

5-4- Calibration of the Temperature Sensors

In order to calibrate the sensors up to a temperature of about 90-95 °C, the test chamber was charged with FC-77 liquid. The boiling point of this liquid at atmospheric pressure is 97 °C. The die temperature was measured with an accuracy of ±0.1 °C using the thermocouple installed on its corner (see Figure 5-16 for the thermocouple position). During the calibration process, it was found that at high chamber temperatures, the die temperature was approximately 5 degrees less than the chamber liquid temperature. This was most likely due to heat loss from the bottom of the PGA to the ambient. However, the die itself is expected to be at isothermal condition when no heat is applied to the heater. In order to increase the calibration temperature of the sensors above 90 °C, the Signal Conditioning Card (SCC) was disconnected from the PGA. Then, the bottom of the chamber was sealed using a metallic plate. A Kapton heater was also attached on the bottom of the metallic plate to heat it up to the chamber temperature. Using this procedure, temperature sensors H-1 and H-2 were calibrated with an accuracy of ±0.1 °C. These sensors were used in the next step to calibrate the sensor array, while SCC was connected to the PGA. In this case, the thin film heater was powered to increase the sensor array temperature. Temperature difference between the sensor array and H-2 is expected to be much less that 0.1 °C, which is the calibration accuracy.

CHAPTER 6: EXPERIMENTAL RESULTS OF THE 2ND GENERATION DEVICE

The experimental results determined using the 2nd generation sensor array are presented and discussed in this chapter. The results include the surface temperature data during the nucleation process along with the synchronized images of the bubbles at different test conditions. A numerical model has been developed to determine the surface heat flux using the experimental temperature data. The numerical heat flux results were used to calculate heat transfer from the surface that can be directly attributed to the different mechanisms of microlayer evaporation, transient conduction, and bubble induced convection. Furthermore, the results were used to determine the microlayer thickness/profile and its contribution to the bubble growth. The digital bubble images were analyzed to quantify the apparent bubble/surface contact diameter, bubble volume (or equivalent spherical radius), and the first and second time derivatives of the bubble radius. The temporal history of the bubble size has been used to calculate the order of magnitude variation of the different stress terms acting on the bubble (inertia, surface tension, and viscous) that influence the bubble growth. Finally, variations of the above-mentioned parameters with surface and liquid temperatures were analyzed.

6-1- Experimental Conditions and Data Reduction

Although nucleate boiling is sensitive to a wide variety of fluid and surface parameters, for the work presented in this thesis, only a single working fluid (FC-72) was studied across a range of wall superheat temperatures at saturated conditions (Tests 1 through 4). Nominally, these tests produced nucleation conditions in which there was no

perceptible waiting time in between bubbles. There was, however, a single anomalous test in which a significant waiting time was generated (the waiting time was approximately 30% of the bubble cycle). The surface and liquid temperatures were set to the same as the conditions of case 1. It is not known what caused this one test to generate an ebullition event with a finite waiting time (perhaps a small amount of surface contamination), but even so, it was a stable event that generated very repeatable bubbles within the duration of the test. Despite repeated trials to reproduce these conditions, the surface always generated bubbling events with no waiting time. Since the presence of a waiting time between bubbles had a noticeable alteration in the bubble dynamics, this data is included in the results as test condition 5. Finally, two tests were conducted at slightly subcooled liquid temperatures for comparison, but not over a comprehensive range of superheat values (test condition 6 and 7). Although not a precise match, each of these tests has an approximate correspondence to a nominal case at saturated condition through similarity of the wall temperature (case 6 corresponds to case 2, and case 7 to case 3). Surface temperature was increased to about 135 °C to initiate nucleation. Table 6-1 provides a list of experiments conducted at different surface and liquid temperatures.

Table 6-1: Experimental conditions.

Test No.	Surface Temperature	Liquid Temperature
1	80.5	56.7
2	86.4	56.7
3	91.4	56.7
4	97.2	56.7
5	80.2	56.7
6	87.5	51.5
7	90.1	52.7

In order to set the stage for a full analysis and comparison of these data, an explanation of how the temperature and image data have been processed to determine the relevant quantities of interest are presented. First, the temperature data were used to calculate the surface heat flux using the numerical model described in the following section.

6-2- Numerical Model of the BCB Layer

The numerical model of the BCB layer was implemented using the commercial software Icepack software (developed by the Fluent Inc.). Figure 6-1 shows how a section of the BCB layer was considered for modeling. As will be shown later, since the temperature results were found to be axisymmetric, modeling of only a section of the BCB layer was sufficient to determine the heat flux values. This helped to reduce the mesh count and consequently saved computational time. The numerical model for each test case includes sensors with variable temperature (starting from sensor S-1) and an additional sensor right after the last sensor with variable temperature. For example, the model shown in Figure 6-1 is used for test cases that their furthest sensor (from the center) with variable temperature is sensor 7. The area covered by sensor 8 shown in Figure 6-1 is equal to a diameter of 676 μm. This model is sufficient for most test conditions expect for the highest surface temperature (test No. 4), in which sensors 9 and 10 were also added to the model. Heat flux at areas that are not included in the numerical model can be directly calculated using the temperature difference between each sensor and the H-1 sensor in combination with a Fourier steady conduction equation. Details of the numerical model are discussed in the following.

- Maximum mesh size:

- x-direction: 1 µm
- y-direction: 3 µm
- z-direction: 2 µm
    - First mesh close to the surface: 0.2 µm

- This mesh size was determined after several mesh refinement steps until a mesh

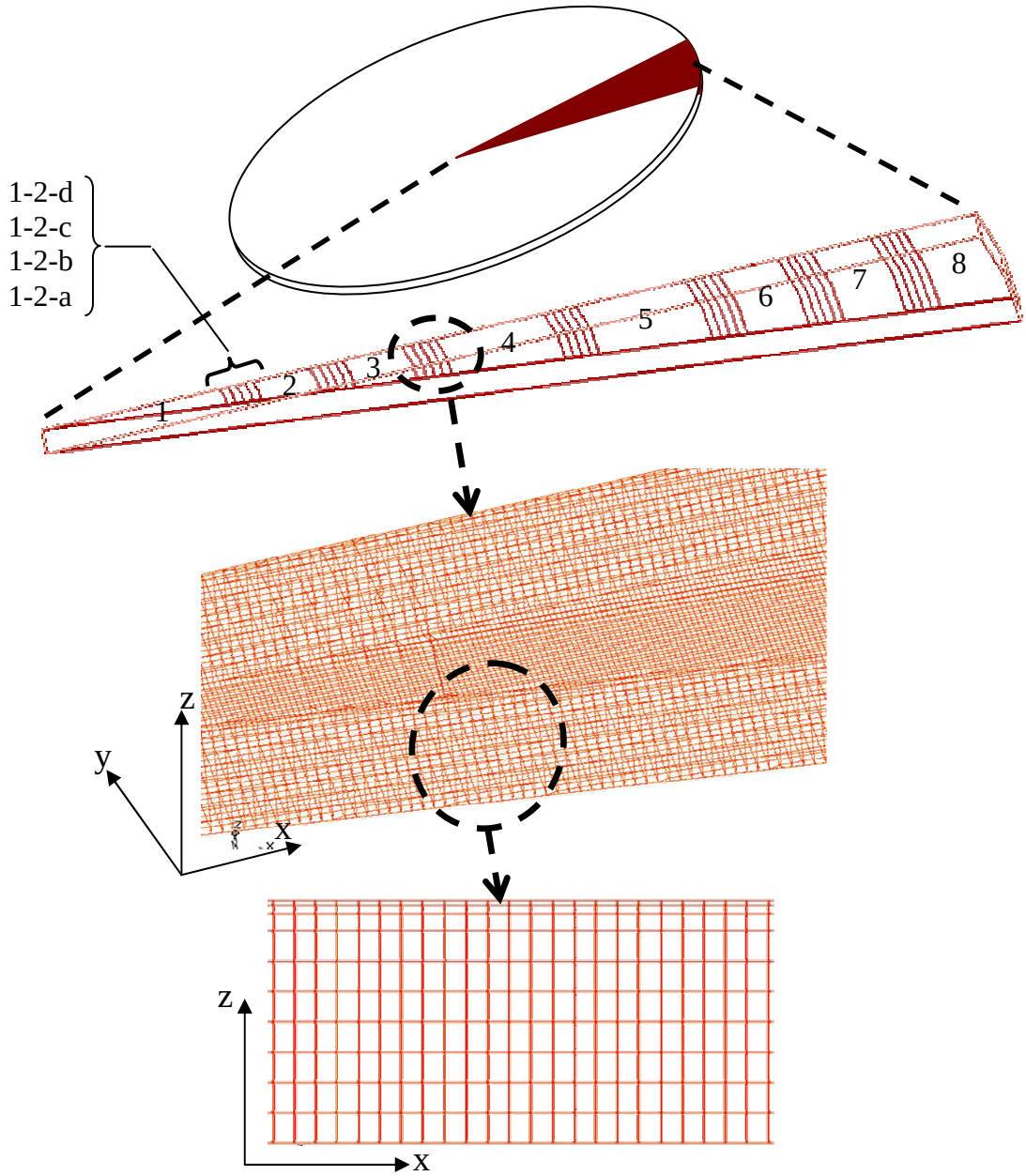

Figure 6-1: Numerical model of the BCB layer.

independent solution was achieved.

- Time step:
  - 25 μsec
- Convergence criteria in each time step:
  - Normalized energy residuals less than 10^{-15}
- Discretization scheme:
  - Second order
- Number of nodes:
  - 144791

The area covered by each element of the sensor array is defined as a separate wall (numbered from 1 to 8), as can be seen in Figure 6-1, to which the corresponding experimental temperature values are applied. The existing 10-μm wide spaces between the neighboring sensors are divided into four sections. The temperatures of these sections are determined through a linear interpolation between the temperatures of the two neighboring sensors. For example, temperatures of the four sections (see Figure 6-1) between the neighboring sensors 1 and 2 are as follow

$$T_{1-2-a} = 0.8T_1 + 0.2T_2$$

$$T_{1-2-b} = 0.6T_1 + 0.4T_2$$

$$T_{1-2-c} = 0.4T_1 + 0.6T_2$$

$$T_{1-2-d} = 0.2T_1 + 0.8T_2$$

The other boundary conditions of the model are; constant temperature H-1 on the backside of the model and adiabatic on its three sides. The entire model was initially set

at an arbitrary temperature close to the average surface temperature. As will be discussed later, the initial condition effect on the results diminishes in less than 2 ms.

6-3- Experimental Results and Analysis

In this section, the test data (surface temperature data and images of the bubbles) for one test condition are presented and the processing procedure of the data to determine characteristics of the nucleation process is described. This is followed by a summary of the results for the remaining conditions. Finally, a comprehensive discussion of the relevant difference between the cases is presented.

6-3-1- Results for Test Condition No. 2

Figure 6-2 shows a sequence of images describing a single ebullition cycle at an average surface temperature of 86.4 ºC and a liquid temperature of 56.7 ºC (test 2). In order to assess the degree of symmetry of the bubbles and how well they are centered within the sensor array, temperature data from several sensors at different radial and azimuthal positions are compared in Figure 6-3. Comparison of sensor S-3a with S-3b (note that sensors S-1 and S-2 are unique), and sensor S-4a with S-4c suggests excellent surface temperature symmetry. The temperature traces have similar magnitudes (typically within 0.5 °C over a 10 °C range of variation), with only a slight phase shift visible in sensor S-4 that is typically less than 0.15 ms. However, the variation in the S-5 sensors is slightly larger, most notably around the time of 10 ms. A potential reason for these slight differences is that a small eccentricity of the bubble might cause less difference in temperature of the counterpart sensors within the contact area than the boarder sensors S-5. Note that the contact line resides at the middle of sensors S-5 (a to d) at its maximum diameter and a few microns difference in the affected area (by microlayer evaporation or

transient conduction) could cause a sizeable difference in the temperature and heat flux at that region. However, temperatures of sensors S-5a and S-5d are considered close and the overall thermal field could be considered quite symmetric. Although temperatures of sensors of different quadrants are quite similar and each could be conveniently used as a representative of all quadrants, the average value based on all available sensors at a given radius has been determined and used for calculating the surface heat flux. Figure 6-4 shows the averaged temperature data.

In order to show the similarity of different bubbling events, a graph of temperature data for several preceding and succeeding bubbles to the bubble of Figure 6-2 are presented in Figure 6-5. As can be seen in the figure, the bubbling events are quite similar. This suggests that time averaged values of different parameters such as temperature and heat flux during a single bubble cycle could be conveniently considered as the average of that parameter over any period of time.

6-3-1-1- Analysis of the Temperature Data

Comparison of the bubble images (see Figure 6-2) and the temperature data (see Figure 6-4) shows that formation of a bubble is associated with a sudden surface temperature decrease. The temperature decrease starts at the center of the array (i.e. at sensor S-1) and progress radially outward over the subsequent sensors (S-2 to S-5). Comparison of the bubble apparent contact diameter (see Figure 6-6) with the temperature history shows that the temperature decrease at the location of each sensor starts after the contact line passes over the sensor. This suggests that the observed temperature decrease is due to microlayer evaporation. The beginning of the microlayer evaporation at each sensor is marked on the temperature profiles shown in Figure 6-4. As can be seen in this figure, the surface temperature starts to increase shortly after the initial

decrease. This indicates that microlayer has evaporated to the extent that the sensor is only partially covered (i.e. the true contact line is at a radial position somewhere between the radial edges of the sensor), and that the amount of heat supplied to the surface exceeds the cooling provided by the remaining liquid. The increasing trend in surface temperature continues until the surface temperature reaches the temperature of the silicon substrate (approximately 88 °C for this case, as indicated by the H-1 sensor), once the microlayer fully evaporates (i.e. surface fully dries out).

After the bubble/surface contact area reaches to its maximum diameter, the apparent contact line starts to recede. The receding liquid rewets the dried out areas. This process is associated with a second sudden decrease in surface temperature. As can be seen in Figure 6-4, the receding contact line at about t=10 ms results in renewed decease in temperature of sensor S-5 that had previously decreased due to the microlayer evaporation. Note that the location of this sensor corresponds to the maximum apparent contact diameter. The temperature decrease trend continues when the contact line subsequently passes over sensors S-4 to S-1 as it moves towards the center of the sensor array.

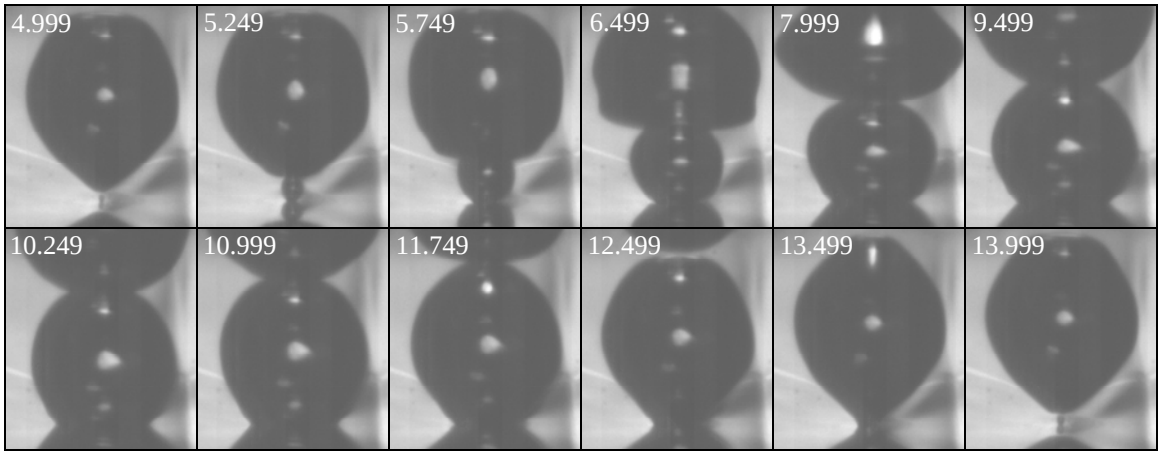

Figure 6-2: A bubbling event at test condition No. 2. The time of each image is shown in the upper left corner of the image (in ms).

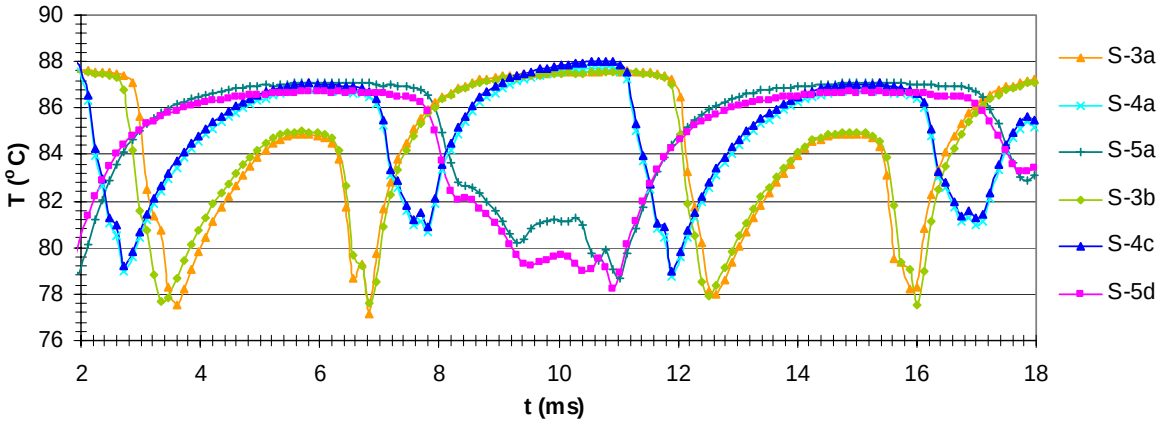

Figure 6-3: Comparison of temperature data at different quadrants.

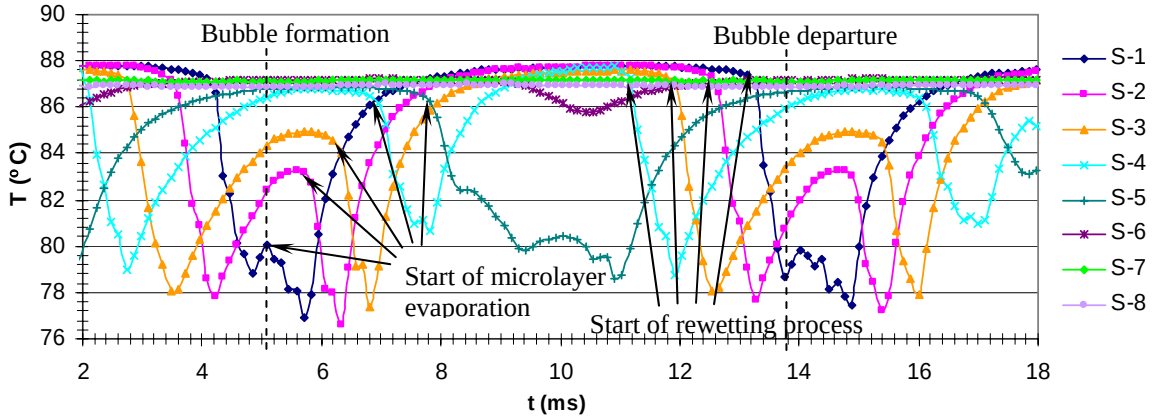

Figure 6-4: Surface temperature variations during the bubbling event of Figure 6-2.

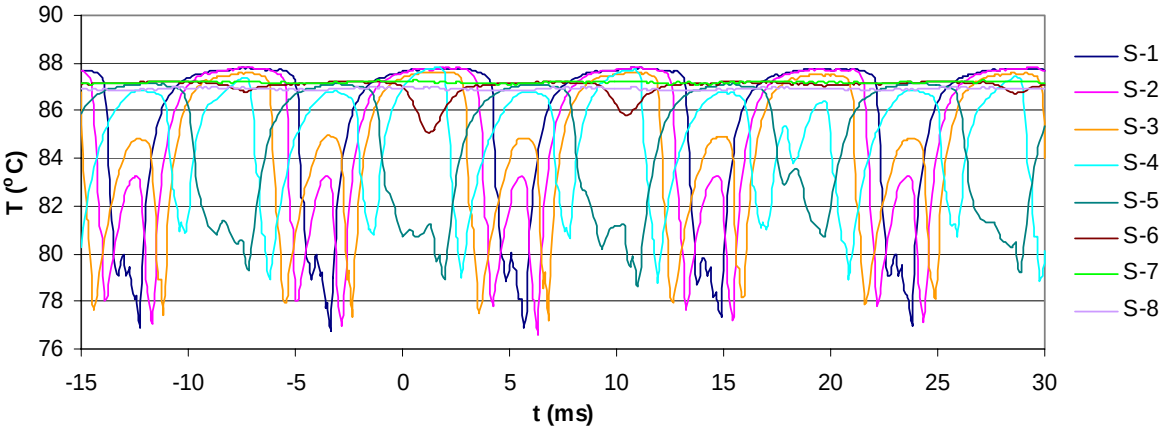

Figure 6-5: Temperature data for bubbling events before and after the bubble formed at t=5 ms (bubble images are shown in Figure 6-2).

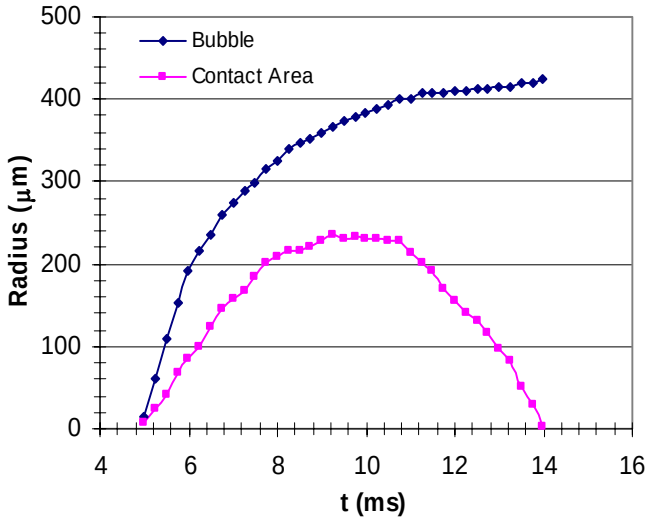

Figure 6-6: Variation of contact area and bubble radius (bubble images are shown in Figure 6-2).

6-3-1-2- Analysis of the Heat Flux Results

The temperature profiles presented in Figure 6-4 have been used in the numerical model of the BCB layer to determine the surface heat flux profiles. As mentioned earlier, since an arbitrary temperature (close to the average surface temperature) was used as an initial condition for the numerical model, the heat flux values of the early part of the solution are invalid. As can be seen in Figure 6-7, heat flux at the central sensors quickly approaches to zero (after about 1-2 ms) that is the correct value of heat flux, as the physics of the problem suggests (see the temperature profiles in Figure 6-4). It should be noted that the surface heat flux becomes zero when the surface temperature approaches to the temperature of the H-1 sensor. Also, starting the solution at time -1 ms did not change the results at time 2 ms. The heat flux values during the first 2 ms are excluded from the solution and the final results are shown in Figure 6-8.

As can be seen in the figure, the start of microlayer evaporation process at t= 5 ms results in heat flux spikes of up to about 30 W/cm^2 over the contact area. The durations of these spikes are in the order of 1 ms. The area under the heat flux curves (marked in red)

shows the local energy transfer from the surface during the microlayer evaporation. The integral over time of the heat flux profiles of sensors S-1 to S-5 is proportional to the total energy per unit area transferred from the surface resulting from evaporation of the microlayer. The heat flux values were multiplied by the area of their corresponding sensors and summed together to determine the overall energy transfer due to microlayer evaporation. Figure 6-9 shows the total cumulative heat transfer from the surface due to microlayer evaporation. As can be seen in the figure, the microlayer energy amounts to 0.032 mJ at the end of the process.

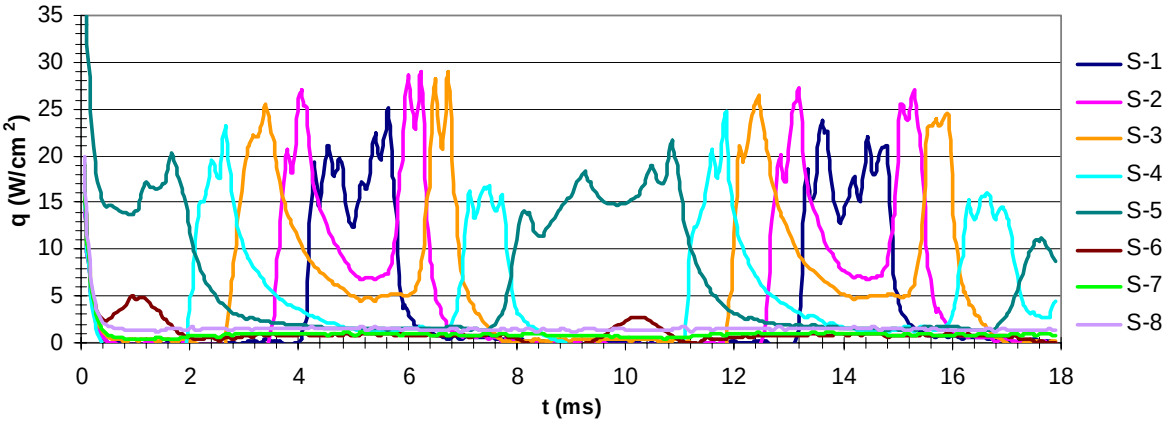

Figure 6-7: Effect of initial condition on the heat flux calculation. Heat flux at the central sensors approaches to zero during the first 1-2 ms of the solution.

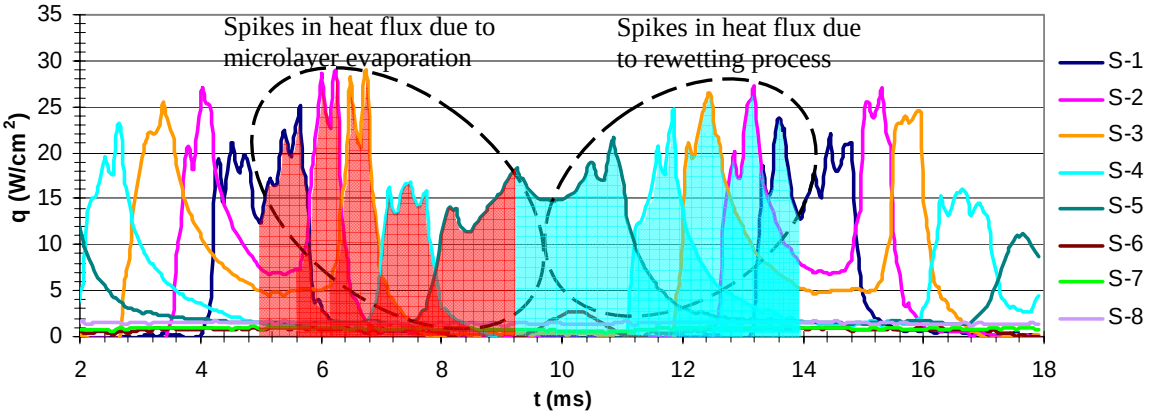

Figure 6-8: Heat flux results corresponding to the temperature data of Figure 6-3. Heat transfer due to microlayer evaporation and transient conduction are marked in red and cyan colors, respectively.

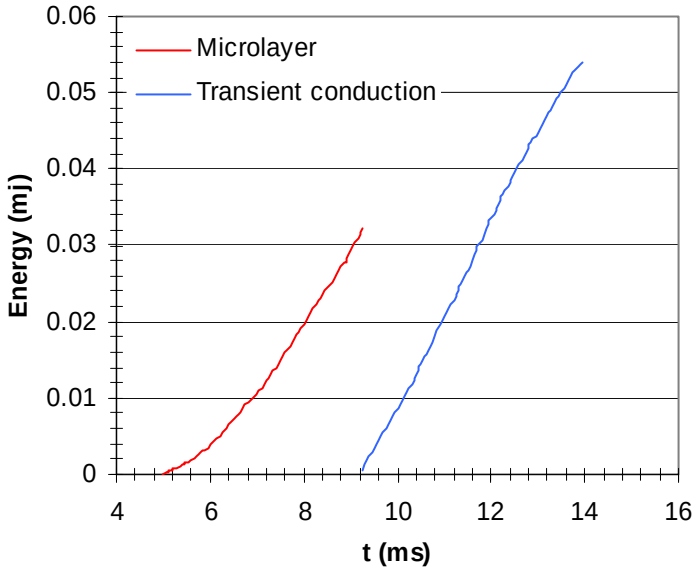

Figure 6-9: Rate of energy transfer from the surface due to microlayer evaporation and transient conduction, and rate of energy transfer into the bubble.

The temperature and heat flux results can also be used to determine the microlayer thickness. The microlayer evaporation energy can be broken into two parts: 1) direct heat transfer from the heated wall ($\int_{t_{m,i}}^{t_{m,e}} q_{s.m} A dt$) during the microlayer evaporation, where in $q_{s.m}$ is the wall heat flux during the microlayer evaporation and $t_{m,i}$ and $t_{m,e}$ are times marking the beginning and end of the microlayer evaporation, respectively, and 2) the initial sensible energy of the liquid microlayer trapped beneath the bubble ($mC\Delta T$). The sum of these two components is related to the microlayer evaporation energy through the following equation.

$$\int_{t_{m,i}}^{t_{m,e}} q_{s,m} A dt + mC\Delta T = mh_{fg} \tag{6-1}$$

where in ΔT is the difference between the initial temperature of the microlayer and the saturation temperature of the liquid. Equation 6-1 can be expanded to the following form

$$\int_{t_{m,i}}^{t_{m,e}} q_{s,m} A dt + \rho_l A \delta_0 C\Delta T = \rho_l A \delta_0 h_{fg} \tag{6-2}$$

After canceling A and rearranging the terms, δ_0 can be determined as follow

$$\delta_0 = \int_{t_{m,i}}^{t_{m,e}} q_{s,m} dt \Big/ \left(\rho_l h_{fg} - \rho_l C \Delta T\right) \tag{6-3}$$

Before one could use Equation 6-3 to calculate the initial microlayer thickness, the initial equivalent superheat temperature of the microlayer (ΔT) should be determined. Since the surface temperature and heat flux at the time of microlayer formation are known, the initial temperature profile in the vicinity of the wall can be directly calculated. Figure 6-10 shows a schematic of the liquid temperature profile during the transient conduction heat transfer process. Knowing the surface heat flux, the slope of the temperature profile at the liquid and surface interface, $dT/dy = q/k_l$, can be determined. Since the microlayer is only a few microns thick, the temperature profile within the microlayer can reasonably be approximated as linear. Since the temperature of the bottom of the microlayer film is equal to the wall temperature and temperature gradient within the liquid is determined, the average temperature of the microlayer and thereby ΔT can be calculated.

Using Equation 6-3, the initial (maximum) thickness of the microlayer on each sensor was determined and presented in Figure 6-11. The total microlayer energy can

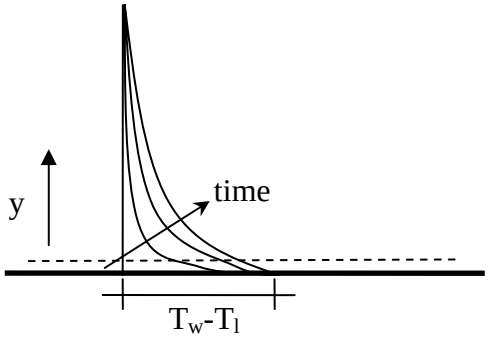

Figure 6-10: Schematic of temperature profile within the liquid before the microlayer formation.

then be determined using the following expression.

$$Q_m = \rho_l A \delta_0 h_{fg} \tag{6-4}$$

It is important to emphasize that the microlayer profile shown in Figure 6-11 does not physically exist on the surface at any time during the microlayer formation and evaporation. This is due to the fact that the microlayer rapidly evaporates as it forms over the surface, so its thickness over all the sensors is never simultaneously equal to the

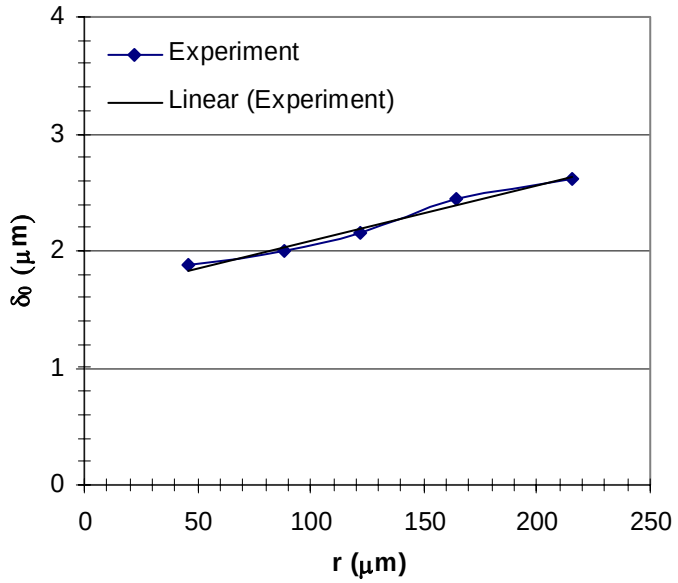

Figure 6-11: Microlayer thickness at different radius.

initial thickness. Heat flux results suggest that microlayer fully evaporates at small radius even before it forms at larger radius. Thickness of the microlayer would have been equal to what is shown in Figure 6-11, if it had not evaporated before it was fully formed. Presentation of the microlayer profile in this format is important, since it allows comparison of the results with theoretical models developed for estimating the initial microlayer thickness/profile.

As mentioned earlier in the discussion of the temperature results, when the contact line starts to recede at t = 9.25 ms, the contact area experiences a second dramatic

increase in heat flux (see Figure 6-8). This dramatic increase in heat flux is most likely a result of the strong transient conduction that occurs as the cooler liquid surrounding the bubble rewets the surface left dry by the evaporation of the microlayer, as postulated by Mikic and Rohsenow (1969). As was done for the microlayer evaporation, the rate of energy transfer from the surface during the transient conduction process was calculated by multiplying the heat flux values by the area of the corresponding sensors and adding them together. Figure 6-9 shows the rate of surface heat transfer during this process. The cumulative transient conduction heat transfer per unit area of each sensor has also been calculated and presented in Figure 6-12.

Although the determined heat transfer value represents the transient heat conduction due to surface rewetting by the bubble shown in Figure 6-2, it doesn't accurately represent the entire transient conduction heat transfer during this bubbling event. A more accurate account of transient conduction heat transfer during this bubbling cycle (5 ms to 14 ms) can be determined by taking into account the transient conduction

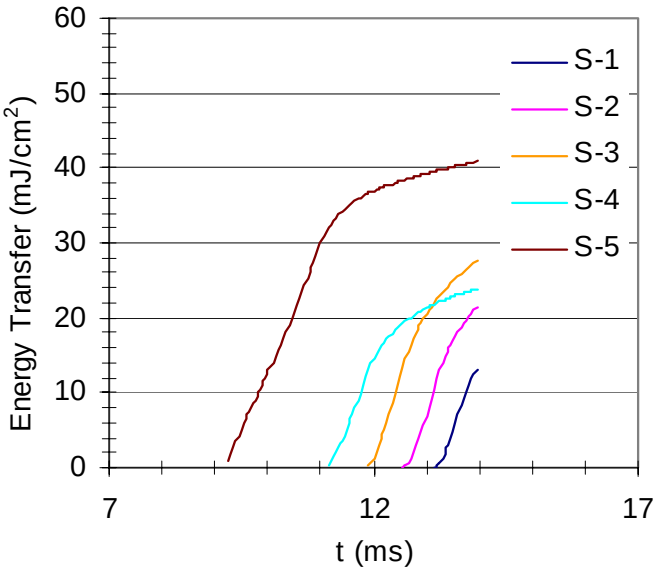

Figure 6-12: Local transient conduction heat transfer.

heat transfer at sensor S-2 during the time period of 5 ms to 5.6 ms and at sensor S-3 during the time period of 5 ms to 6 ms. This transient conduction heat transfer that is the reminder of the surface rewetting by the preceding bubble amounts to 2.2 μJ. This represents 3.9% of the total transient conduction heat transfer from the surface.

6-3-1-3- Bubble Image Processing

The bubble images were analyzed using a matlab program to determine the radius of the bubble and its apparent contact area with the surface. The matlab program takes the profile of the bubble perimeter with an accuracy of ±1 pixel (each pixel is approximately 5.2 μm, determined using the calibration sphere) and determines the bubble volume, assuming that it is axisymmetric. The equivalent radius of the bubble is then determined using the bubble volume. As the bubble images show, the bubbles are spherical, so the equivalent radius of the bubble should be close to the actual bubble radius. Using the bubble radius values (shown in Figure 6-6), the rate of energy increase inside the bubble (i.e. energy transfer into the bubble) was calculated. Results of Figure 6-6 were also used to calculate inertia, surface tension, and viscous terms that act on bubble during its growth (see Figure 6-13). These terms are listed in the following (see chapter 2 for a description of these terms).

Inertia: $\rho_l\left(R\ddot{R}+\frac{3}{2}\dot{R}^2\right)$

Surface tension: $\frac{2\sigma}{R}$

Viscous: $\frac{4\mu\dot{R}}{R}$

Results suggest that the surface tension stress is significantly larger than the inertia and viscous terms. Therefore, surface tension stress can be considered the dominant stress term throughout the growth process. The viscous stress is negligible during the entire growth period.

In addition, the bubble images were used to determine buoyancy stress ($(\rho_l - \rho_v)gR$) on the bubble (see Figure 6-13). The buoyancy force is commonly assumed to overcome the surface tension force between the bubble and surface at the

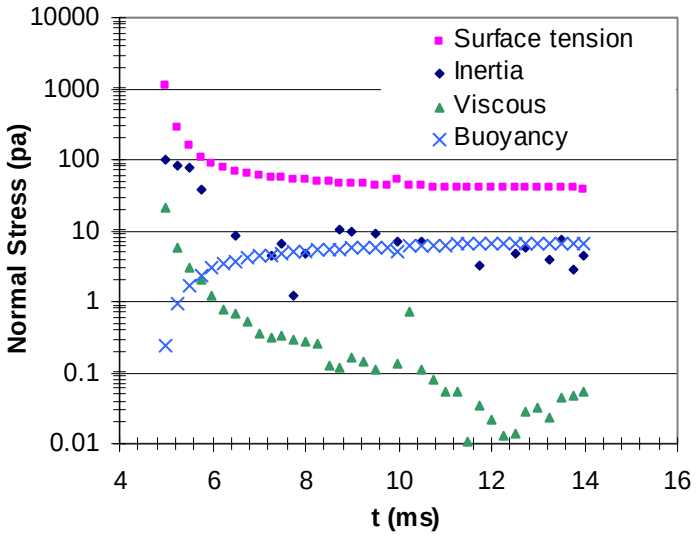

Figure 6-13: Surface tension, inertia, viscous, and buoyancy stress terms.

time of departure. The surface tension force is determined using the following expression.

$$F_S = -\pi d_w \sigma \sin\phi$$

where in d_w is the actual bubble/surface contact diameter and ϕ is the actual contact angle, as can be seen in Figure 6-14.

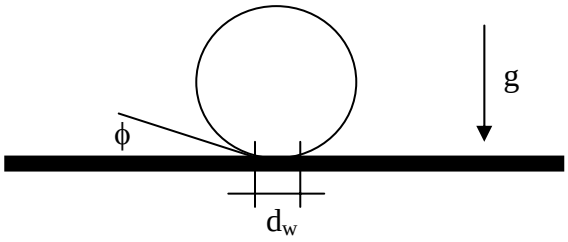

Figure 6-14: Ideal bubble attached to horizontal heating surface.

6-3-2- Experimental Results at Different Test Conditions

Data collected at other test conditions noted in Table 6-1, and the results were found to have a similar degree of axisymmetry and repeatability as test condition No. 2 shown above. The temperature data for a bubbling event for each test condition, the numerical heat flux results, the corresponding images of the bubbles, and the diameter of the bubble and its contact area with the surface are presented in Appendix "B", and the important similarities and differences of the data from the baseline case 2 are noted below.

An examination of the experimental results for the nominally saturated conditions (test cases 1 to 4, Figures B-1 through B-4) reveals that the temperature change patterns are quite similar for the different surface temperatures. As discussed earlier in the analysis of the test results at condition No. 2, the nucleation process is associated with a set of heat transfer processes that are outlined in the following:

1- A radially expanding wave of rapid surface cooling (i.e. increase in surface heat flux) due to microlayer evaporation immediately after the bubble formation and growth on the surface.

2- Surface dryout (i.e. zero heat flux) over the bubble/surface contact area shortly after the beginning of the microlayer evaporation.

3- A second wave of radially contracting surface cooling (i.e. increase in surface heat flux) due to transient conduction process after the contact line recedes (i.e. liquid rewets the surface).

Comparison of the heat flux results at different surface temperatures shown in B-1c to B-4c shows that the maximum surface heat flux during the microlayer evaporation consistently increases with an increase of wall superheat temperature. In contrast to this, a similar trend during the rewetting phase could not be clearly seen.

For the isolated case with a significant waiting time (test 5), the overall pattern of surface temperature, heat flux and their relation with different bubble growth stages are similar to the nominal cases 1 through 4 (with almost no waiting time), but with several important differences. Comparison of the temperature histories (Figure B-5) with those of Figure B-1 shows that waiting time has almost doubled the amplitude of the microlayer evaporation heat flux spikes and reduced their period to about half. The maximum amplitude of the transient conduction heat flux spikes has remained invariant at approximately 20 W/cm^2, although the duration of this process has significantly increased. A more detailed discussion of the implications of these findings will be given later in this chapter.

Finally, for the subcooled data (see Figures B-6 and B-7), the overall trend of the heat transfer events in these two cases is also similar to the other tests that have been presented earlier. Although comparison of test No. 6 with test No. 2 (note that the surface temperatures in the two cases are very close) evidently suggests that subcooling has reduced the bubble growth time, comparison of the heat flux spikes during the microlayer evaporation and transient conduction do not show obvious variation trends. So, further

analysis of the effect of subcooling on dynamics of the nucleation process requires that the exact values of different parameters be calculated and compared, as will be discussed later in this chapter.

6-3-3- Analysis of the Experimental Results

The experimental results presented in the previous section were used to determine different nucleation parameters including the bubble growth rate and departure diameter and frequency, diameter of the bubble/surface contact area, microlayer energy and its contribution into the bubble growth, transient conduction heat transfer, and convection heat transfer outside the contact area. Table 6-2 provides the value of these parameters at different test conditions. The values of these parameters and their variations with surface and liquid temperatures are discussed in the following sections. It should be noted that the discussions are mainly focused on important observations and highlighting the variation trends and differences and similarities among the parameters. Further review of the results and their examination using different heat transfer models and also the comparison of the results with the exiting theories are presented in chapter 7.

Table 6-2-a: Summary of the experimental results at different surface and liquid temperatures.

Test			Diameter and Frequency			Contact Area		Microlayer Energy			Transient Conduction		Outside Convection
No.	T_s (°C)	T_l (°C)	D_b (μm)	f (s^{-1})	D_bf (m/s)	D_c (μm)	D_c/D_b	Q_m (μJ)	δ_0 (μm)	Q_m/Q_b %	Q_{TC} (μJ)	Q_{TC}/A_c (mJ/cm^2)	q''_C W/cm^2
1	80.5	56.7	728	125	0.091	351	0.469	26.6	1.8	11.6	29.2	30.2	0.65
2	86.4	56.7	848	112	0.095	470	0.554	53.2	2.2	14.7	54.0	31.1	1.52
3	91.4	56.7	988	92	0.091	520	0.526	108.4	2.8	18.9	109.0	51.3	2.04
4	97.2	56.7	1110	83	0.092	600	0.540	175.3	3.7	21.6	156.3	55.3	3.04
5*	80.2	56.7	798	112	0.090	508	0.636	53.2	2.2	17.9	43.2	21.3	1.87
6	87.5	51.5	644	146	0.094	444	0.689	37.0	1.6	20.2	41.6	26.8	2.07
7	90.1	52.7	738	130	0.096	450	0.610	55.1	2.2	22.8	56.1	35.2	2.64

* with waiting time (t_g=5.79 ms and t_w=3.16 ms)

Table 6-2-b: Summary of the experimental results at different surface and liquid temperatures.

Test	Surface Heat Transfer per Bubble Cycle			Contribution of Heat Transfer Mechanisms			Average Heat Flux	
No.	Microlayer $Q_{m,s}$ (μJ)	Transient Conduction Q_{TC} (μJ)	**Outside Convection Q_C (μJ)	Microlayer %	Transient Conduction %	Outside Convection %	Contact Area q''_{CA} (W/cm^2)	Over $\pi D_b^2/4$ q'' (W/cm^2)
1	18.6	29.2	16.7	28.8	45.3	25.8	6.18	1.94
2	32.3	54.0	53.1	23.1	38.8	38.1	5.57	2.76
3	58.5	109.0	122.7	20.1	37.6	42.3	7.26	3.48
4	79.3	156.3	251.0	16.3	32.1	51.6	6.92	4.17
5*	35.8	43.2	49.8	27.8	33.6	38.7	4.36	2.88
6	22.2	41.6	24.3	25.2	47.2	27.6	6.01	3.94
7	30.6	56.1	54.5	21.7	39.7	38.6	7.08	4.29

** $Q_C = q''_C \times \frac{\pi}{4}\left(D_b^2 - D_C^2\right) \times \frac{1}{f}$

6-3-3-1- Bubble Departure Diameter and Frequency

Comparison of the bubble departure diameters at saturation conditions (in tests No. 1 through 4) shows that the bubble diameter increases almost linearly with increase in surface temperature, as can be seen in Figure 6-15. Figure 6-15 also shows that increase in bubble departure diameter (D_b) is associated with a decrease in bubble departure frequency (f). The two parameters change in a way that $D_b f$ remains almost constant at different surface temperatures, as can be seen in Figure 6-16. The values of the $D_b f$ parameter in other test conditions (test No. 5 to 7) are also included in the graph. As can be seen in the figure, parameter $D_b f$ for all test conditions is almost the same even though the bubble diameter and frequency significantly change. This is an interesting observation considering that the thermal field, which controls the bubble growth process, varies significantly among different test conditions. Perhaps this can be related to the physical properties of the liquid. The existing knowledge in literature about this result

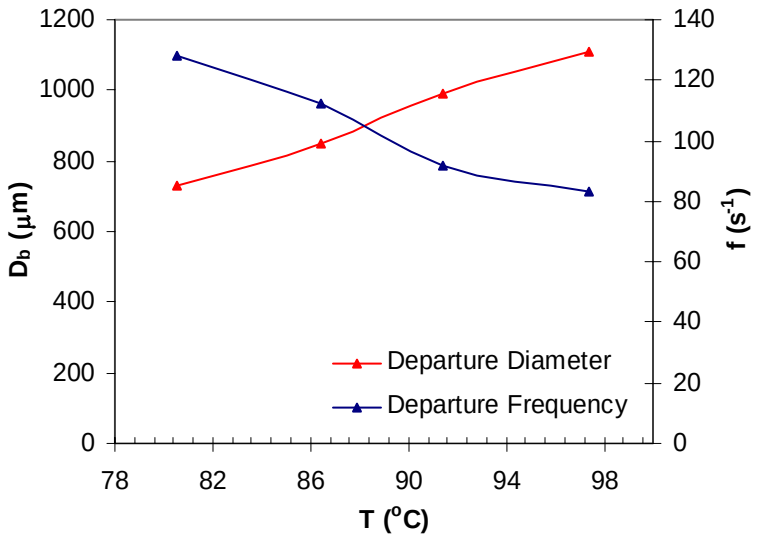

Figure 6-15: Variation of bubble departure diameter and frequency with surface temperature in saturated liquid (tests No. 1 to 4).

will be discussed in chapter 7.

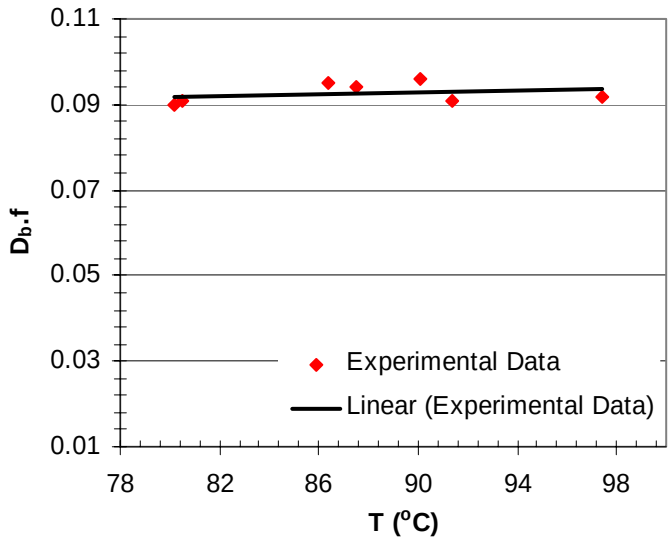

Figure 6-16: $D_b f$ at different liquid and surface temperatures (tests No. 1 to 7).

6-3-3-2- Bubble Growth Rate

Figures 6-17 to 6-19 show the experimental results for bubble growth. The results at saturated liquid and different surface temperatures (tests No.1 to 4) are compared in Figure 6-17. As can be seen in the figure, the bubble growth rate consistently increases with increase in surface temperature. Figure 6-17 also suggests that increasing the surface temperature from 80.5 °C (test No. 1) to 91.4 °C (test No. 3) results in an increase in bubble growth rate in both early and later growth stages. However, increasing the surface temperature from 91.4 °C (test No. 3) to 97.2 °C (test No. 4) only results in growth rate increase at the later stage of the growth process (when bubble is larger than 500 μm in diameter), not at the early growth stage. Comparison of these data with the existing growth models, in chapter 7, provides some explanation about the growth physics in these experimental conditions.

The bubble growth rates at saturated and subcooled liquid conditions are compared in Figure 6-18. Results show that subcooling changes the bubble growth rate

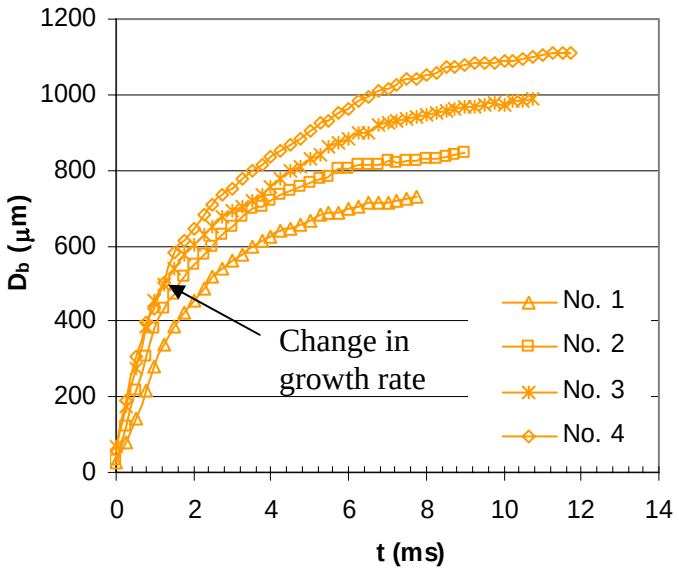

Figure 6-17: Bubble growth rate in saturated liquid. Surface temperature was increased from 80.5 °C at test No. 1 to 97.2 °C at test No. 4.

mainly at the later stage of the growth process, mainly after the bubble reaches a diameter of approximately 500 μm. Results also suggest that at test condition No. 6 the bubble diameter even declines before departure. However, almost no decline in the bubble diameter is observed in test No. 7.

Comparison of the bubble growth rate in tests No. 5 (with a waiting time of 3.16 ms between the bubbles) and No.1 shows a significant difference in growth rate throughout the growth period (see Figure 6-19). The fact that the surface temperature is the same in the two cases suggests that waiting time has significantly changed the balance of different factors that control the bubble growth. As can be seen in Figure 6-20, the inertia term in test No. 5 (Figure 6-20-e) is significantly higher than in the test No.1 (Figure 6-20-a). The growth behavior of the bubble in this test condition is further discussed in chapter 7.

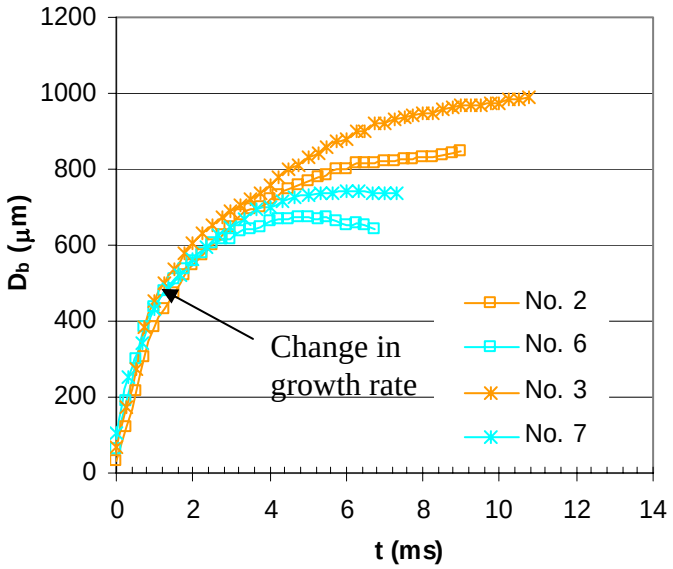

Figure 6-18: Effect of subcooling on bubble growth rate.

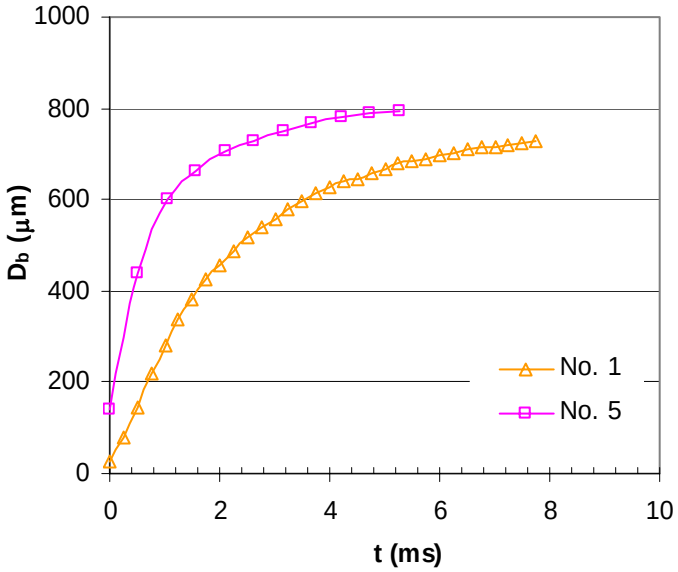

Figure 6-19: Effect of waiting time on bubble growth rate.

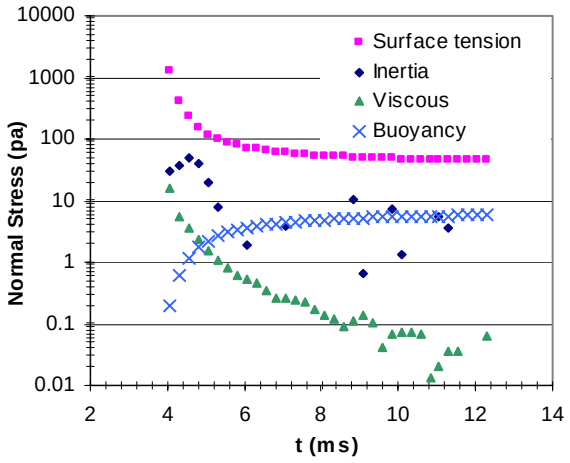

a- Test No. 1

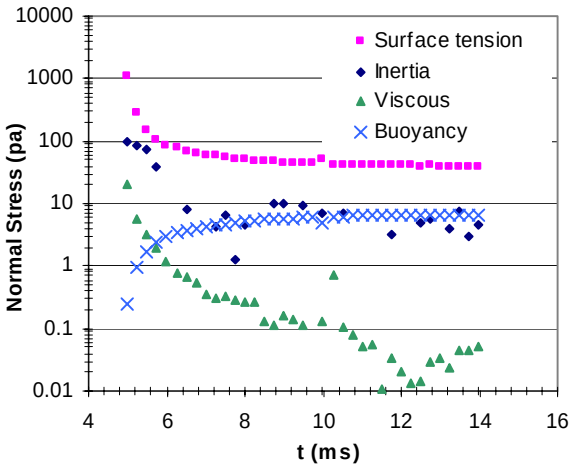

b- Test No. 2

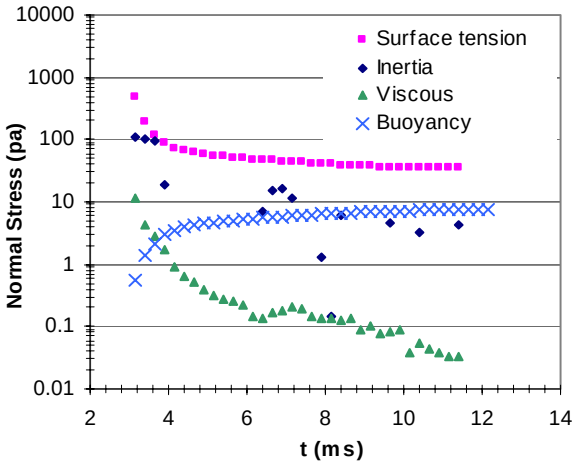

c- Test No. 3

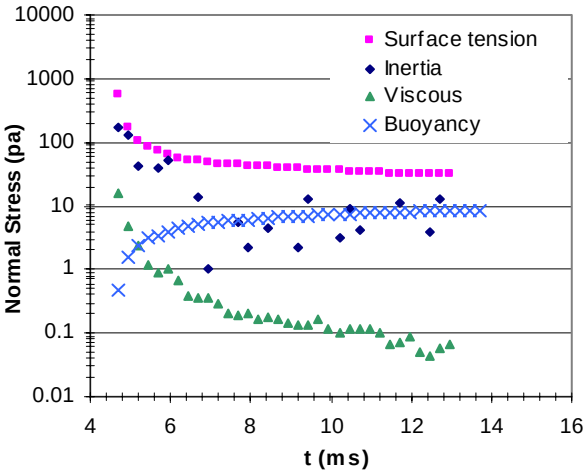

d- Test No. 4

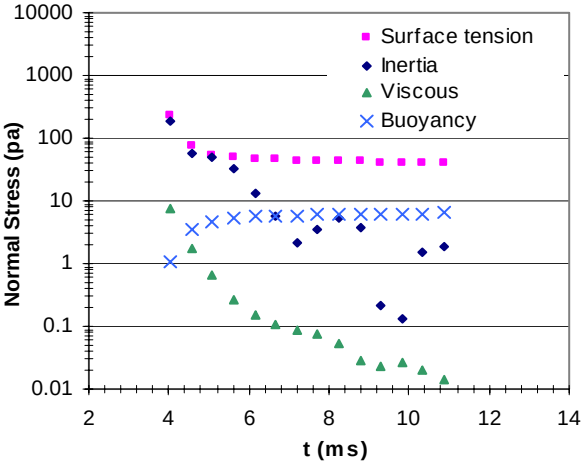

e- Test No.5

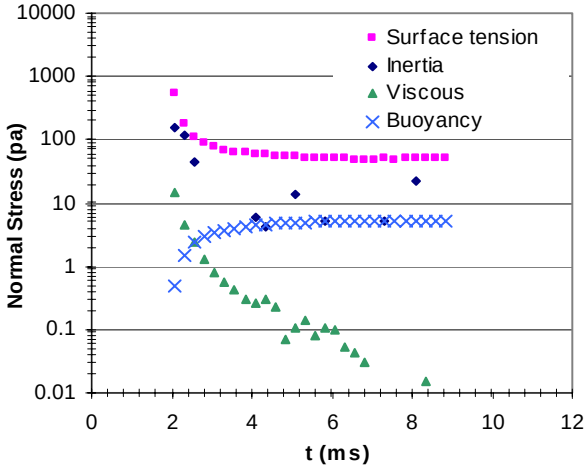

f- Test No.6

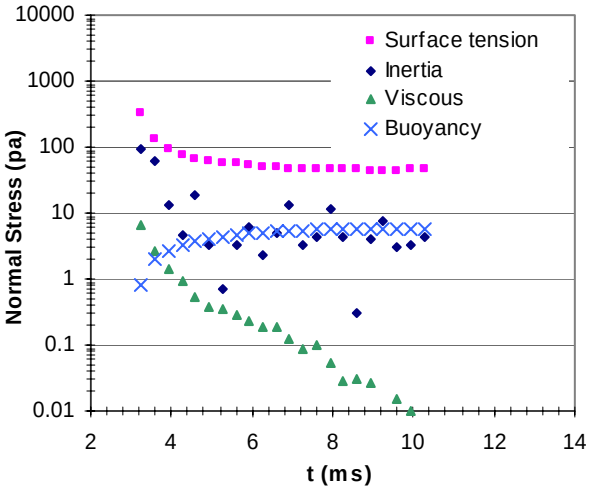

g- Test No.7

Figure 6-20: Normal stress values during the bubble growth at different test conditions.

6-3-3-3- Bubble/Surface Contact Area

Figure 6-21 shows the variation of the apparent bubble/surface contact diameter with surface temperature at saturation condition. As can be seen in the figure, diameter of the contact area linearly increases with surface temperature. Figure 6-21 also shows the

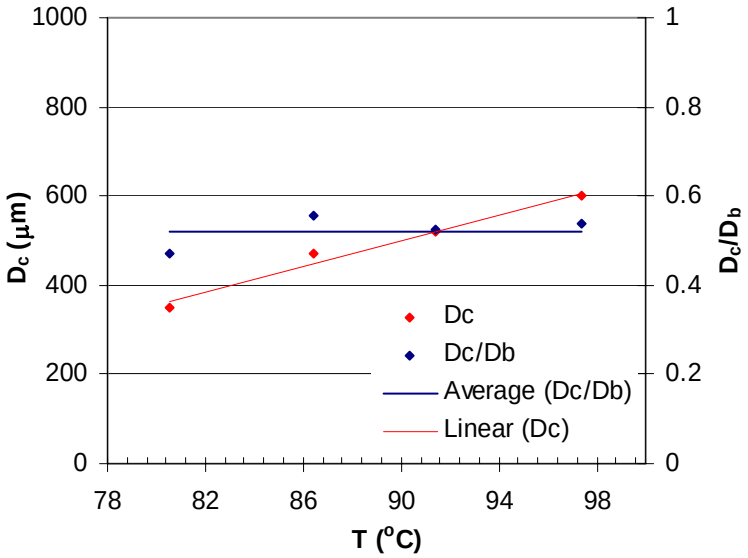

Figure 6-21: Variation of the contact area diameter with surface temperature in saturated liquid.

non-dimensional contact diameter (D_c/D_b). The average non-dimensional contact diameter (D_c/D_b) is 0.522. The maximum deviation from the average value is 16.4% (at test No.1), which implies an approximate geometric similarity of the bubble shape at the time of departure.

Comparison of the contact area diameter reported in Table 6-2 for tests No.1 and 5 shows a significant difference between the two, even though the surface and liquid temperatures are the same. As shown in Figure 6-19, the growth process of the bubble in test No. 5 is very rapid during the initial growth stage. The rapid growth rate of the bubble in this case leads to its hemispherical growth (see Figure B-5-a). Figure 6-22 shows how rapidly the contact area expands at the early stage of the bubble growth in test No. 5.

Comparison of the contact diameter values (see Table 6-2) at subcooled (tests No. 6 and 7) and saturation (No. 2 and 3) conditions indicates that subcooling reduces the

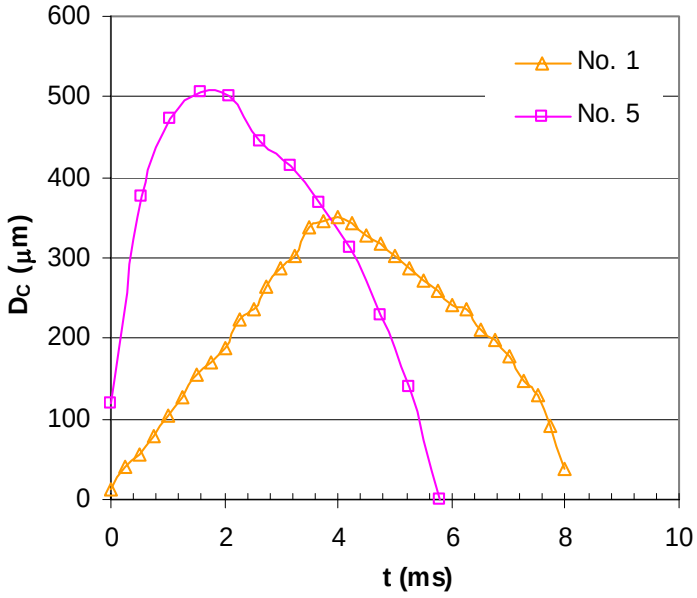

Figure 6-22: Comparison of the contact diameter of tests No. 1 and 5.

diameter of the apparent contact area. Subcooling also reduces the bubble diameter to such an extent that it leads to an increase in non-dimensional contact diameter (D_c/D_b). As can be seen in Table 6-2, the average non-dimensional contact area for the two subcooled tests No. 6 and 7 is 0.65, which is approximately 25% higher than the corresponding value at saturation conditions (0.522).

6-3-3-4- Microlayer Evaporation and Its Contribution to Bubble Growth

As mentioned earlier, the total (sensible and latent) energy of the microlayer can be determined using Equations 6-3 and 6-4. Using these two equations, the total microlayer energy for all test cases were calculated and reported in Table 6-2. Results for tests conducted at saturation conditions (tests No. 1 to 4) are compared in Figure 6-23. As can be seen in the figure, the microlayer energy and its contribution in total bubble energy steadily increase with increasing the surface temperature. The microlayer contribution to the bubble energy at surface temperature 80.5 °C is 11.6%. This contribution increases to 21.6% at surface temperature 97.2 °C.

In order to compare the microlayer thickness at different test conditions, the average of the initial microlayer thickness for all test conditions were determined and listed in Table 6-2. Figure 6-24 compares the results at different conditions. As can be seen in the figure, increasing the surface temperature at saturated liquid conditions results in an increase in the microlayer thickness. Cooper and Lloyd (1969) model was used to determine the variation of the microlayer thickness with surface temperature. As mentioned in chapter 2, Cooper and Lloyd (1969) suggested that the microlayer thickness can be determined using $\delta_0 = 0.8\sqrt{v_l t_g}$ where v_l is the liquid viscosity and t_g is the bubble growth time. This equation gave an order of magnitude higher thickness than the

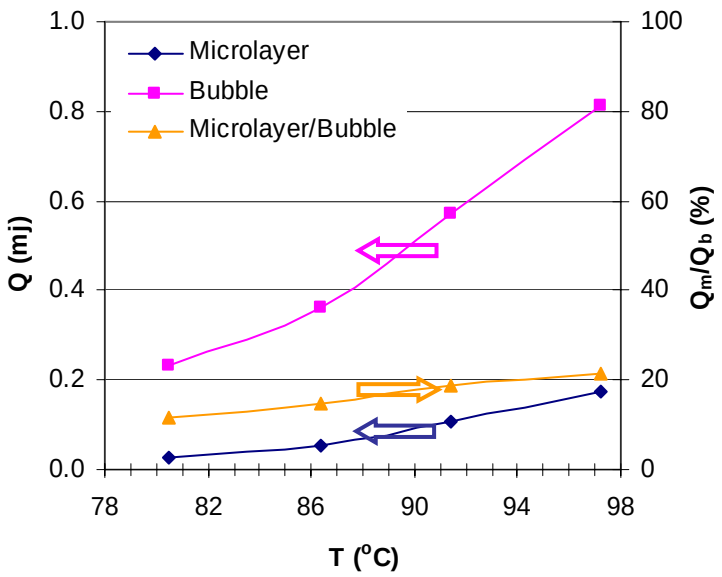

Figure 6-23: Microlayer energy and its contribution to bubble growth in saturated liquid.

experimental results. An arbitrary coefficient of 0.08 was used instead just to make it easier to compare the model and the test results. The liquid viscosity (v_l) was determined at the surface temperature of each test case. The value of v_l decreases approximately 10% from temperature 80.5 °C to 97.2 °C. Figure 6-24 compares the theory with the test results. The theoretical thicknesses are marked with T_No. 1 to 7. As can be seen in the figure, the theory also predicts an increasing trend in thickness with the surface temperature. Comparison of the slope of the theoretical and experimental curves suggests that the change in microlayer thickness is a stronger function of t_g than what is suggested in the Cooper and Lloyd (1969) theory ($\delta_0 \propto t_g^{1/2}$). The theory also predicted a decrease in the microlayer thickness at subcooled conditions compared to the saturation conditions, as determined in the tests cases 6 and 7. This is due to the decease in bubble growth time at subcooled conditions. For the test case 5, while the test result suggested that the waiting time has increased the microlayer thickness, the model predicted a

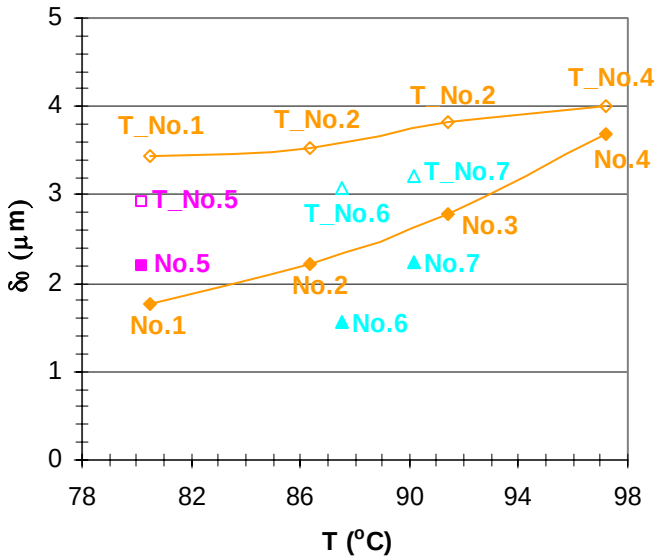

Figure 6-24: Variation of microlayer thickness with surface temperature (experimental and theoretical).

reduction in thickness. This is simply because the model only uses t_g to calculate the thickness.

6-3-3-5- Transient Conduction Heat Transfer

Using the heat flux data, the cumulative transient conduction heat transfer per unit area for each sensor was calculated and presented in Figure 6-25. An immediate observation from the results is that if the transient conduction mode persists over a sensor for more than 1 to 2 ms, the slope of the heat transfer curve significantly declines. An example of this trend can be seen at sensors 5 and 6 in Figure 6-25-c. A plausible explanation for this trend is that after the initial rapid rise of the surface heat transfer, the effect of transient conduction quickly fades away and a steady state heat transfer mechanism (perhaps convection heat transfer) with a more or less constant heat transfer rate controls the heat transfer from the surface. It is important to note that the slope of the curves at each surface temperature is different and depends on the strength of this heat transfer regime.

Comparison of the results of tests No. 1 to 4 that are shown in Figures 6-25-a to 6-25-d suggests that transient conduction heat transfer generally increases with increasing the surface temperature. The two factors that contribute to this increase are 1) an increase in duration of the rewetting process, as can be seen in Figures B-1 to B-7 and 2) an increase in surface and liquid temperature difference. The total transient conduction heat transfer (heat transfer per unit area of the bubble/surface contact area, Q_{TC}/A_C) for all test conditions has been calculated and listed in Table 6-2. Comparison of test results No. 1 to 4 indicates that a decrease in the bubble departure frequency (i.e. increase in bubble growth time) corresponds to an increase in transient conduction heat flux. However, the rate of change for these two parameters isn't the same.

The classical transient conduction theory suggests that the cumulative transient conduction heat transfer is proportional to $(T_s - T_l)$ and $f^{-0.5}$ (Mikic and Rohsenow (1969) determined $\frac{Q}{A} = \frac{2k}{\sqrt{\pi\alpha}}(T_s - T_l) f^{-0.5}$). In order to analyze the dependency of the transient conduction heat transfer results to these two factors, first, cumulative transient conduction per unit area and temperature difference between the surface and liquid was determined. Figure 6-26 shows a plot of $Q_{TC}/A_C(T_s - T_l)$ versus $f^{-0.5}$ ($=\sqrt{t}$). As can be seen in the figure, $Q_{TC}/A_C(T_s - T_l)$ increases with $f^{-0.5}$. Second, the parameter $Q_{TC}/A_C\ f^{-0.5}$ was calculated and plotted versus surface and liquid temperature difference ($T_s - T_l$). Figure 6-27 shows the results. Results suggest an upward trend in $Q_{TC}/A_C\ f^{-0.5}$ as $T_s - T_l$ is increased.

To further analyze the ability of the transient conduction model to predict the experimental results, using the liquid properties, constant $\frac{2k}{\sqrt{\pi\alpha}}$ was calculated and $\frac{2k}{\sqrt{\pi\alpha}} f^{-0.5}$ was plotted in Figure 6-28. Note that $\frac{2k}{\sqrt{\pi\alpha}} f^{-0.5}$ is equal to $\frac{Q}{A_C \Delta T}$, based on transient conduction model. As can be seen in the figure, the transient conduction theory significantly overpredicts the experimental results. The parameter $\frac{2k}{\sqrt{\pi\alpha}} f^{-0.5}$ was multiplied by 0.35 to get a better match with the experimental results. This is as if $\Delta T = 0.35(T_s - T_l)$, which suggests that the rewetting liquid is not at the bulk liquid temperature. Although this arbitrary number provided a relatively good match between the model and the experimental results, more studies are required to examine the accuracy of the transient conduction model.

Comparison of the results of test No. 5 (see Figure 6-25-e) and test No. 1 (see Figure 6-25-a) shows that although waiting time increases the transient conduction time period, it doesn't consistently increase the cumulative heat transfer of all sensors. As can be seen in the figures, while the cumulative heat transfer of sensors S-1 and S-2 increases, those of the sensors S-3 and S-4 slightly declines. Comparison of the parameter Q_{TC}/A_C (see Table 6-2) between the two cases suggests an overall decline in Q_{TC}/A_C in test No. 5 (also see Figures 6-26 and 6-27). Note that the total transient conduction heat transfer (Q_{TC}) in test No. 5 is higher than in test No. 1 (see Table 6-2) due to its larger contact area.

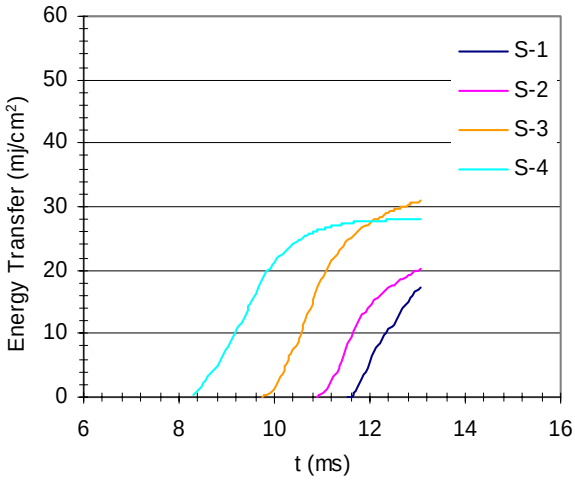

a- Test No. 1

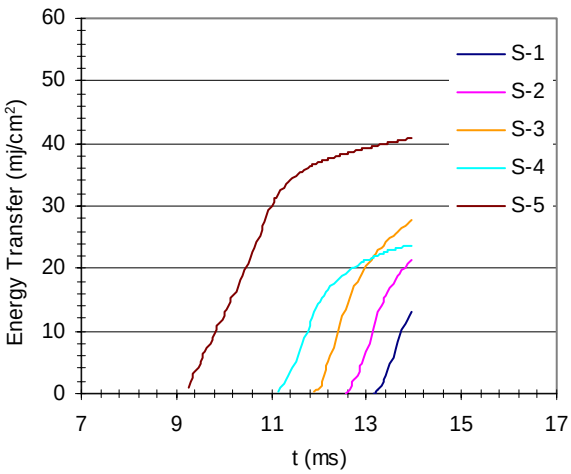

b- Test No. 2

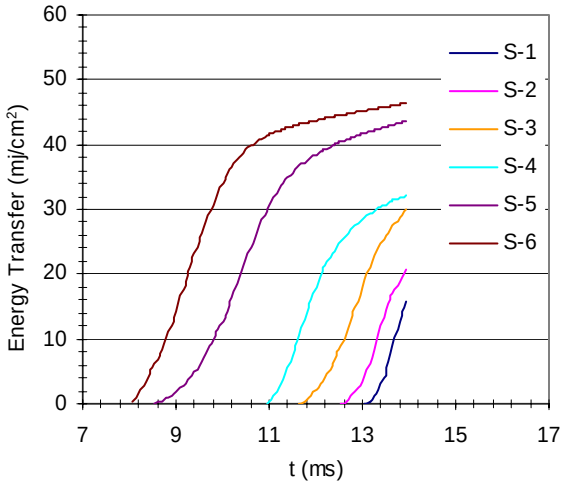

c- Test No. 3

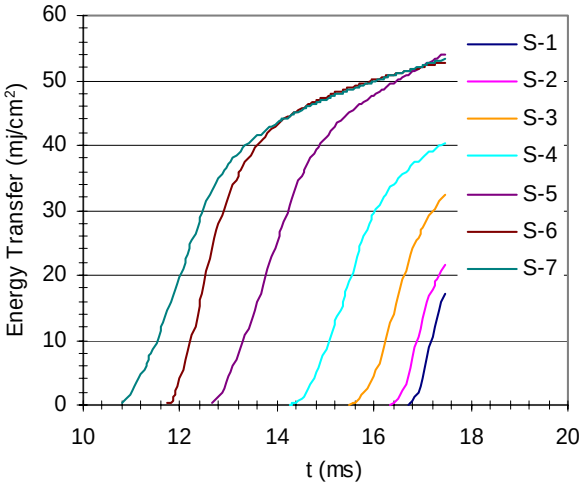

d- Test No. 4

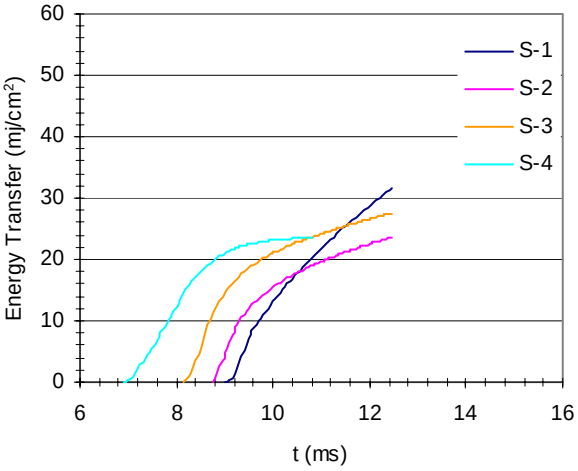

e- Test No. 5

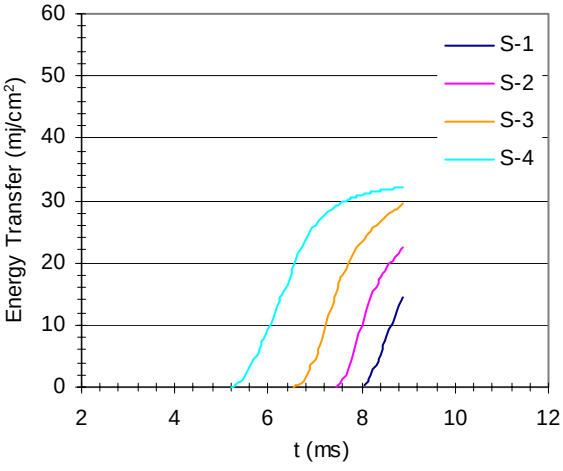

f- Test No. 6

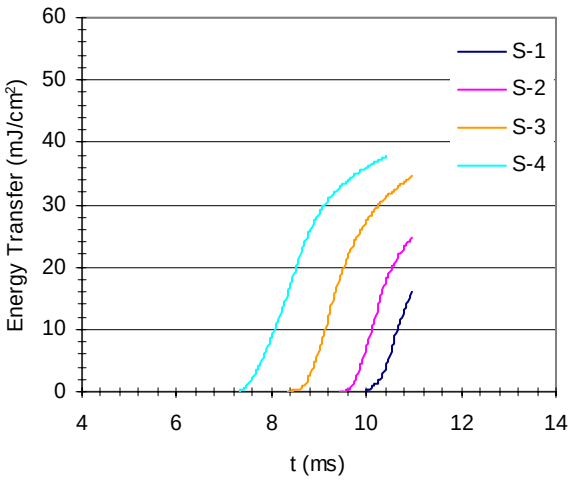

g- Test No. 7

Figure 6-25: Local transient conduction heat transfer at different experimental conditions.

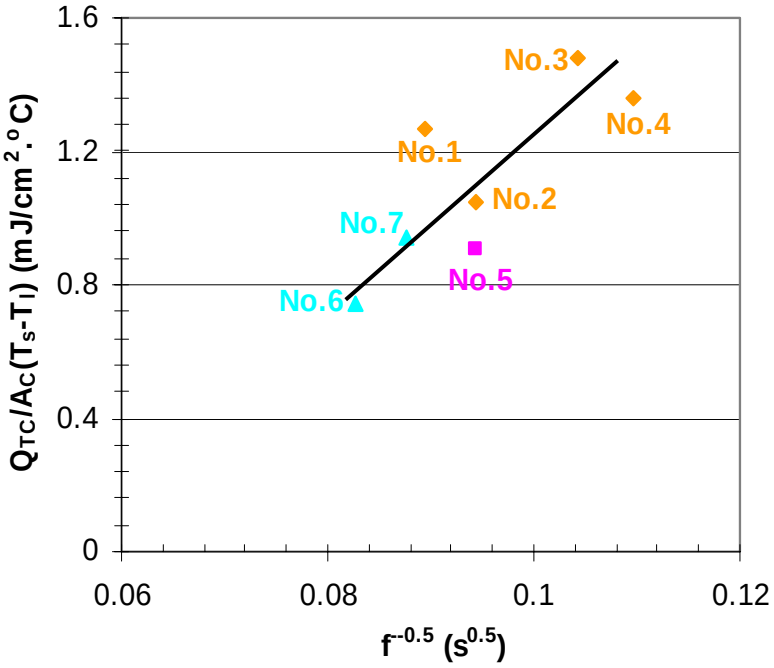

Figure 6-26: Transient conduction per unit area and temperature difference between surface and liquid as a function of $f^{-0.5}\left(=\sqrt{t}\right)$.

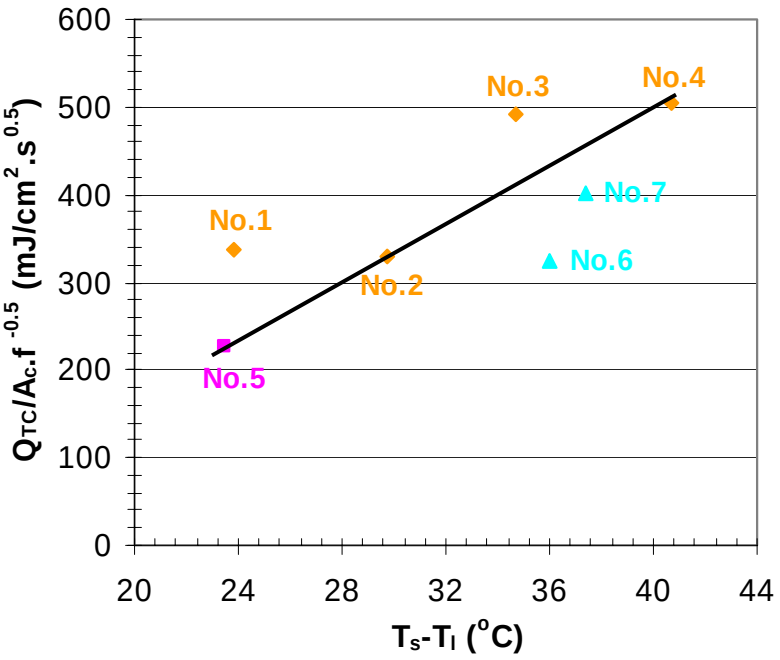

Figure 6-27: Transient conduction per unit area and $f^{-0.5}\left(=\sqrt{t}\right)$ as a function of surface and liquid temperature difference.

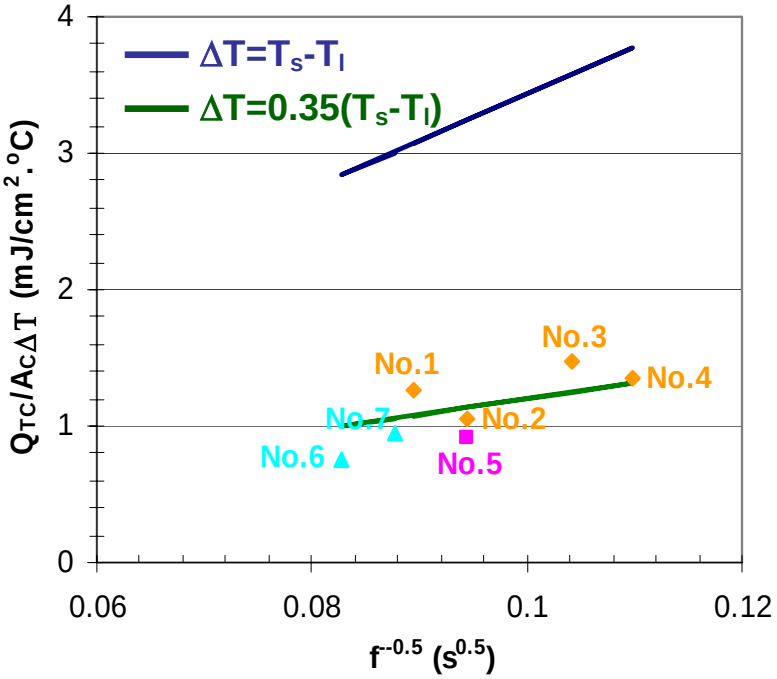

Figure 6-28: Comparison between theory and experiment for transient conduction per unit area and temperature difference as a function of $f^{-0.5}\left(=\sqrt{t}\right)$.

To evaluate the effect of liquid subcooling on transient conduction heat transfer, one can compare the results of tests No. 2 and 3 with tests No. 6 and 7, respectively. It is clear from the results that subcooling increases the cumulative heat transfer of the individual sensors. Perhaps, this is due to the increase of the surface and liquid temperature difference. However, subcooling reduces the overall transient conduction heat transfer (see Table 6-2 and Figures 6-26 and 6-27), since the decrease in contact area at subcooled conditions eliminates the outer sensors from participating in the process. Note that the outer sensors significantly contribute to transient conduction heat transfer process.

6-3-3-6- Heat Transfer Outside the Contact Area

It is evident from all the test cases (see Figures B-1 to B-7) that the heat transfer field (temperature and heat flux) outside the contact area maintains a steady value throughout the nucleation process. This suggests that the rapid expansion of the bubble during the growth and its departure process does not generate strong transient liquid movements outside the maximum contact area that can modify the thermal boundary layer and give rise to transient convection effect in the vicinity of the bubble.

In order to study whether the bubbling event perceptibly alters the heat transfer field outside the immediate contact area, it was decided to measure and compare the surface heat flux generated by natural convection in the absence of a bubble. In general, one can conduct such test using the sensor array without a cavity. However, since the onset of nucleation of the tested liquid (FC-72) was associated with a significant surface temperature hysteresis, it was possible to set the surface temperature equal to that of the tests No. 1 to 7 without generating a bubble. Figure 6-29 compares the natural convection results with those of the tests No. 1 to 4. As can be seen in the figure, at low surface

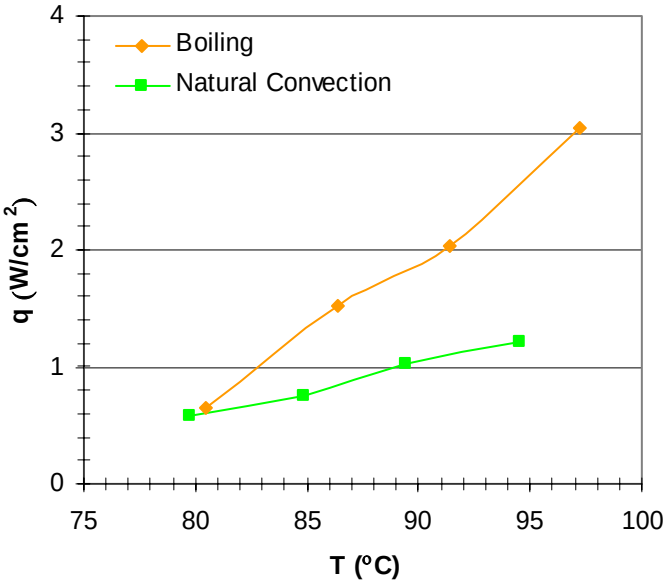

Figure 6-29: Comparison of heat flux outside the contact area with natural convection.

temperature, the convection heat flux outside the bubble is almost the same as the natural convection heat flux at the same surface temperature. However, the difference between the two significantly increases at the higher surface temperatures.

Figure 6-30 compares the results of tests at saturation conditions (tests No. 1 to 4)

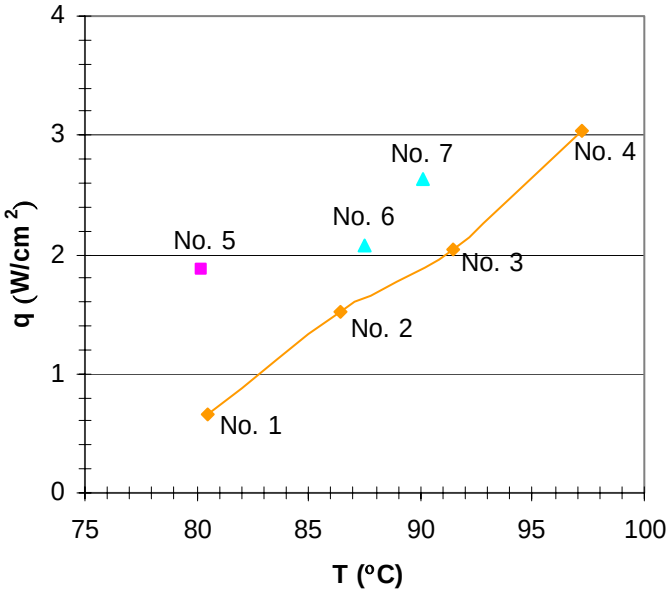

Figure 6-30: Comparison of heat flux outside the contact area at different test conditions.

with test conditions No. 5 to 7. As can be seen in the figure, heat flux in test No. 5 is significantly higher than test No. 1. Also, heat flux in subcooled conditions (tests No. 6 and 7) is higher than in saturation conditions (tests No. 2 and 3).

6-3-3-7- Total Heat Transfer from the Surface

As discussed in the previous sections, the three mechanisms of heat transfer from the surface including microlayer evaporation, transient conduction, and convection are active during the nucleation process and contribute significantly to the total heat transfer from the surface. The magnitude of these heat transfer mechanism (see Table 6-2) for saturation conditions are plotted in Figure 6-31. As can be seen in the figure, heat transfer through microlayer evaporation is always less than the other mechanisms of heat transfer. At low surface temperature, the transient conduction heat transfer mode has the highest magnitude among the three mechanisms of heat transfer, and as the surface temperature is increased, the convection mode exceeds the transient conduction mode. Figure 6-32 shows the relative contribution of these three mechanisms of heat transfer at different

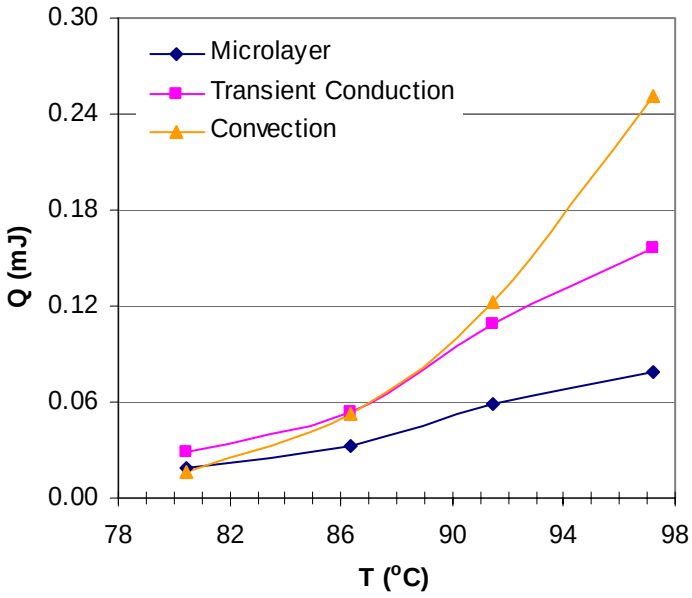

Figure 6-31: Heat transfer from the surface through different mechanisms over area $\pi D_b^2/4$.

surface temperatures. As can be seen in the figure, the relative contribution of the microlayer evaporation and the transient conduction modes decreases with increasing the

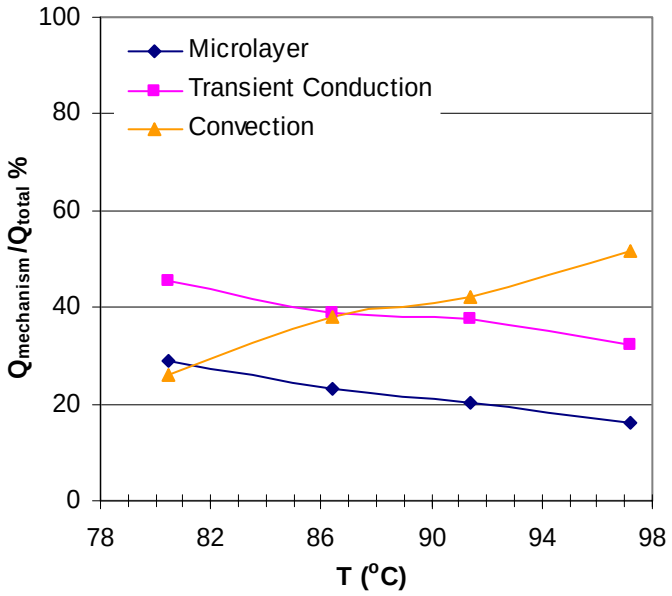

Figure 6-32: Contribution of different mechanisms of heat transfer to the total surface heat transfer over area $\pi D_b^2/4$.

surface temperature, while the relative contribution of the convection heat transfer mode increases with the surface temperature. A comparison of these results with the existing literature is provided in chapter 7.

CHAPTER 7: COMPARISON WITH EXISTING LITERATURE

In this chapter, the experimental results on details of the nucleation sub-processes are analyzed and compared with the traditional models in the boiling literature and recent microscale experimental studies. The following subjects are covered.

- Bubbling dynamics
    - Bubble growth
    - Bubble departure diameter
    - Relation between departure diameter and frequency
- Mechanisms of heat transfer from the surface
    - Microlayer evaporation
    - Transient conduction
    - Microconvection
- Recent microscale experimental studies

7-1- Bubble Dynamics

7-1-1- Bubble Growth

In this section, the experimental results for bubble growth are compared with predictions of four available models for heterogeneous bubble growth. These models represent the more popular of the competing theories. The models and their fundamental assumptions have been discussed in chapter 2.

7-1-1-1- Mikic and Rohsenow Model (1969)

Assuming that the bubble acquires its entire growth energy from the relaxation layer (i.e. superheated liquid surrounding the bubble dome), Mikic and Rohsenow (1969) determined the following bubble growth correlation (Equation 2-24).

$$R = \left(\frac{12}{\pi}\right)^{1/2} \left\{1 - \frac{T_w - T_\infty}{T_w - T_{sat}} \left[\left(1 + \frac{t_w}{t}\right)^{1/2} - \left(\frac{t_w}{t}\right)^{1/2}\right]\right\} Ja\sqrt{\alpha t}$$

As mentioned in the previous chapter, the bubble waiting time in all of the test results, except in test No. 5, was about zero. This model suggests that for $T_\infty = T_{sat}$ and $t_w = 0$, the bubble radius is zero (i.e. $R = 0$). In fact, this is consistent with the assumptions under which this model has been developed. Mikic and Rohsenow (1969) assumed that during the first stage of the bubble growth process heat transfers to the liquid adjacent to the wall through transient conduction. The thermal energy transferred to the liquid via conduction is subsequently passed to the bubble when the bubble emerges from the cavity and grows over the surface. Basically, the Mikic and Rohsenow (1969) model implies that with a zero waiting time, no heat exists in the liquid to be consumed by a growing bubble. Therefore, only test result No. 5 with a waiting time of 3.16 ms was compared with the Mikic and Rohsenow (1969) model. Figure 7-1 shows

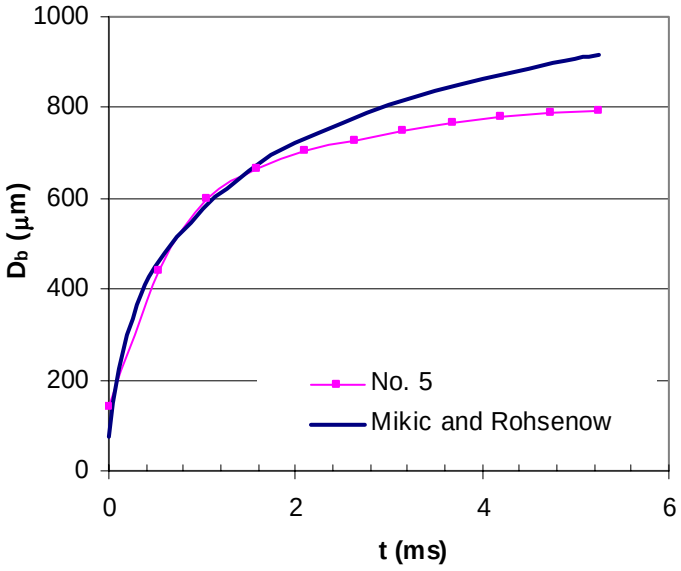

Figure 7-1: Comparison of the Mikic and Rohsenow (1969) model with test results No. 5 (with waiting time).

this comparison.

As can be seen in the figure, the model predicts a growth fairly close to the experimental results. In fact, the agreement between the two at the beginning of the growth period is excellent and only after about 1.5 ms does the model start to overpredict the bubble diameter. Eventually, the model overpredicts the bubble diameter by 15% at the time of departure. This is equivalent to an overprediction of 52% in bubble volume and the total amount of energy transferred to the bubble. Considering that the microlayer evaporation contributed into the experimental bubble growth, the Mikic and Rohsenow (1969) model also overpredicted the actual contribution of the relaxation layer heat transfer to the bubble at the early growth stage, and the microlayer coincidently compensated in part for the difference. Review of the microlayer evaporation data shows that approximately 74% of the microlayer evaporates into the bubble during the first 1.5 ms of the growth period. This is approximately 13% of the bubble energy (i.e. bubble volume).

7-1-1-2- Van Stralen et al. model (1975)

Van Stralen et al. (1975) multiplied the homogeneous growth correlation of Plesset and Zwick (1954) by correction factor b and presented the following correlation (Equation 2-25). The parameter b is proportional to the relative height of the bubble dome that is not covered with the superheated liquid.

$$R(t) \cong \left(\frac{12}{\pi}\right)^{1/2} bJa(\alpha t)^{1/2} = 1.95 bJa(\alpha t)^{1/2}$$

$$Ja = \frac{\rho_l c_l (T_w - T_{sat})}{\rho_v h_{fg}} \exp - \left(\frac{t}{t_g}\right)^{1/2}$$

Results of comparison between the Van Stralen et al. (1975) model and the experimental are presented in Figures 7-2 to 7-4. Parameter b was set at 0.8 for all experimental conditions. Figure 7-2 compares the model with experimental results at saturation conditions. Only the lowest and highest surface temperature cases (No. 1. and 4) are presented in the graph, since the two other conditions (No. 2 and 3) show a similar trend. As can be seen in the figure, the Van Stralen et al. (1975) model doesn't properly predict the bubble growth rate at any stage of the process. At low surface temperature (test No. 1), it overpredicts the bubble diameter at the beginning of the growth. The growth rate suddenly slows down after a rapid expansion at the beginning of the process. Although this slow down eventually compensates for the fast initial growth, allowing the model to closely predict the final bubble diameter, the model doesn't seem to follow the physics of the bubble growth at the different growth stages. As mentioned in chapter 2, Van Stralen et al. (1975) multiplied the correlation Plesset and Zwick (1954) for

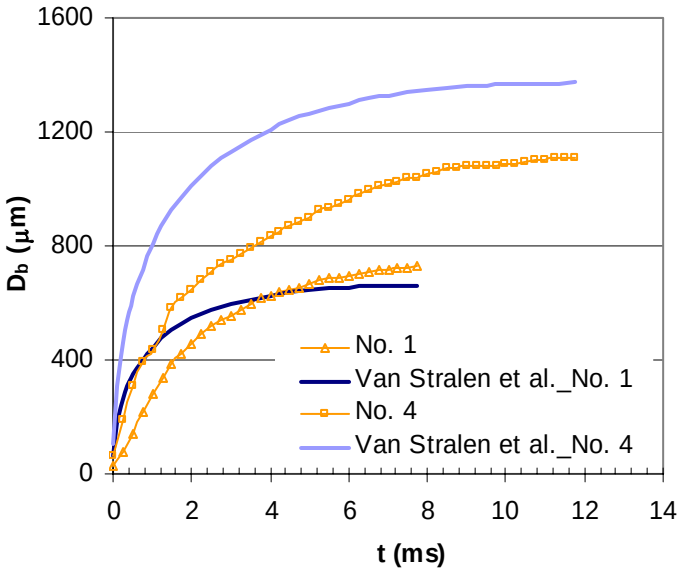

Figure 7-2: Comparison of the test results at saturation conditions (No. 1 and 4) with Van Stralen et al. (1975) model.

homogenous bubble growth ($R(t) = 1.95 Ja(\alpha_l t)^{1/2}$) by parameter b to account for their assumption that part of the bubble is not covered by the superheated liquid. As will be shown in section 7-1-4, a coefficient 1.95 causes a very significant overprediction for the bubble growth rate. If Van Stralen et al. (1975) had used the conventional definition of the Ja number (i.e. time independent Ja) in their model, the model would have predicted a bubble diameter that is 3.2 times greater than the experimental value. This is equivalent to 31.3 times greater bubble volume (i.e. energy transfer to the bubble). The effect of this correction at small times is low, so the model predicts a significant growth rate at the early growth stage, and the growth rate quickly reduces as the correction factor becomes significant. Essentially, Van Stralen et al. (1975) damped the effect of using 1.95 by introducing Ja number that reduces with time. For instance, for the test result No. 4 the Ja number decreases from 62 to 23.7 during the bubble growth period.

Figure 7-3 compares the Van Stralen et al. (1975) model with test results at

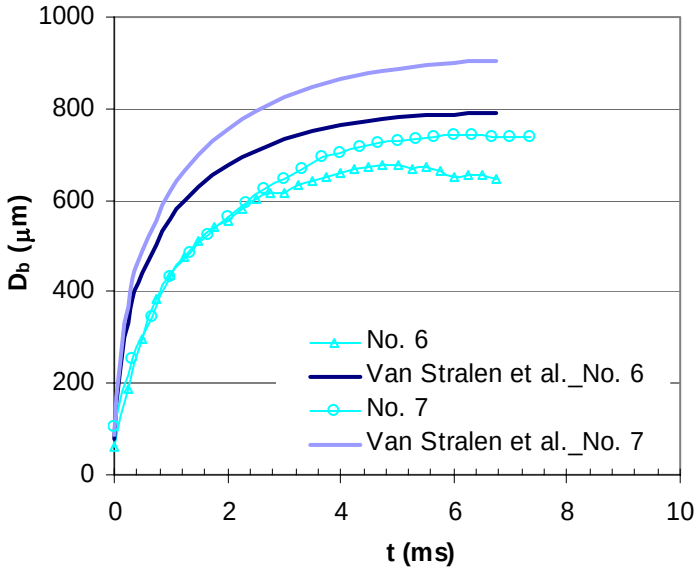

Figure 7-3: Comparison of the test results at subcooled conditions (No. 6 and 7) with Van Stralen et al. (1975) model.

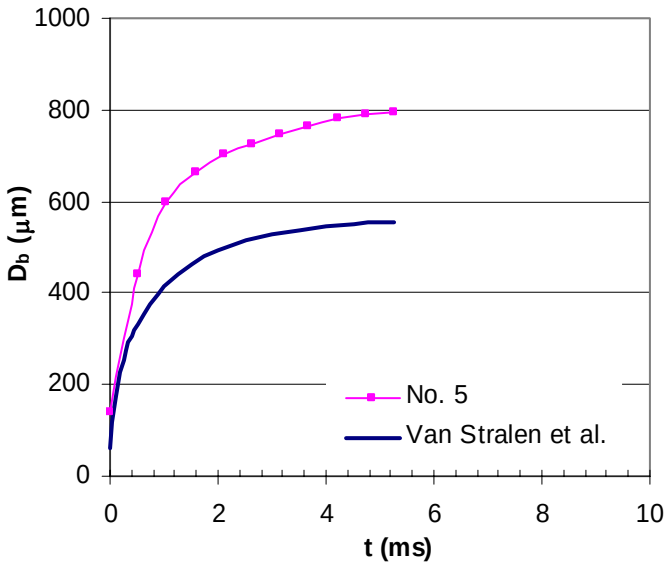

Figure 7-4: Comparison of the test result No. 5 (with waiting time) with Van Stralen et al. (1975) model.

subcooled conditions (test No. 6 and 7). As can be seen in the figure, the model predicts the bubble growth significantly higher than the test results at the beginning of the growth, similar to the saturation conditions (see Figure 7-2). The model predictions get closer to the experimental results in the later growth stage, but that might be just a coincidence, since the model doesn't have any mechanism to take into account the subcooling effect (i.e. subcooling temperature is not incorporated into the model).

As can be seen in Figure 7-4, even in the case of test No. 5 with a relatively rapid bubble growth rate at the beginning and a quick slow down afterward, the Van Stralen et al. (1975) model still fails to follow the experimental growth rate.

Overall, comparison of the Van Stralen et al. (1975) model with the experimental data suggests that the model doesn't use the right physics for the bubble growth at different stages of the growth process for different liquid and surface conditions.

7-1-1-3- Cooper Model (1969)

As mentioned in chapter 2, Cooper's (1969) model has been developed assuming that the microlayer is the dominant contributor to the bubble growth. However, the experimental results of this study suggested that the microlayer has a limited contribution (10-22% for the test conditions of this study) to the bubble growth. Although the fundamental assumption of this model is not supported by the experimental results, the two will still be compared to show the difference between the growth rates observed in the experiment and those of the bubbles supplied solely by microlayer energy.

Cooper (1969) provided the following two correlations for bubble growth (Equations 2-28 and 2-29).

- Highly conducting wall,

$$R(t) = 1.98\,\mathrm{Pr}_l^{-1/2}\, Ja(\alpha_l t)^{1/2}$$

- Poorly conducting wall,

$$R(t) = 1.12\left\{\frac{k_s\rho_s C_s}{k_l\rho_l C_l}\right\}^{1/2} Ja(\alpha_l t)^{1/2}$$

Since a specific criterion for application of these two correlations has not been provided by Cooper (1969), it is important to briefly study these two correlations from different perspectives. Using the FC-72 and BCB properties, the terms $1.98\,\mathrm{Pr}_l^{-1/2}$ and $1.12\left(k_s\rho_s C_s / k_l\rho_l C_l\right)^{1/2}$ were determined to be 0.64 and 2.06, respectively. This clearly shows that the Cooper's correlation for poorly conducting walls predicts a significantly higher growth rate than a highly conducting wall, as shown in Figure 7-5. This seems physically incorrect, since the microlayer evaporation rate is expected to be higher when there is less resistance to drawing heat from the surface, as in the case of a highly

conducting wall. As mentioned in chapter 2, Mei et al. (1995) showed that the wall and microlayer thermal interaction is very complicated. They showed that the microlayer evaporation rate and bubble growth is a function of factors: $Ja = \rho_l C_l (T_w - T_{sat}) / \rho_v h_{fg}$, $Fo = \alpha_w t_d / H^2$, $k = k_l / k_w$, and $\alpha = \alpha_l / \alpha_w$.

Although Cooper's correlation for a highly conducting wall is the only one left for comparison with the experimental results, it is still unclear whether this equation is applicable for the BCB/silicon composite wall of the 2nd generation sensor. Thus, the main question is whether or not the BCB layer on the silicon wall has appreciably slowed down the microlayer evaporation rate. The main basis for development of Cooper's model for a poorly conducting wall was that the wall's rapid temperature drop to T_{sat} significantly slows down the microlayer evaporation rate. For instance, consider a microlayer of liquid with a saturation temperature of 60 °C on a surface initially at 90 °C. This represents a temperature potential of 30 °C available to evaporate the microlayer. A

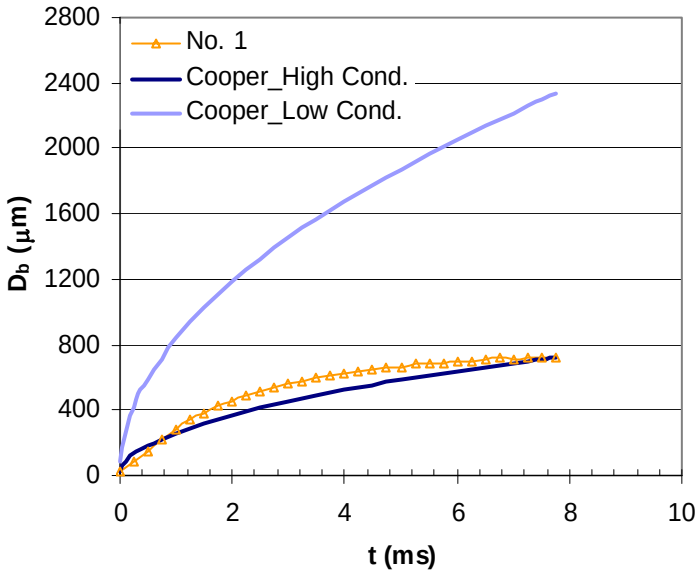

Figure 7-5: Comparison of the Cooper's (1969) model for highly and poorly conducting walls and test results No. 1 (in saturated liquid).

sudden decrease of the surface temperature to only a few degrees above the saturation temperature, reduces the microlayer evaporation rate multiple times. In this experiment, the evaporation time of the microlayer at any location on the surface is in the order of 1 ms, which is significantly shorter than the bubble growth time. In a test case with an initial surface temperature of 90 °C, a fall of 10 °C in the surface temperature during the microlayer evaporation represents an only 15% ($=\left(1-\frac{(90+80)/2-56.6}{90-56.6}\right)\times 100$) drop in the available temperature potential for microlayer evaporation. In addition, the experimental results showed that the microlayer contained 30-50% (depending on the surface temperature) of its total microlayer evaporation energy due to sensible heating even before the microlayer was formed. Therefore, the microlayer evaporation rate is not expected to have slowed down more than 10%. Thus, the assumption of a highly conducting wall seems to be appropriate for this case.

Figures 7-6 to 7-8 show the comparison between the Cooper (1969) model and the experimental results. As can be seen in Figure 7-6, the Cooper (1969) model can only predict the bubble growth reasonably well at the early growth stage, when the microlayer plays a greater role in the bubble growth than in the later stages of the growth process. Figure 7-6 shows that at low surface temperature (test No. 1), the Cooper (1969) model follows the experimental data for a short period of time (about 1 ms) until the bubble reaches a diameter of about 200-300 μm. Perhaps this is due to the fact that microlayer has a greater contribution to the bubble growth at the early growth stage. At higher surface temperature (test No. 4), the Cooper (1969) model follows the test result for a longer period of time (about 2 ms) until the bubble reaches a diameter of about 500-700

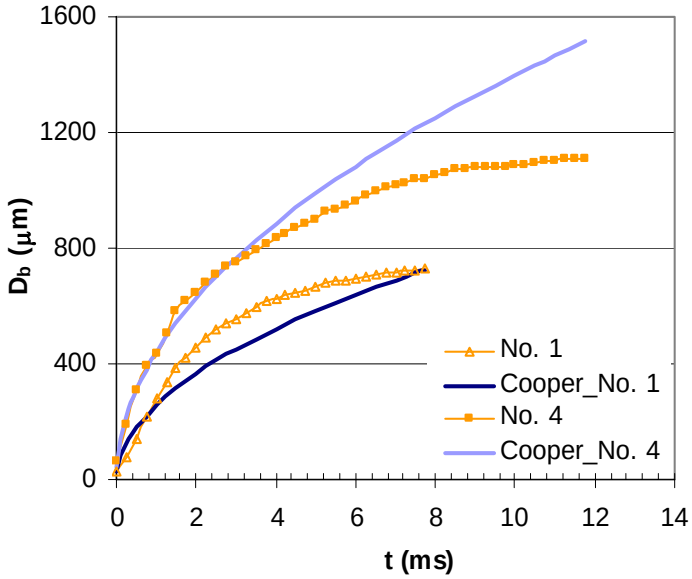

Figure 7-6: Comparison of the Cooper model with test results at saturation conditions (No. 1 and 4).

μm. This can also be due to the fact that the microlayer contribution into the bubble growth has increased with the surface temperature, according to the experimental results.

Figure 7-7 compares the Cooper (1969) model with experimental data at subcooled conditions. In this case also, the Cooper (1969) model closely follows the experimental results at the early growth stage. However, the model fails to follow the test result shortly after the beginning of the growth. This comparison highlights that the Cooper (1969) model does not have a built-in mechanism to take care of the reduction in bubble diameter due to condensation at the bubble dome at subcooled conditions. As can be seen in the results, Cooper (1969) model predicts a continuous bubble growth while test result shows a reduction in bubble diameter.

Figure 7-8 shows the comparison of the Cooper (1969) model with test result No. 5. As can be seen in the figure, the Cooper (1969) model fails to predict the test results over the entire growth period. The test result shows an explosive growth at the beginning

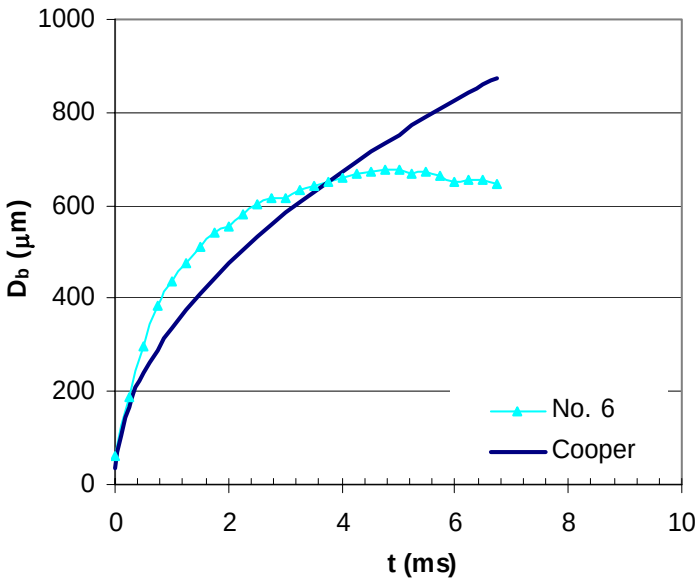

Figure 7-7: Comparison of the Cooper (1969) model with test results at subcooled condition (No. 6).

of the bubble formation, followed by a relatively slow growth rate, whereas the Cooper (1969) model predicting a gradual growth rate typical of this model, as can also be seen in Figures 7-6 and 7-7.

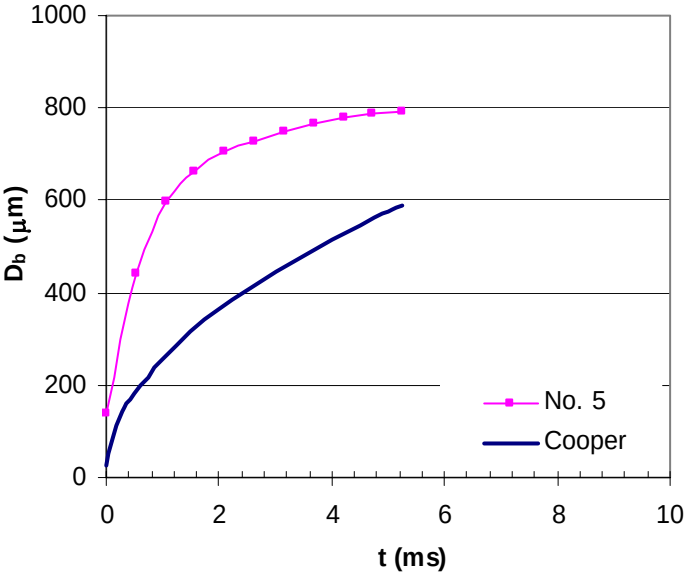

Figure 7-8: Comparison of Cooper (1969) model with test result No. 5 (with waiting time).

Overall, although the Cooper (1969) model was not successful in predicting the bubble growth during the most of the growth period, it showed some agreement with the test results (expect for test No. 5) at the beginning of the growth process. Note that Van Stralen et al. (1975) model was not successful in predicting the growth rate at the early growth stages (see Figures 7-2 and 7-3).

7-1-1-4- Van Ouwerkerk (1971)

Van Ouwerkerk (1971) combined the effect of heat transfer from the thermal boundary layer (i.e. relaxation layer) and microlayer, determining the following correlation (Equation 2-30) for bubble growth:

$$R(t) = 2.44\,Ja(\alpha t)^{1/2}$$

He assumed that the thermal boundary around the bubble dome (i.e. relaxation layer) is uniformly superheated. Details of this model are discussed in chapter 2. Comparison of this model with both homogenous and heterogeneous growth models (see

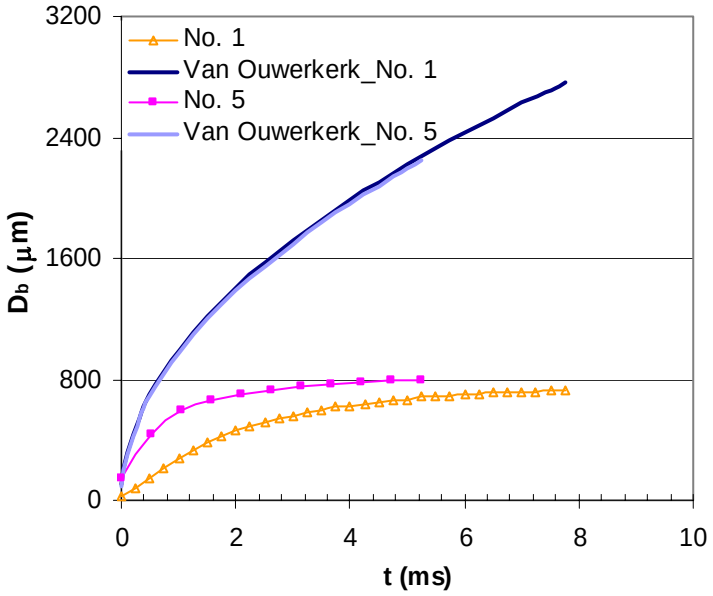

Figure 7-9: Comparison between test results No.1 and No. 5 with Van Ouwerlerk (1971) model.

Table 7-1) shows that constant factor 2.44 is higher than in all other models. For this reason, this model significantly overpredicts the experimental results, as can be seen in Figure 7-9. Perhaps this is because the model assumes that the liquid surrounding the bubble is uniformly superheated and also predicts a microlayer thickness that is almost the same as the Cooper (1969) model prediction.

Table 7-1: Comparison of χ coefficients in both homogeneous and heterogeneous growth models ($R(t) = \chi Ja(\alpha_l t)^{1/2}$)

Model	**Constant Coefficient χ**
Bosnjakovic (1930)	1.128
Forster and Zuber (1954)	1.77
Plesset and Zwick (1954)	1.95
Cooper (1969)	0.64
Van Ouwerkerk (1971)	2.44

7-1-2- Bubble Departure Diameter

Numerous models have been proposed for prediction of the bubble detachment diameter in pool boiling. Carey (1992) conducted a survey of the existing models. The presented models cover the effect of a wide range of parameters such as liquid properties, surface superheat temperature, heat flux, and liquid pressure. Also, some of the models used different constants provided mainly for traditional fluids (not for FC-72). Considering the range of parameters varied in the experiment and unavailability of some of the constants used in the correlations, a set of correlations were selected for comparison with the experimental data, as can be seen in Table 7-2. Figure 7-10 shows a comparison of the listed models with the experimental results.

Table 7-2: Departure diameter correlations.

Zuber (1964)	$Bo^{1/2} = \left[\frac{3\pi^2 \rho_l \alpha_l g^{1/2}(\rho_l - \rho_v)^{1/2}}{\sigma^{3/2}}\right]^{1/3} Ja^{4/3}$
Cole (1967)	$Bo^{1/2} = 0.04 Ja$
Kutateladze and Gogonin (1979)	$Bo^{1/2} = 0.25\left(1 + 10^5 K_1\right)^{1/2}$ for $K_1 \prec 0.06$ $K_1 = \left(\frac{Ja}{\mathrm{Pr}_l}\right)\left\{\left[\frac{g\rho_l(\rho_l - \rho_v)}{\mu_l^2}\right]\left[\frac{\sigma}{g(\rho_l - \rho_v)}\right]^{3/2}\right\}^{-1}$
Jenson and Memmel (1986)	$Bo^{1/2} = 0.19\left(1.8 + 10^5 K_1\right)^{2/3}$ $K_1 = \left(\frac{Ja}{\mathrm{Pr}_l}\right)\left\{\left[\frac{g\rho_l(\rho_l - \rho_v)}{\mu_l^2}\right]\left[\frac{\sigma}{g(\rho_l - \rho_v)}\right]^{3/2}\right\}^{-1}$

As can be seen in the figure, both the Zuber (1964) and Cole (1967) models overpredict the experimental data, but the Zuber (1964) model prediction is significantly higher than the Cole (1967) model. An examination of the Zuber (1964) model suggests that the fundamental reason for this behavior is the exponent 4/3 for Ja in the model. The coefficient $Ja^{4/3}$ in the Zuber (1964) model (0.019 for FC-72) is about half of coefficient Ja in Cole (1967) model (0.04). Using the exponent of 4/3 in the Zuber (1964) model leads to a significant overprediction of the model both in terms of the magnitude and the slope of its change with surface temperature. Kutateladze and Gogonin (1979) and Jenson and Memmel (1986) models suggest that the bubble departure diameter is a weaker function of Ja. This has led to a better agreement of their models with the experimental results, especially in the case of the Jenson and Memmel

(1986) model for which the variation trend with temperature closely follows the experimental results.

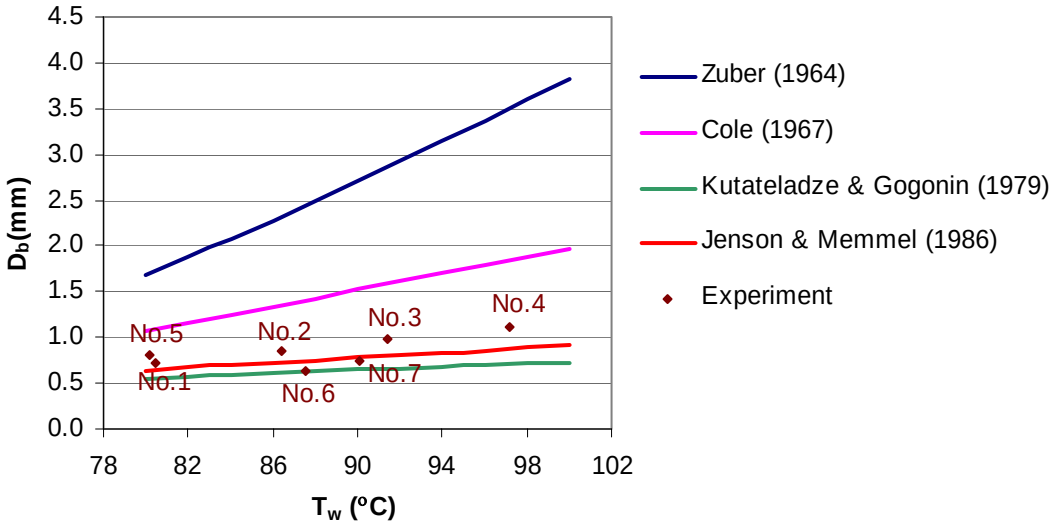

Figure 7-10: Comparison between experimental results and models for bubble departure diameter.

7-1-3- Relation between Bubble Departure Diameter and Frequency

As we have learned from the experimental results (see Figure 7-19), although the bubble diameter (D_b) and frequency (f) significantly change at different test conditions, parameter $D_b f$ remains almost constant (changes between 0.090 and 0.096). Carey (1992) provided a survey of the existing correlations in the literature for relationships between the bubble departure diameter (D_b) and its departure frequency (f). Table 7-3 lists these correlations. As can be seen in the table, only the first three correlations predict that parameter $D_b f$ is constant. Jacob and Fritz (1931) prediction of this constant value is close to the experimental result of this study even though their correlation has been developed for water and hydrogen. Expression $1.18\left(\frac{t_g}{t_g + t_w}\right)$ in Peebles and Graber

(1953) correlation was determined to be 0.65 for test No. 5 and 1.0 for the rest of the test conditions. This correlation gives a value of 0.054 for test condition No. 5 and 0.084 for the other test conditions. Therefore, the Zuber (1963) model, which has a similar functional form, also under predicts the value of $D_b f$ parameter. This comparison suggests that the experimental results can be predicted fairly closely using $fD_b = 1.11\left[\frac{\sigma g(\rho_l - \rho_v)}{\rho_l^{\,2}}\right]^{1/4}$.

Table 7-3: Relation between bubble departure diameter and frequency

Jacob and Fritz (1931)	$fD_b = 0.078$ (for water and hydrogen)
Peebles and Garber (1953)	$fD_b = 1.18\left(\frac{t_g}{t_g + t_w}\right)\left[\frac{\sigma g(\rho_l - \rho_v)}{\rho_l^{\,2}}\right]^{1/4}$
Zuber (1963)	$fD_b = 0.59\left[\frac{\sigma g(\rho_l - \rho_v)}{\rho_l^{\,2}}\right]^{1/4}$
Ivey (1967)	$f^2 D_b = cons\tan t$ for inertia controlled growth $f^{1/2} D_b = cons\tan t$ for heat transfer-controlled regime
Mikic and Rohsenow (1969)	$f^{1/2} D_b = \left(\frac{4}{\pi}\right) Ja\sqrt{3\pi\alpha_l}\left[\left(\frac{t_g}{t_w + t_g}\right)^{1/2} + \left(1 + \frac{t_g}{t_w + t_g}\right)^{1/2} - 1\right]$

7-2- Mechanisms of Heat Transfer from the Surface

As mentioned in chapter 2, over the past 50 years, several models for predicting the surface heat transfer during the boiling process have been developed. These models have been commonly used to predict the surface heat transfer on large boiling surfaces which simultaneously generate numerous bubbles. Experimental coefficients were often

used to accommodate for difference between the models and the experimental results. Unlike the test conditions of this study, on a large boiling surface, interactions between the bubbles would likely trigger a more complex regime of heat transfer than in the case of a single bubble boiling. Although the models were often applied to such regimes, they do not have built-in mechanisms to model the heat transfer processes resulted from interactions between the bubbles. In contrast, these models have been developed solely based on assumptions concerning the heat transfer processes involved in single bubble boiling. The utility of the current work, therefore, is in testing the fundamental mechanistic assumptions upon which the models are based, while ignoring higher order effects due to multiple bubbles interactions. The premise of such an assumption is that if the lowest order physics and dominant mechanistic trends are not captured, the utility of the model in other regimes is likely to be similarly limited.

These models are all explicitly or implicitly a function of wall superheat, bubble diameter, bubble departure frequency, and nucleation site density. For instance, the nucleation site density explicitly appears in the final form of the correlation developed by Tien (1962), whereas in the Rohsenow's correlation (1951), the effect of the surface in combination with a particular liquid indirectly accounts for the nucleation sites as an empirically derived constant. The Mikic and Rohsenow (1969) and Forster and Greif (1959) correlations explicitly use the bubble frequency and departure diameter. Given the detailed nucleation parameters (including wall superheat, bubble diameter, bubble departure frequency, and nucleation site density on the surface), one can calculate the heat transfer coefficient directly using any of the developed correlations. This assumes that the model properly represents the physics of the heat transfer process. As shown in

Figure 6-31, the experimental results of this study suggested that all mechanisms of heat transfer have a significant contribution in heat transfer from the surface. Therefore, none of the models alone introduced in chapter 2 are representative of the complete physics of heat transfer from the surface, since they only assume one mechanism of heat transfer to be dominant. In order to explore whether these models can predict the components of surface heat transfer for which they have been developed, a detailed study is conducted in the following.

7-2-1- Calculation of the Experimental Nu Number

Using the experimental results for bubble departure diameter and surface heat flux, the *Nu* number was calculated using the following equation.

$$Nu = \frac{hD_b}{k} = \frac{q''D_b}{(\Delta T)k_l} \tag{7-1}$$

The average heat flux (q'') values are provided in Table 6-2. Figure 7-11 shows the determined Nu number. As can be seen in the figure, Nu number increases with the surface temperature. Also, the limited data available for subcooled condition suggest that subcooling decreases the Nu number. The results are compared with the boiling models in the following sections.

7-2-2- Rohsenow Model (1951)

As mentioned in the introduction section, Rohsenow's model (1951) suggests that convective heat transfer to the liquid is the dominant mode of heat transfer during the boiling process, and the role of the bubbles is to simply induce strong convective motions within the liquid. Rohsenow (1951) suggested the following equation for boiling heat transfer from the surface (note that the exponent of 1.7 for *Pr* is applicable for any liquid except water):

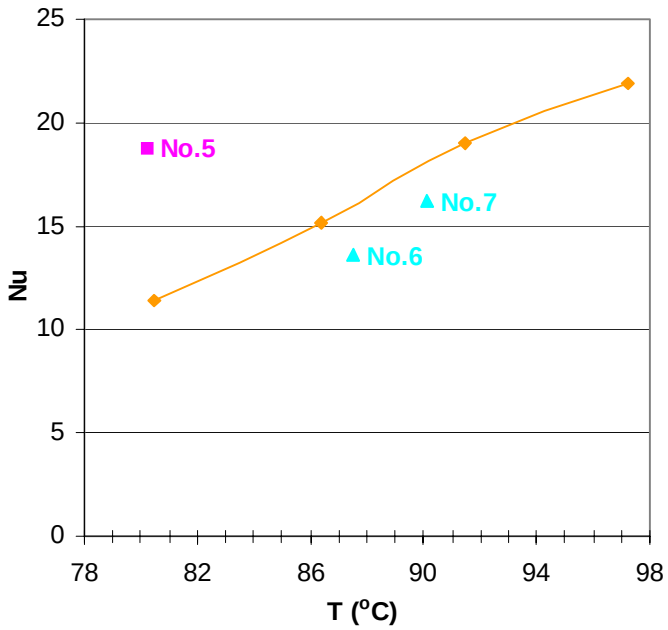

Figure 7-11: Nu number at different surface and liquid temperatures.

$$\frac{C_l(\Delta T)}{h_{lv}} = C_{sf}\left(\frac{q''}{\mu_l h_{lv}}\sqrt{\frac{\sigma}{g(\rho_l-\rho_v)}}\right)^{0.33}\mathrm{Pr}^{1.7} \tag{7-2}$$

The value of C_{sf} depends on the combination of the surface and liquid properties that should be determined experimentally. For different combinations of liquid and surface material, Rohsenow (1951) found C_{sf} to vary over a range of 0.0049-0.0154. A value of 0.013 was recommended for C_{sf} as a first approximation when no experimental data is available.

In a effort to determine an equation in the form

$$Nu = C_1\,\mathrm{Re}^{m_1}\,\mathrm{Pr}^{n_1} \tag{7-3}$$

with C_1 independent of the surface and liquid combination properties, we reverted to the original elements used in derivation of Equation 7-2. Rohsenow (1951) used the following equations for the bubble diameter and *Re* number

$$D_b = C_d\beta\left[\frac{2\sigma}{g(\rho_l-\rho_v)}\right]^{0.5} \tag{7-4}$$

$$\mathrm{Re}_b = \frac{\rho_v V_b D_b}{\mu_l} \tag{7-5}$$

$$V_b = \frac{q''}{\rho_v h_{lv}} \tag{7-6}$$

where $C_d\beta$ is a function of liquid and surface properties and G_b was related to the surface heat flux through the following equation.

$$q'' = C_q h_{lv} G_b = C_q h_{lv} \left(\rho_v \frac{\pi}{6} {D_b}^3 fn \right) \tag{7-7}$$

Using Equations 7-4 to 7-7 and Equation 7-1 for the *Nu* number, Equation 7-2 can be written as follow

$$Nu = \frac{C_q}{C_{sf} \left(\frac{C_q}{\sqrt{2} C_d \beta} \right)^{0.33}} \mathrm{Re}_b^{\,0.67} \, \mathrm{Pr}^{-0.7} \tag{7-8}$$

Using the experimental data for bubble diameter and liquid properties, the coefficient $C_d\beta$ that represents the liquid and surface combination properties was determined. Since the area of interest for heat transfer calculation is D_b, the following equation for *n* and the experimental values of bubble diameter and frequency were used to determine C_q from Equation 7-7.

$$n = \frac{1}{{D_b}^2} \tag{7-9}$$

Note that the values of factors $C_d\beta$ and C_q change at different test conditions. Eventually, using a value of 0.013 for C_{sf} and Equation 7-5 for Re_b, Nu was determined using Equation 7-8. Results are presented in Figure 7-12.

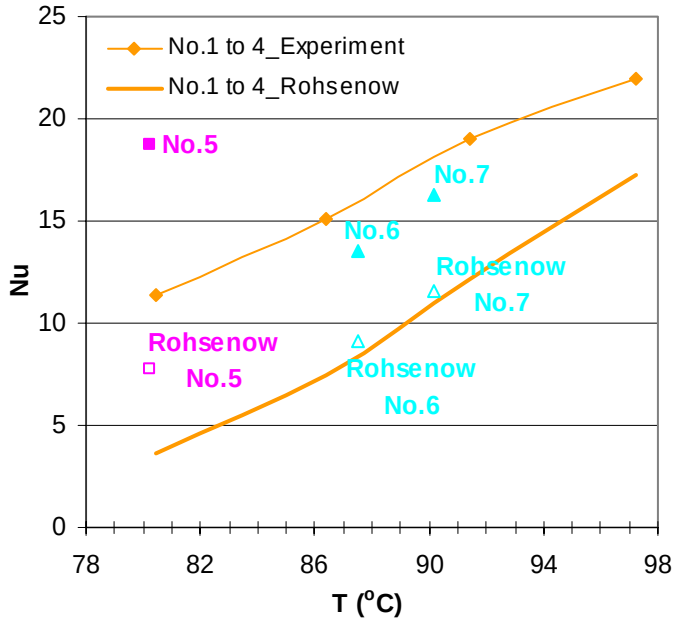

Figure 7-12: Comparison of Nu number between experiment and Rohsenow (1951) model.

Comparison of the experimental results for saturation conditions with Rohsenow (1951) model shows that the model significantly underpredicts the Nu number. The model prediction is 34.9% of the experimental value at low surface temperature (test No. 1) and 78.6% of the experimental value at higher surface temperature (test No. 4). As mentioned earlier, Rhosenow (1951) model does not represent the physics of the heat transfer process, so its disagreement with the test results is not surprising. However, the predictions of the model seem to be close to the microconvection fraction of the surface heat transfer results observed in the experiment. As discussed in chapter 6, miroconvection heat transfer occurs outside the contact area. Using the heat flux values (listed in Table 6-2) at this region, Nu number was calculated and compared with the model. Figure 7-13 shows the results. As can be seen in the figure, the model is in very close agreement with the experimental results. Although the agreement between the two is remarkable, further tests, particularly on other liquids, are required before one can

conclude that Rohsenow (1951) model is generally adequate for modeling the microconvection heat transfer term.

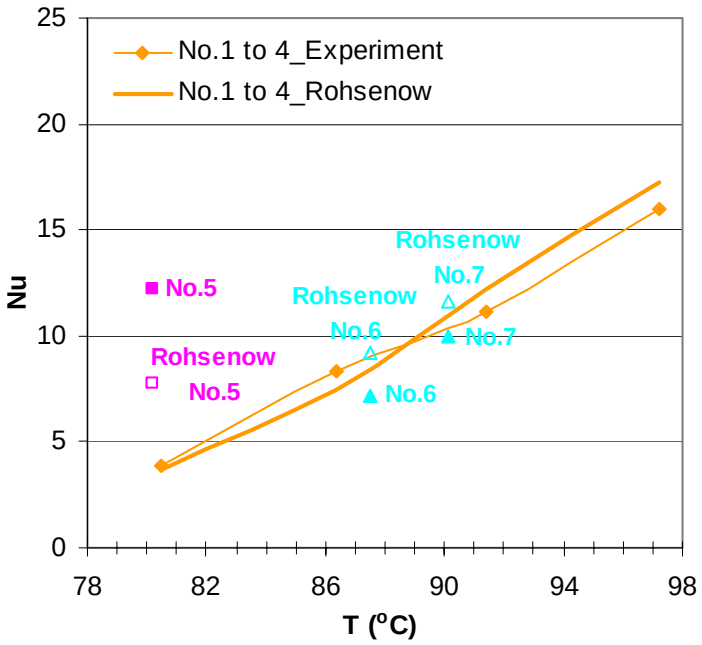

Figure 7-13: Comparison of experimental Nu number outside the contact area with Rohsenow (1951) model.

7-2-3- Forster and Zuber Model (1955)

Forster and Zuber (1955) used Rohsenow's model (1951) as the mechanism of heat transfer from the surface, but modified the expression for the bubble radius and velocity ($R = Ja(\pi\alpha_l t)^{1/2}$ and $V = \dot{R}$). They recommended the following equation for the *Nu* number.

$$Nu = 0.0015\,\mathrm{Re}_b^{\,0.62}\,\mathrm{Pr}^{0.33} \tag{7-10}$$

The Re_b was defined as follows

$$\mathrm{Re}_b = \frac{\rho_l}{\mu}\left(\frac{(\Delta T)C_l\rho_l\sqrt{\pi\alpha}}{h_{lv}\rho_v}\right)^2 \tag{7-11}$$

Using Equation 7-10, the Nusselt number was determined. Their correlation gives a maximum Nu of 0.56 at the highest surface temperature (at test case No. 4). This result is significantly different than the experimentally determined *Nu* number. In order to explore the source of such a significant deficiency in the model, it was compared with the Rohsenow (1951) model. Note that both models are based on a similar analogy for heat transfer from the surface. Three major differences of Forster and Zuber (1955) and Rohsenow (1951) models are the difference between the exponent for the *Pr* number, the constant coefficients, and the value of Re_b. Among the three factors, the very small constant coefficient of the correlation (0.0015) causes an inordinately small prediction for the *Nu* value.

7-2-4- Mikic and Rohsenow Model (1969)

The Mikic and Rohsenow (1969) model suggests that a departing bubble continuously pumps away the hot liquid adjacent the surface. Heat is transferred into the liquid that replaces the displaced fluid via transient conduction, which is considered to be the sole mechanism of heat transfer from the surface. They used the governing equation for heat transfer to a semi-infinite body to derive the following equation for surface heat flux.

$$q'' = 2\frac{k\Delta T}{\sqrt{\pi\alpha}}\sqrt{f} \tag{7-12}$$

Using Equation 7-1 for the *Nu* number, Equation 7-12 can be written as:

$$Nu = \frac{2}{\sqrt{\pi}}\left(\frac{f.D_b{}^2}{\alpha}\right)^{0.5} \tag{7-13}$$

Using Equation 7-13 and the experimental values of bubble frequency and diameter, the values of *Nu* for different test cases were calculated and the results are

reported in Figure 7-14. As can be seen in the figure, the transient conduction model of Mikic and Rohsenow (1969) predicts a much higher *Nu* than the experimental results. As it was shown in chapter 6, although the magnitude of the transient conduction heat transfer is much higher than the average surface heat transfer, the active area of this heat transfer mode is limited to the contact area. In addition, transient conduction is active for a limited period of time during the bubble growth process. Therefore, the fundamental reason for the Mikic and Rohsenow (1969) model overprediction of the test results is that it overpredicts the influence area and time period of the transient conduction process.

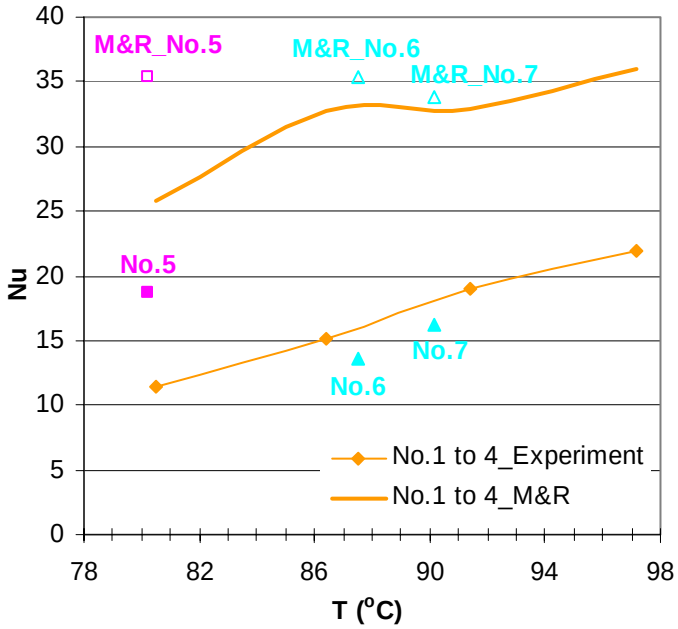

Figure 7-14: Comparison of Nu number between experiment and Mikic and Roshenow model (1969).

7-2-5- Tien Model (1962)

Tien (1962) suggested that the wake generated behind a bubble possesses the same velocity distribution as a stagnation point flow, except flowing in the opposite direction. He then used the heat transfer correlation for an inverted stagnation flow (Schlichting, 1960) and suggested the following equation for the rate of heat transfer.

$$q'' = 61.3\,\mathrm{Pr}^{0.33}\, k.n^{0.5}\left(\Delta T\right) \tag{7-14}$$

After substituting Equation 7-9 for n and Equation 7-1 for *Nu*, the following equation for *Nu* is determined.

$$Nu = 61.3\,\mathrm{Pr}^{0.33} \tag{7-15}$$

This equation determines a constant *Nu* = 189.5, which is one order of magnitude greater than the experimentally determined values. This model does not seem to represent the physics of the phenomena.

7-2-6- Forster and Greif Model (1959)

Forster and Greif (1959) assumed that each bubble released from the surface pumps a volume of liquid equal to its volume into the bulk liquid. They assumed that the temperature of the pumped liquid is equal to the average of the surface and bulk liquid. The Forster and Greif analogy (1959) resulted in the following expression for the heat transfer from the surface.

$$q'' = (\rho.C)_l.\left(\frac{\pi D_b^3}{6}\right).f.n.\Delta T/2 \tag{7-16}$$

Using Equation 7-9 for *n* and Equation 7-1 for *Nu*, Equation 7-16 can be written as follow

$$Nu = \frac{\pi}{12}\frac{f.D_b^{\,2}}{\alpha} \tag{7-17}$$

The experimental values of bubble frequency and diameter were used in Equation 7-17 to determine the *Nu* number. The *Nu* number was determined (137 and 267 for test conditions No. 1 and 4, respectively) to be one order of magnitude greater than the experimental results. Although the Forster and Greif (1959) model does not represent the physics of the heat transfer process and also its results are quite different than those of the

tests, the only variable parameter fD_b^2 in the model seems to give a slope approximately equal to the slope of the curve for saturation conditions.

In summary, none of the discussed models could properly predict the surface heat transfer during the nucleation process, since their assumptions do not represent the physics of the phenomena. As can be seen in Table 6-2 and Figure 6-31, the three mechanisms of heat transfer (microlayer evaporation, transient conduction, and convection/micrconvection) significantly contribute in total heat transfer from the surface. A proper model should take into account all three mechanisms of heat transfer.

7-3- Recent Microscale Studies

7-3-1- Studies of Demiray and Kim (2002, 2004)

This section is dedicated to analysis of a set of recent studies conducted by Demiray and Kim (2002, 2004) and Myers et al. (2005), all from the same group. These studies are particularly relevant to the current work, as they are closest in terms of working fluid, wall superheat and spatial/temporal resolution. These studies were also among the first to provide a detailed perspective of the microscale processes in nucleate boiling, and as such, form the current benchmark in the literature against which the present work should be compared. These studies were enabled by development of a novel micro heater array consisting of 96 rectangular platinum resistance heater elements deposited on a quartz substrate. The size of each heater element is 100×100 μm^2, and the entire array covers a square area of 0.01 cm^2. The heaters were also used to measure the local surface temperature. The development of the micro heater array has greatly contributed in advancing the understanding of the microscale heat transfer events during

the nucleation process. A careful analysis of the experimental conditions, details of the assumptions, procedure for processing the experimental data, and analysis of the conclusions are discussed. As will be shown, this has allowed for the resolution of several discrepancies between the conclusions/interpretations of the prior work and illustrates how the current results extend our current understanding of the nucleate boiling process.

7-3-1-1- Demiray and Kim (2002)

Demiray and Kim (2002) do not report spatially resolved data on surface heat flux and a separate account of different modes of heat transfer from the surface. Therefore, a one-to-one comparison of the results of this study with those of the Demiray and Kim (2002) is not possible. However, the heat transfer spikes observed during the nucleation process in the study of Demiray and Kim (2002) were found to be comparable to the sum of the microlayer and transient conduction heat transfer measurements recorded in the current work during a bubbling event under test conditions close to that of their work. So, the significance of this comparison is in comparing the integral value of the heat transfer results between the two studies. Before conducting this comparison, it should be noted that Demiray and Kim (2002) provides test results only at one test condition (surface and liquid temperatures of 76 °C and 52 °C, respectively). Test results of the current study at a temperature (77 °C) showed intermittent and irregular bubbling events, as was reported by Demiray and Kim (2002). Since this level of surface temperature was generating irregular bubbling events, testing at such conditions was avoided in the current work. Details of the Demiray and Kim (2002) test, data processing procedure, and conclusions are discussed in the following.

Demiray and Kim (2002) configured their heater array with an electronic feedback circuit to keep the heaters at a constant temperature. This was accomplished by

varying the applied voltage (and thereby the electrical power) supplied to the heater. Since the temperature of the surface was always constant, no significant transient conduction occurred in the substrate. As mentioned earlier, the test was conducted using surface and liquid temperatures of 76 °C and 52 °C, respectively. The temperature of each heater was sampled with a frequency of 3704 Hz. An uncertainty of less than 1 °C was reported for the heater temperature.

Figure 7-15 shows the experimental results of the total rate of heat transfer from the surface versus time. As can be seen in the figure, 10 bubbles were generated during the first 1 second of the reported time period. The reported growth time for the bubbles is between 4 to 5 ms with an average waiting time of approximately 100 ms between the bubbles. As can be seen in Figure 7-15, the heat transfer spikes due to bubbling events were superposed on a slow time-varying heat flux from the surface. Demiray and Kim

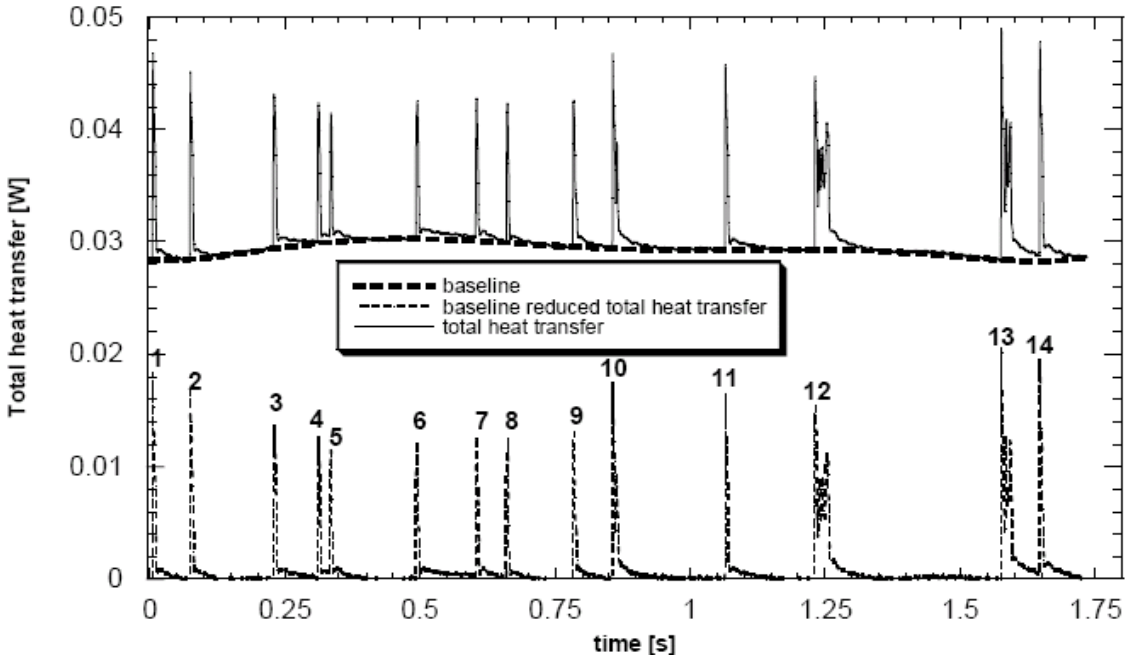

Figure 7-15: Total heat transfer vs. time (Demiray and Kim (2002)).

(2002) considered the slowly varying heat flux to be “likely due to a natural convection flow over the heater driven by the temperature difference between the bulk liquid and the heater array”. The heat transfer excursion around the slowly varying baseline was “assumed to be a consequence of bubble formation and departure”. “To obtain the effect of the bubble only, a sixth degree polynomial was fitted to selected points on the baseline and subtracted from the total time-resolved heat trace for each heater in the array”. The resulting heat flux data associated with the bubbling event, shown as a baseline reduced total heat transfer, is reported in Figure 7-15. Figure 7-16 shows the heat transfer excursion event associated with bubble #3, which was analyzed by Demiray and Kim (2002).

Demiray and Kim (2002) considered the area under the curve before the bubble departure to be due to microlayer evaporation and concluded that the microlayer

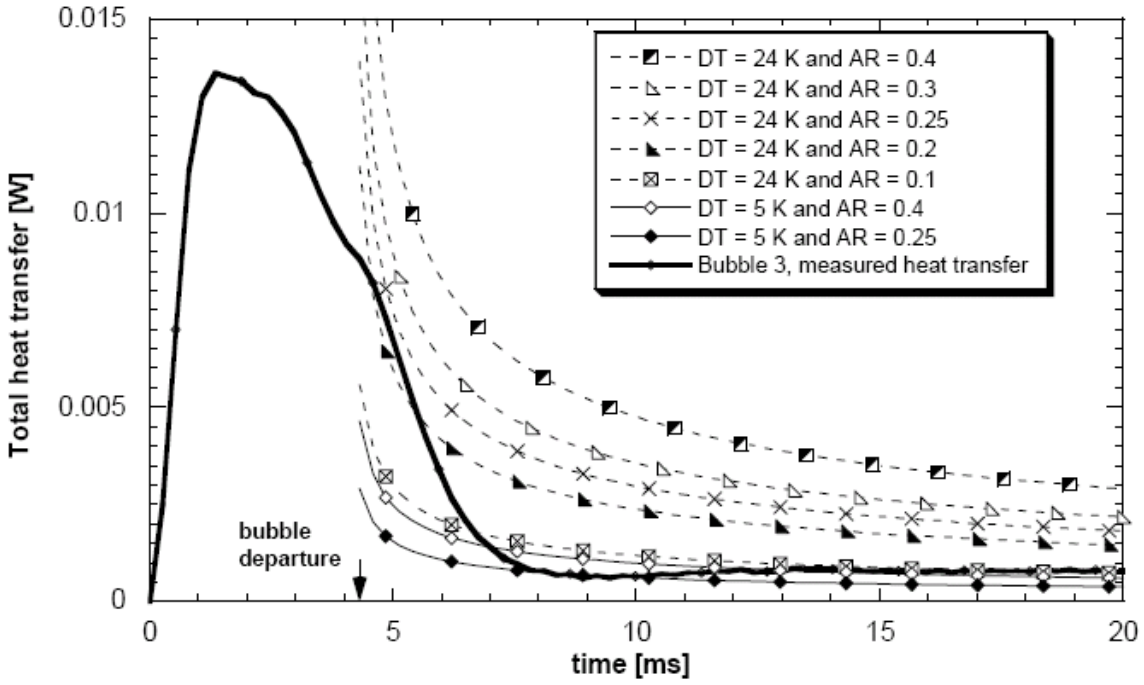

Figure 7-16: Wall heat transfer excursion for bubble 3 (Demiray and Kim (2002)).

evaporation contributes “a significant, but not dominant, fraction of the wall heat transfer.” Demiray and Kim (2002) also fit a two-parameter transient conduction model to the portion of the heat transfer curve that is after the bubble departure, where the parameters are given by ΔT and AR (AR is the ratio of the area influenced by transient conduction to a circular area with a diameter of the departing bubble). Demiray and Kim (2002) argued that their transient conduction results could be best matched by an AR=0.1 and a wall and liquid temperature difference of 24 °C. By comparing their results with an earlier study by Kim et al. (2000) that suggested an AR=0.4, they concluded that the temperature of the rewetting liquid is higher than that of the bulk, and suggested a temperature difference of 5 °C and AR=0.4.

Test case No. 5 of this study was considered for comparison with the Demiray and Kim (2002) result described above. As can be seen in Table 6-2, the surface and liquid temperatures in test case No. 5 are 80.2 °C and 56.6 °C, respectively. The waiting time of this test case allows the transient conduction heat transfer to diminish after the bubble departure, similar to the results shown in Figure 7-16. However, the growth time (5.79 ms) and bubble size (798 μm) are both larger than those of the Demiray and Kim (2002). The bubble growth time and size in Demiray and Kim (2002) result are about 4.3 ms and 600 μm, respectively. Although part of this difference is due to the higher surface temperature of the test case No. 5, subcooling effect can be considered as an important factor for this difference (note that liquid in Demiray and Kim (2002) test is 4.6 °C subcooled). For instance, comparison of test cases No. 2 and No. 6 shows that 5 °C subcooling reduced the bubble diameter form 848 μm to 644 μm and growth time from 8.9 ms to 6.8 ms. As can be seen in Table 6-2, the microlayer and transient conduction

heat transfer in test No. 5 are 35.8 μJ and 43.2 μJ, respectively (a total heat transfer of 79 μJ). The area under the heat transfer curve in Figure 7-16 gives an estimated value of approximately 60 μJ ($= 0.01W \times 6ms$) for total heat transfer through microlayer and transient conduction mechanisms. As can be seen, the results are fairly close. In terms of details, based on the test results of this study, their observed results can also be described as following.

1- The microlayer formation and evaporation has probably happened during the first half of the bubble growth time (for about 2 ms), as can be seen in all test cases shown in Appendix-B, particularly for test No. 5.

2- As can be seen in Appendix-B, a significant part of the transient conduction heat transfer occurs before the bubble departure. Therefore, part of the heat transfer curve shown in Figure 7-16 is likely associated with transient conduction heat transfer before bubble departure.

3- Considering the above two points, it is plausible that the transient conduction heat transfer from the wall is more significant than the microlayer heat transfer in the Demiray and Kim (2002) study. As can be seen in Table 6-2-b (note that microlayer energy is different than the microlayer heat transfer from the surface), transient conduction heat transfer is always higher than the microlayer evaporation heat transfer (almost twice in most cases).

The reader is referred to chapter 6 and Appendix-B for further details about the microlayer evaporation and transient conduction processes in terms of their occurrence time, their magnitude at every moment of time and any radius from the center of the bubble/surface contact area, and the overall area influenced by the two mechanisms.

Another area that should be compared between the two studies is the total surface heat transfer. Comparison of the two studies from this perspective is also quite significant, because as discussed from the beginning of this thesis, understanding the physics of heat transfer from the surface is a main objectives. Details of this comparison are provided in the following.

The heat transfer results of Figure 7-15 suggest that the slow varying mechanism of heat transfer observed in Demiray and Kim (2002) is the dominant mechanism of heat transfer from the surface, with an approximate heat flux of 3 W/cm^2 ($= 0.03W/0.01cm^2$). The heat transfer spikes are an insignificant component of the time-averaged surface heat transfer. Considering that the Demiray and Kim (2002) test was conducted at surface and liquid temperatures of 76 °C and 52 °C, respectively, a heat transfer coefficient of 1250 W/m^2°C ($= \frac{3W/cm^2}{24^\circ C}$) was determined. Demiray and Kim (2002) do not provide an account of heat loss through the substrate, so it is not possible to determine how much of this heat transfer is due to direct heat transfer to the liquid through the surface of the heater array. Nonetheless, this value of determined heat transfer coefficient seems to be too high for natural convection. Using the natural convection test results of Figure 6-28, a natural convection heat transfer coefficient of 259 W/m^2°C ($= \frac{0.62W/cm^2}{24^\circ C}$) was determined for the same surface and liquid temperature difference as of the Demiray and Kim (2002) study. This result seems to be more in line with the numerical simulation of Myers et al. (2005), in which they determined a natural convection heat transfer coefficient of 200 W/m^2°C. This suggests the possibility of a significant heat loss from

the surface. In order to determine the order of magnitude of the substrate heat loss, a numerical study was conducted. The details are discussed in the following.

The numerical model is a $3\times3\times0.5$ mm^2 square (the thickness of the quartz was assume 0.5 mm since no data was provided by Demiray and Kim (2002)) with a 1×1 mm^2 square area on top resembling the micro heater array. Adiabatic boundary conditions were applied on the four sides as well as on the backside of the model. Temperature boundary condition of 76 °C was applied to the heater array area. The heat transfer coefficient outside the heater was changed from 0 to 250 W/m^2°C in several different runs that were conducted. Figure 7-17 depicts the temperature distribution of the substrate for a representative case when a heat transfer coefficient 200 W/m^2°C is applied

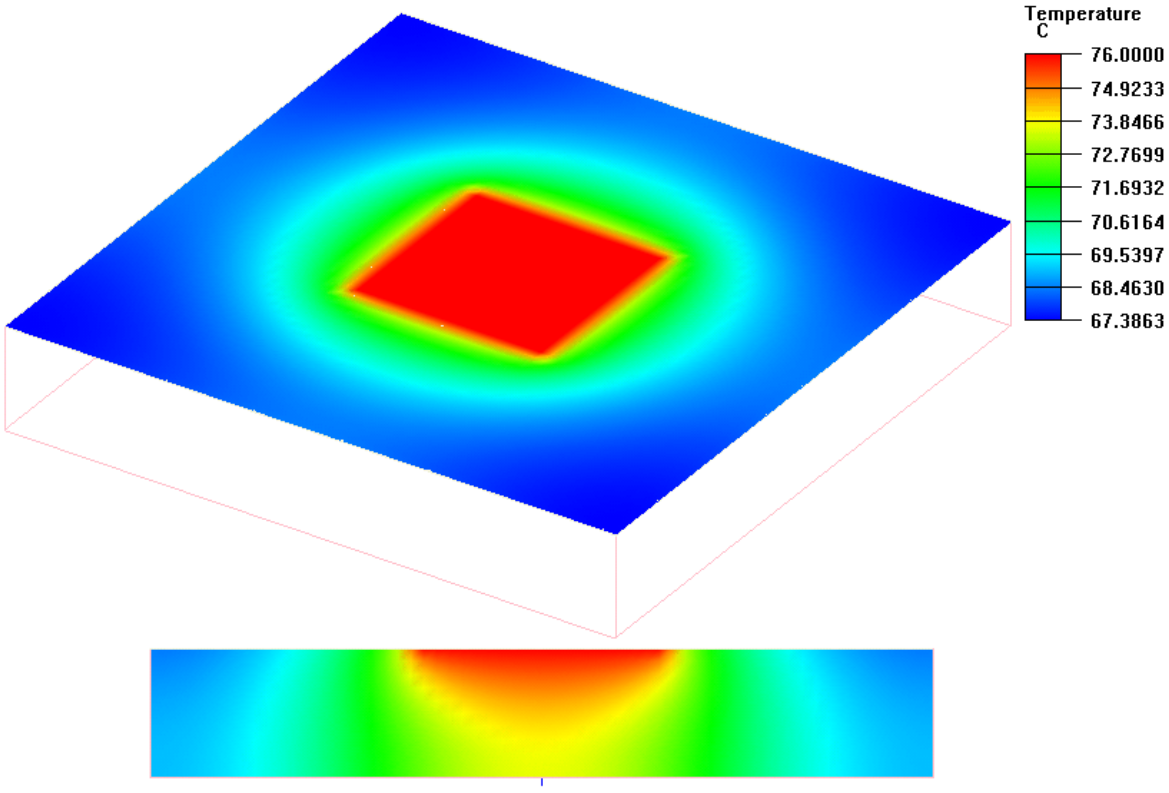

Figure 7-17: Numerical analysis of substrate heat loss in Demiray and Kim (2002) device.

outside the heater area. The numerical results for heat loss from the heater as a function of the heat transfer coefficient were determined. Figure 7-18 shows the results. As can be seen in the figure, heat loss from the heater array is in the same order of the reported heat dissipation from the surface. Although this shows a potential source of discrepancy between the results of the two studies, it does not allow proper comparison of the two, since an accurate account of heat loss from the surface can not be determined due to the fact that the boundary conditions outside the heater array in Demiray and Kim (2002) study are not precisely known.

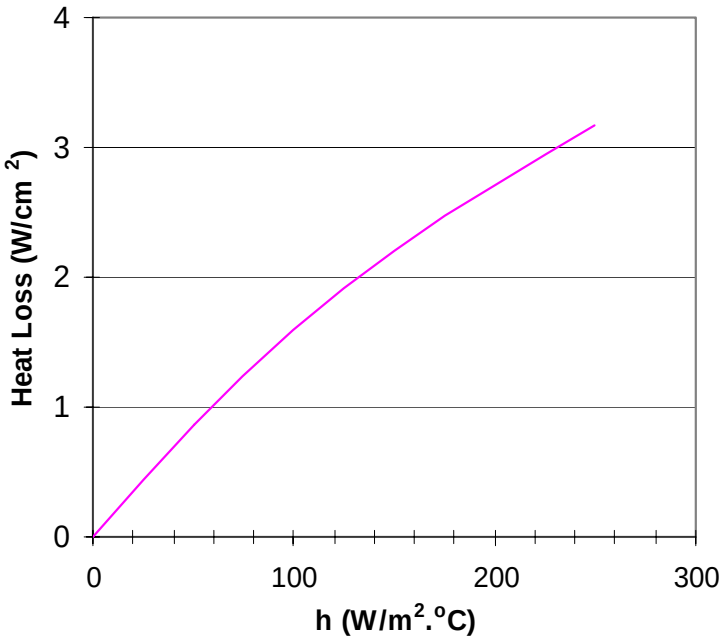

Figure 7-18: Substrate heat loss as a function of heat transfer coefficient outside the heater array area.

7-3-1-2- Demiray and Kim (2004)

The work of Demiray and Kim (2004) presented the experimental data of Demiray and Kim (2002) with an additional test at a lower subcooled temperature of 41 °C and the same surface temperature of 76 °C. The experimental results were processed in a similar procedure as in the Demiray and Kim (2002). Comparison of the Demiray and Kim

(2004) with the study of this thesis will be conducted from two perspectives 1) introduction of a new interpretation of the results reported in Demiray and Kim (2002) and 2) analysis of the Demiray and Kim (2002) finding about the role of microlayer in bubble growth.

Demiray and Kim (2004) derived a transient conduction model that could "track both the magnitude and trends of the measured data remarkably well" for some of their heaters. Figure 7-19 shows this comparison. Considering the similarities between their model and heat transfer from the heaters, they concluded that "transient conduction/and or microconvection was the dominant mechanism for bubble heat transfer". As discussed earlier, the study of this thesis suggested that both microlayer and transient conduction heat transfer mechanisms are active at the surface, but neither is dominant.

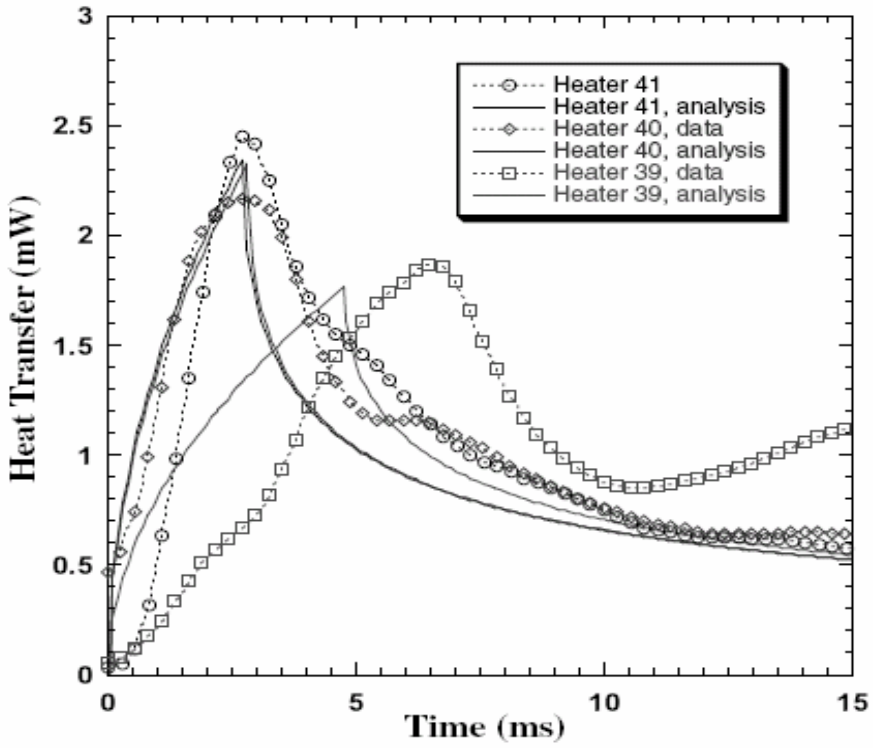

Figure 7-19: Comparison of transient conduction model with wall heat transfer data (Demiray and Kim (2004)).

In terms of the microlayer contribution to bubble growth, they considered bubble L5 with the growth rate shown in Figure 7-20. The bubble grew to a diameter of 0.5 mm during a time period of 0.54 ms. Demiray and Kim (2004) assumed a hemispherical shape for the bubble and determined an equivalent spherical diameter of 0.4 mm. This was found to be twice as large as the equivalent bubble diameter determined based on heat transfer from the surface during the same period, so it was argued that "wall heat transfer could have contributed at most $1/2^3$ or 12.5% of the energy required to produce the bubble". So, they concluded that "single bubbles departing the surface gained the majority of their energy from the superheated liquid layer and not from the wall". Results of test No. 5 of this thesis suggests a microlayer heat transfer from the wall of 12% during the bubble growth and total microlayer contribution of 17.9% to the bubble growth. Note that the difference between the two numbers is due to the initial sensible

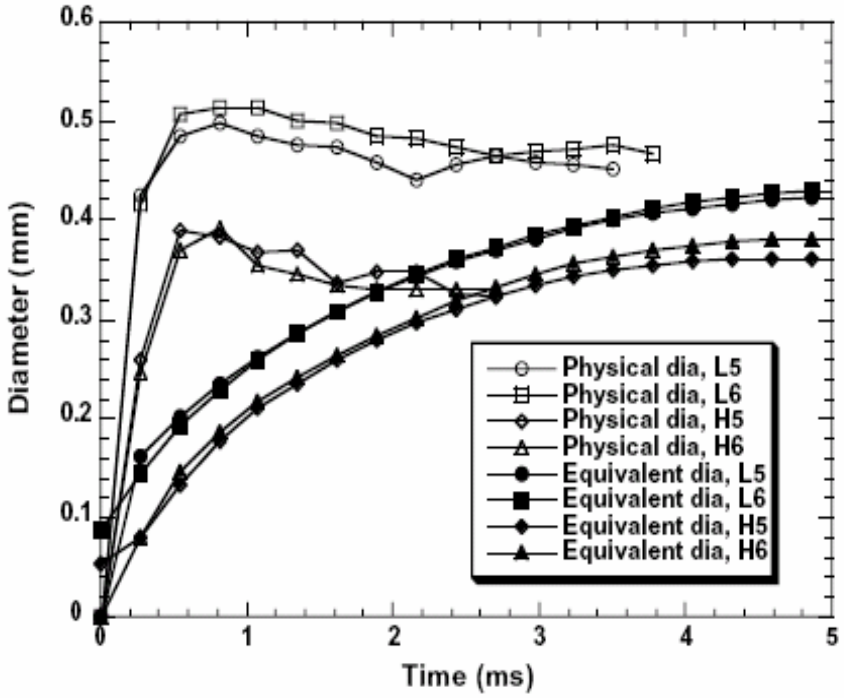

Figure 7-20: Comparison of physical and equivalent diameter (Demiray and Kim (2002)).

energy of the microlayer.

CHAPTER 8: CONCLUSIONS AND RECOMMENDATIONS

A novel MEMS device was developed to simultaneously measure the surface temperature and heat flux with an unprecedented resolution of 22-40 μm underneath a bubble. This was accomplished by design and fabrication of a composite wall with imbedded temperature sensors that take advantage of the unique thermal and microfabrication properties of Benzocyclobutene (BCB). This study provided unique microscale experimental data and enabled an accurate characterization of nucleation dynamics and microscale heat transfer processes during the heterogeneous nucleation process of FC-72 liquid.

The results allowed for the analysis of: 1) bubble growth dynamics and different mechanisms of heat transfer into the bubble and 2) vapor/liquid/surface thermal interactions and the bubble's role in heat transfer enhancement during the nucleation process. This was achieved through using the highly resolved temporal and spatial results determined for the surface temperature and heat flux along with the captured bubble images.

Using the temperature and heat flux results, the microlayer thickness/profile was determined. The average thickness of the microlayer was approximately between 1.6 to 3.7 μm for a surface temperatures range of 80 °C to 97 °C, respectively. Also, the microlayer contribution to the bubble growth was determined to increase from 14.7% to 22% over the same temperature range. Tests at other pressures are required to determine whether or not the microlayer thickness and its contribution to the bubble growth would further increase. A comparison between the test results and the existing bubble growth

models also indicated that models based on microlayer evaporation theory predict a completely different growth rate than what was observed in the experiment. Some of the models developed based on heat transfer from the superheated layer surrounding the bubble dome (the so called relaxation layer) were found to better match the experimental results. The test results of this study highlighted some of the weaknesses of the existing growth models and paved the way for development of new models. Considering that heat transfer to the bubbles for the test conditions of this study takes place mainly through relaxation layer, more attention should be paid to modeling of heat transfer to the relaxation layer. An example of such need was demonstrated in chapter 7 when Mikic and Rohsenow (1969) model was compared with the experimental results. As was shown, the model seemed to have the right mechanism for heat transfer to the bubble through the relaxation layer, but lacked a proper model for energy build up in the relaxation layer.

The transient conduction heat transfer mode was determined to predominantly occur at the bubble/surface contact area, and before the bubble departure, contrary to what has been commonly assumed in classical boiling models. The diameter of the contact area was found to be approximately half of the bubble diameter. Also, contrary to some of the existing knowledge in the boiling literature, transient conduction was not found to generally be the dominant mechanism of heat transfer from the surface. In terms of modeling, although heat transfer through the transient conduction mode has shown some similarities to the predictions of the governing equation for transient conduction heat transfer in solids, caution should be exercised when this model is used in liquids. Unlike in solids, conduction is not the only mechanism of heat transfer through an infinite thickness of a liquid body. Above a finite thickness into the liquid (boundary

layer), convection controls the heat transfer rate.

The high resolution (spatially) results for heat flux allowed for the clear distinction between convection heat transfer outside the contact area and the combined microlayer evaporation and the transient conduction heat transfer modes within the contact area. The test results indicated that at low surface temperatures, convection heat flux outside the contact area is relatively close to that of the natural convection, but it becomes significantly stronger than natural convection at higher surface temperatures. This mode of heat transfer has been commonly called microconvection, but often together with the transient conduction mode as an analogy for the sole mechanism of heat transfer from the surface. Due to the convective nature of this mechanism of heat transfer (as driven by the bubbles), use of forced convection heat transfer models may represent an avenue to explore improvement of modeling this heat transfer mode. However, the proper choice of characteristic length and velocity requires a careful investigation.

The test results of this study allowed for the first time, the measurement of the exact contribution of the different mechanisms of heat transfer from the surface. These results suggested that the contributions of all mechanisms of heat transfer from the surface are significant. Test results under saturation conditions showed that when surface temperature is increased from 80 °C to 97 °C, the contribution of the different mechanisms of heat transfer over a circular area with a diameter equal to that of the bubble changes from: 1) 28.8% to 16.3% for microlayer, 2) 45.3% to 32.1% for transient conduction, and 3) 25.8% to 51.6% for microconvection. The surface heat transfer results were compared with the existing models and it was determined that none of the existing models based on a single heat transfer mode could predict the heat transfer results. The

results suggested that new models that take into account the simultaneous contribution of different heat transfer mechanisms should be developed.

In addition to different heat transfer aspects of the nucleation process that motivated this study, a few other aspects of the bubbling dynamics of FC-72 were revealed. It was determined that bubble departure diameter can be predicted fairly closely using liquid properties and $Ja\left(=\frac{\rho_l c_l\left(T_w - T_{sat}\right)}{\rho_v h_{fg}}\right)$ number. A major source of error in predicting the bubble departure diameter was found to be the exponent of Ja number in the models. A close agreement between the experimental results and those models that use an exponent of close to 0.5 was determined. It was also determined that although the bubble departure diameter (D_b) and frequency (f) significantly vary with surface and liquid temperatures, the product of the two parameters ($D_b f$) remains almost constant. The magnitude of this parameter was found to be fairly predictable using the liquid properties.

The device developed in this study can be used to test other liquids, depending on the compatibility of the liquid with the materials of the device. Tests on a wide range of liquid properties, liquid temperature and pressure, and surface temperature would allow for the development of more generally universal models for bubble growth and heat transfer from the surface during the boiling process.

Appendix-A

MICROFABRICATION OF THE 1ST GENERATION DEVICE

The sensor substrate was fabricated from n-type <100> silicon wafers (1-3 Ω-cm) with a thickness of 300 μm. A layer of thermal oxide was grown (0.3 μm thick), followed by deposition of a LPCVD low stress stoichiometric silicon nitride layer (0.15 μm thick) on both sides of the wafer by the vender. Figure A-1 shows the fabrication sequence of the device. First, the backside of the wafer was patterned with photoresist to define the membrane area. The exposed area of the nitride layer was then etched using Reactive Ion Etching (RIE) with CF_4+O_2 gas. Photoresist was used as a protection mask for the front side of the wafer. It was imperative to keep the nitride layer on the front side of the wafer intact, as this is the side eventually to be immersed in the liquid. Even sub-micrometer size pits on the front side of the final device could serve as a cavity, and hence result in a source of bubbling in an undesirable location. The exposed oxide layer, underneath the nitride, was then etched in BOE. The patterned area (exposed silicon) was then anisotropically etched in 25% KOH solution at 80 °C to make a 30 μm thick 3.6×3.6 mm^2 square-shape membrane.

a) Thermal oxide growth and nitride deposition

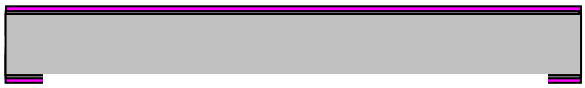

b) Pattern the nitride and oxide layers

c) Anisotropic etching of the membrane

d) Grow a layer of oxide

e) Deposition of Cr, Pt, and Au and lift-off

f) Etch the Au layer from within the sensor area

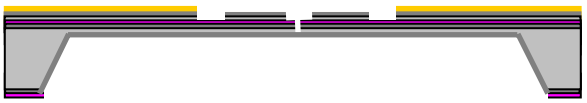

g) Pattern the cavity, etch nitride, oxide, and DRIE

h) Deposit Cr and Au on the backside of the membrane using shadow mask

Figure A-1: Fabrication sequence of the 1st generation device.

The sensor array was then fabricated on the frontside of the membrane through lift-off process and using a second mask. The metalization layer of the sensor array consists of three layers including 5 nm Cr, 20 nm Pt, and 1000 nm Au. A third mask was then used to pattern a layer of photoresist to etch the Au layer from within the sensor area. Table A-1 gives the radial position of the sensors. A fourth mask was used to pattern a 3 μm cavity at the center of the sensor array. The nitride and oxide layers at the patterned area were etched away, and a 25-μm deep cavity was etched into the silicon membrane using DRIE.

The last step was to fabricate the heater on the backside of the membrane. First, a 0.3-μm thick aluminum oxide (alumina) layer was deposited on the backside of the

membrane to provide electrical insulation. A 100-nm thick Cr layer was vapor deposited on the backside of the membrane using a shadow mask. A second shadow mask was used to deposit a 1000-nm thick layer of Au on the two sides of the Cr film, leaving an area of 3×3 mm^2 at the center of the membrane free of Au. The Au layer significantly reduced the resistance and thereby diminished the heat release at the Au coated area. The Au layer also provided bond pad areas to which the heater wires could be soldered.

Table A-1: Radial position of the sensors

Sensor	**R_{in} (μm)**	**R_{out} (μm)**
S-1	25	66
S-2	76	100
S-3	110	134
S-4	144	185
S-5	195	236
S-6	246	270
S-7	280	304
S-8	314	338
S-9	348	372
S-10	382	406
S-11	416	440
S-12	450	474
S-13	484	491

Appendix-B

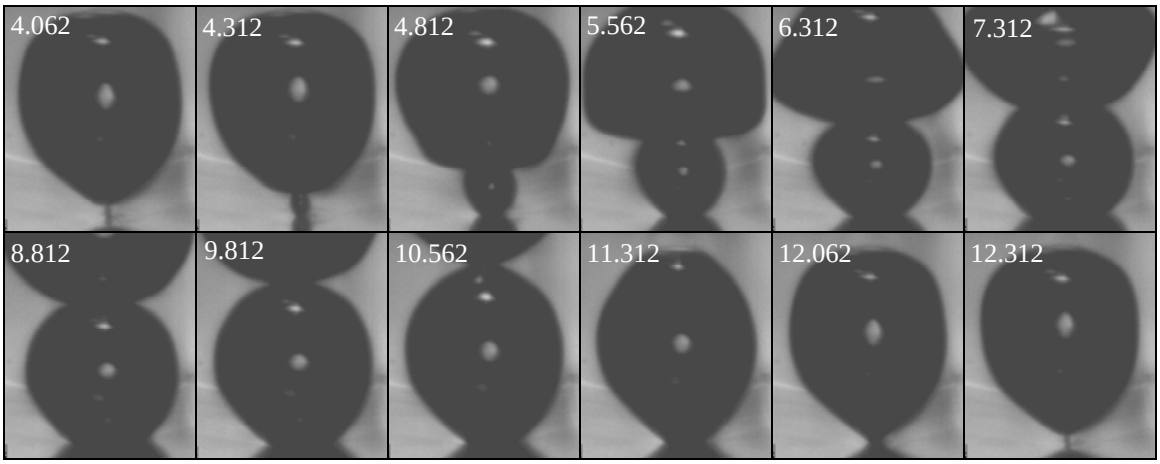

a- Images of a bubbling event during the time period of t=4.062 ms and t=12.312 ms

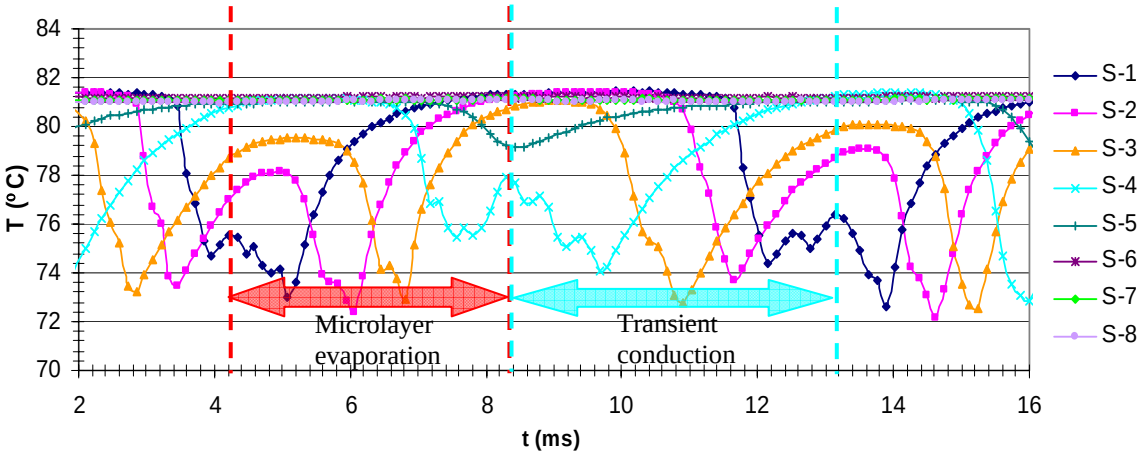

b- Temperature data corresponding to the bubbling event shown in (a)

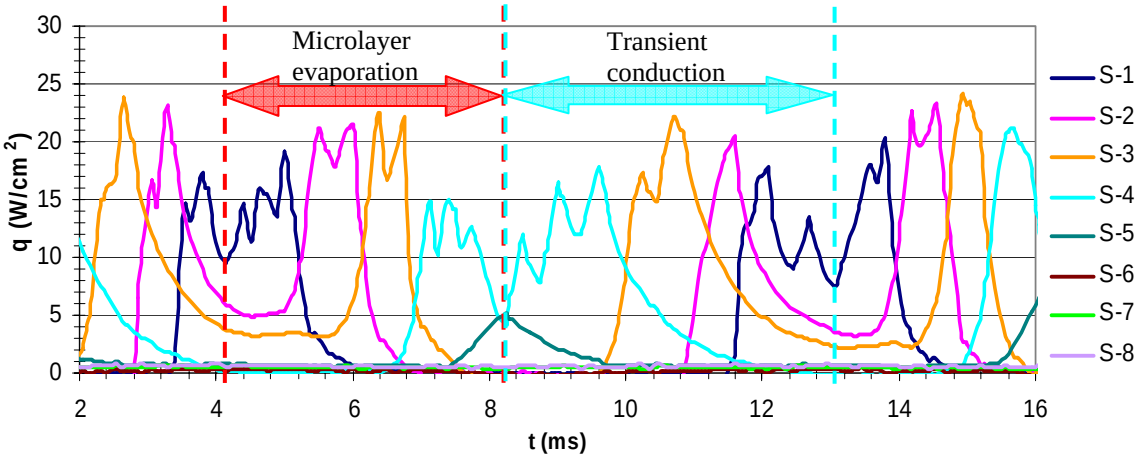

c- Heat flux results corresponding to the bubbling event shown in (a)

Figure B-1: Bubble images and surface temperature and heat flux at an average surface temperature of 80.5 ºC and a liquid temperature of 56.7 ºC (Test No. 1).

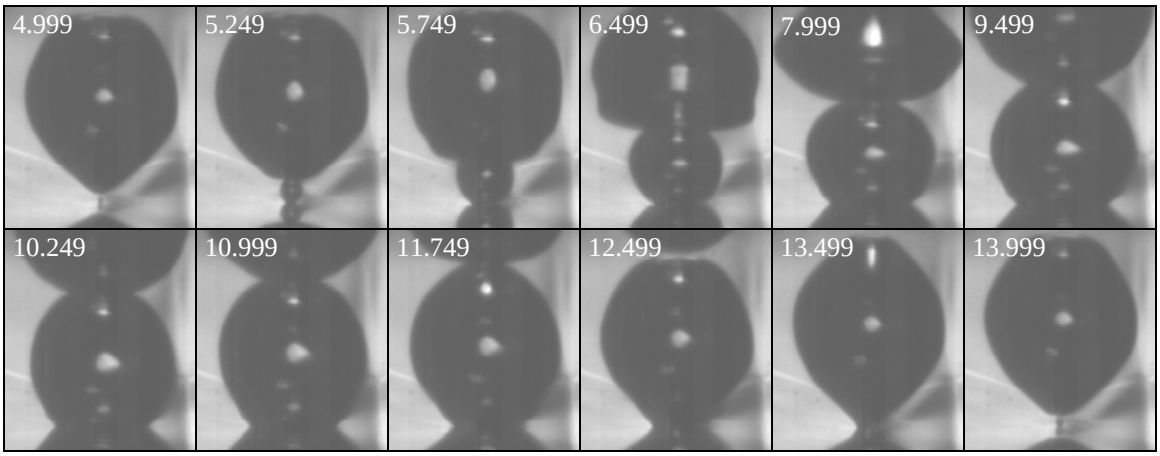

a- Images of a bubbling event during the time period of t=4.999 ms and t=13.999 ms

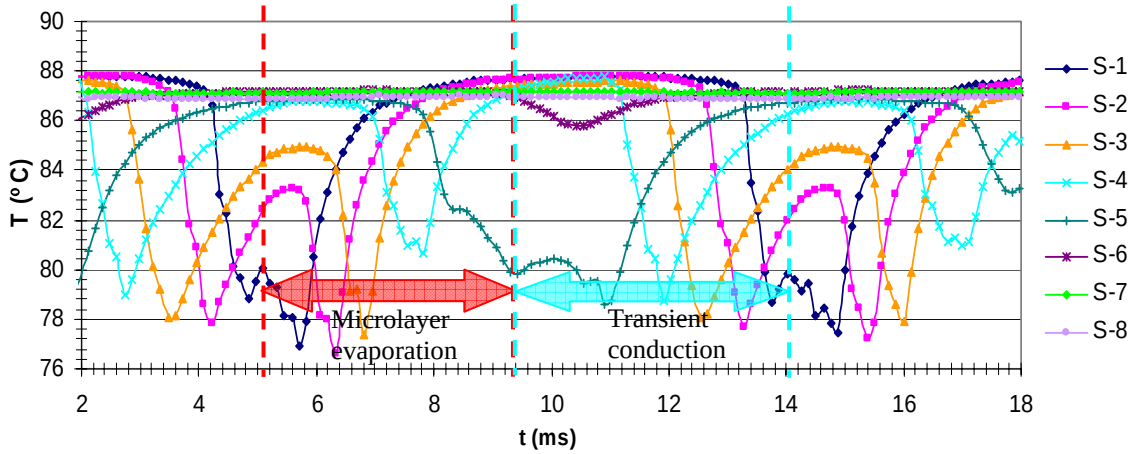

b- Temperature data corresponding to the bubbling event shown in (a)

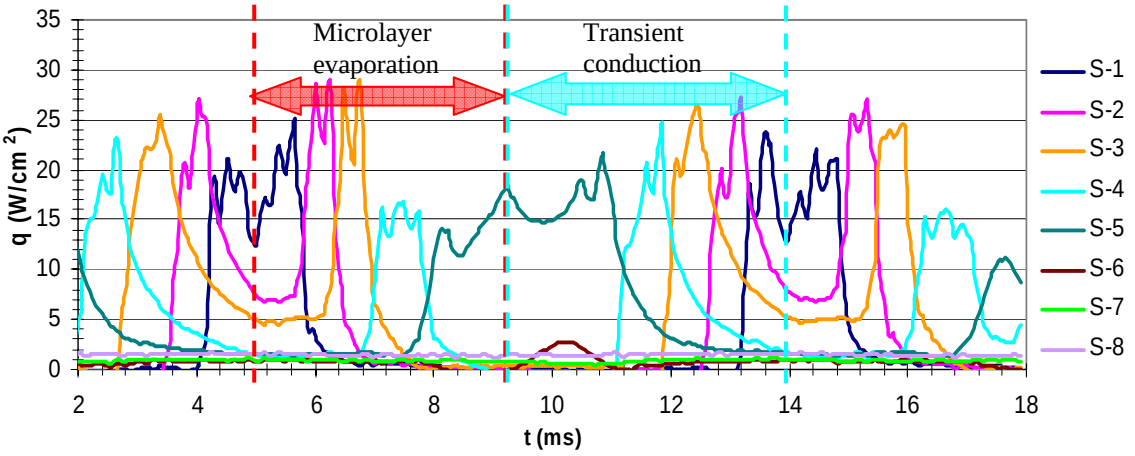

c- Heat flux results corresponding to the bubbling event shown in (a)

Figure B-2: Bubble images and surface temperature and heat flux at an average surface temperature of 86.4 ºC and a liquid temperature of 56.7 ºC (Test No. 2).

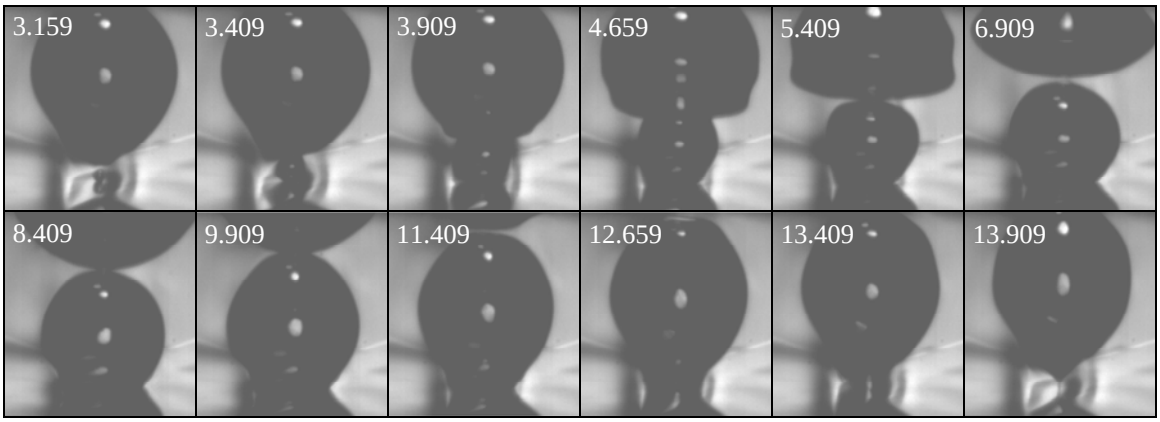

a- Images of a bubbling event during the time period of t=3.159 ms and t=13.909 ms

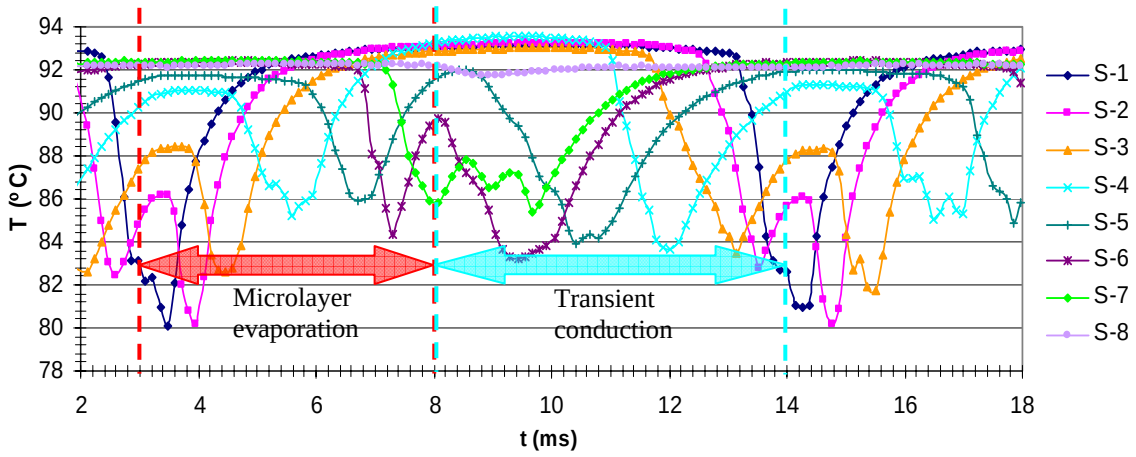

b- Temperature data corresponding to the bubbling event shown in (a)

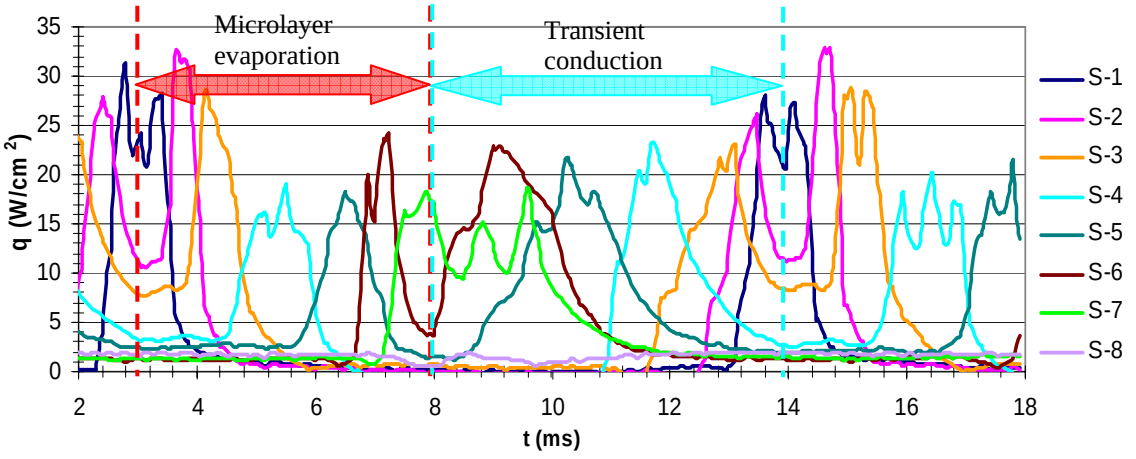

c- Heat flux results corresponding to the bubbling event shown in (a)

Figure B-3: Bubble images and surface temperature and heat flux at an average surface temperature of 91.4 ºC and a liquid temperature of 56.7 ºC (Test No. 3).

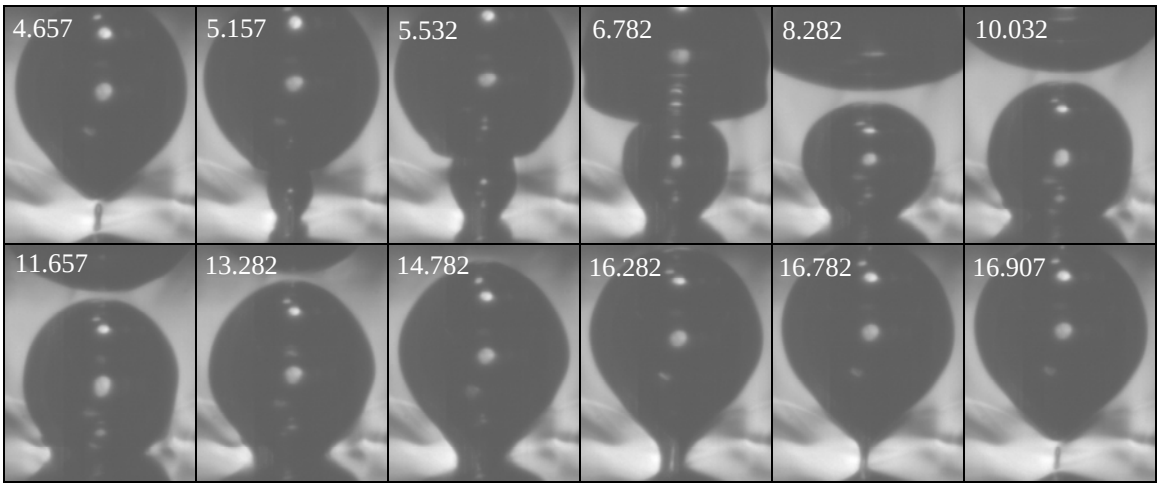

a- Images of a bubbling event during the time period of t=4.657 ms and t=16.907 ms

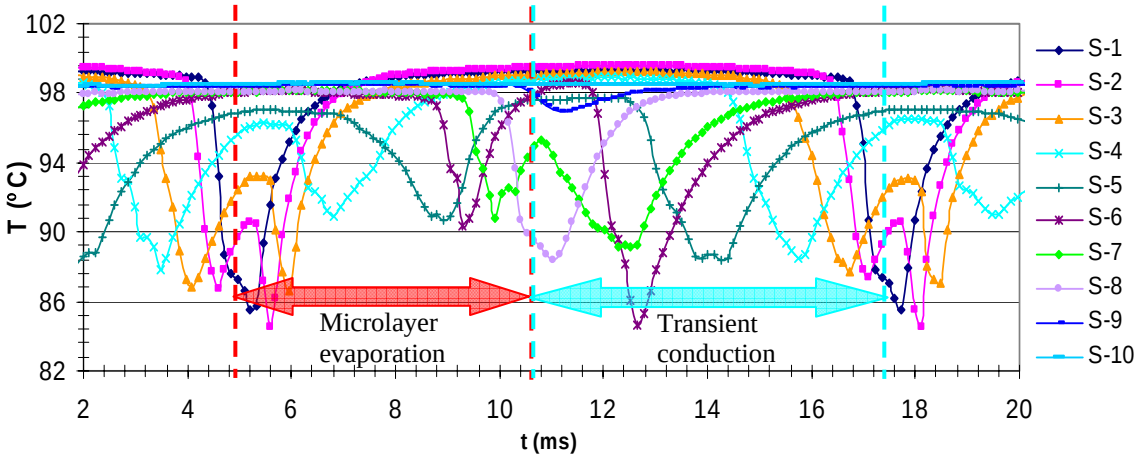

b- Temperature data corresponding to the bubbling event shown in (a)

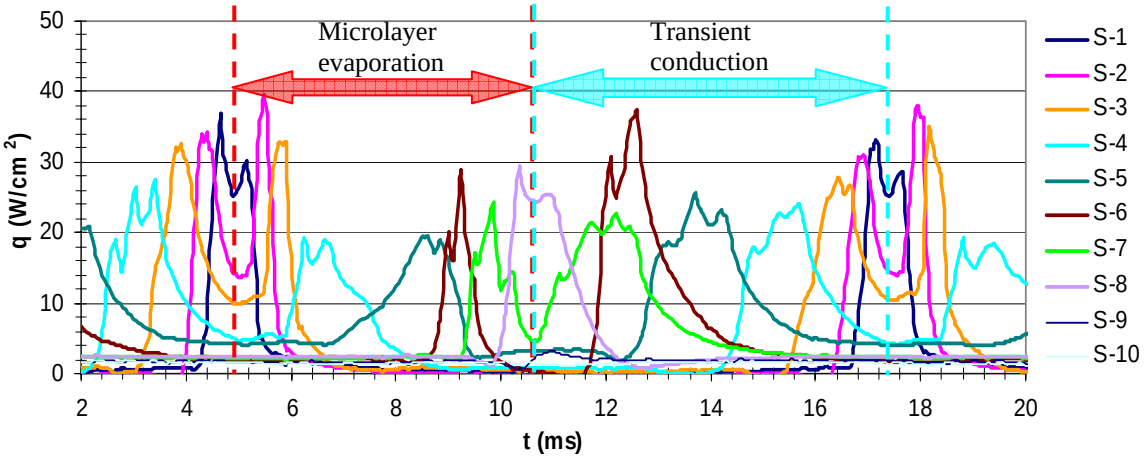

c- Heat flux results corresponding to the bubbling event shown in (a)

Figure B-4: Bubble images and surface temperature and heat flux results at an average surface temperature of 97.2 ºC and a liquid temperature of 56.7 ºC (Test No. 4).

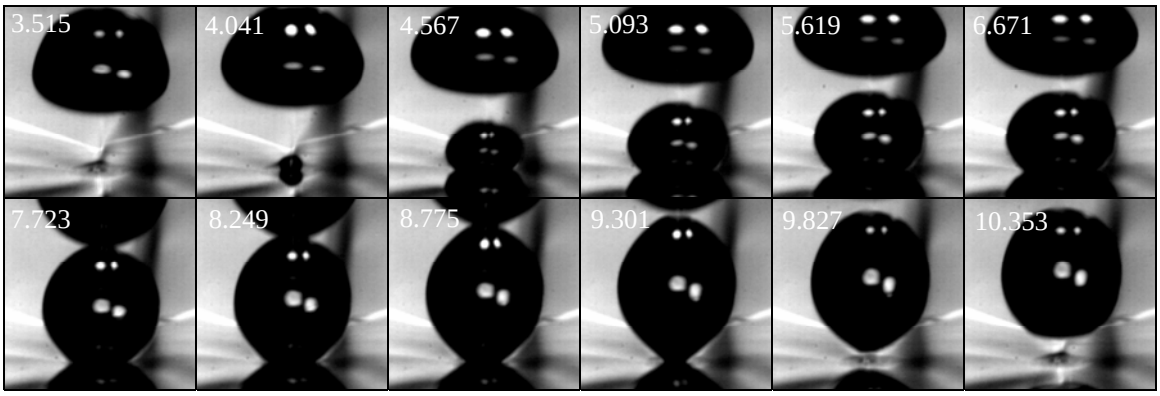

a- Images of a bubbling event during the time period of t=3.515 ms and t=10.353 ms

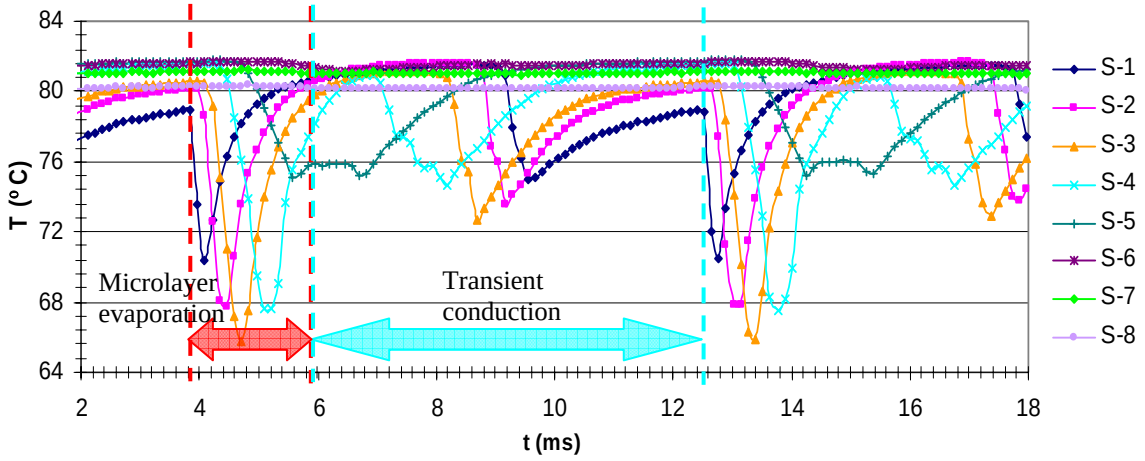

b- Temperature data corresponding to the bubbling event shown in (a)

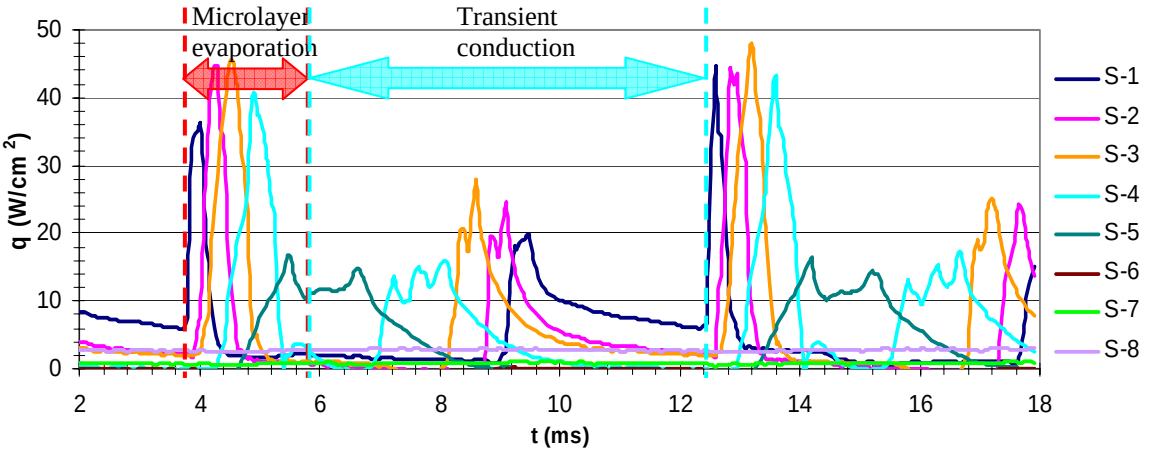

c- Heat flux results corresponding to the bubbling event shown in (a)

Figure B-5: Bubble images and surface temperature and heat flux at an average surface temperature of 80.2 ºC and a liquid temperature of 56.7 ºC (Test No. 5).

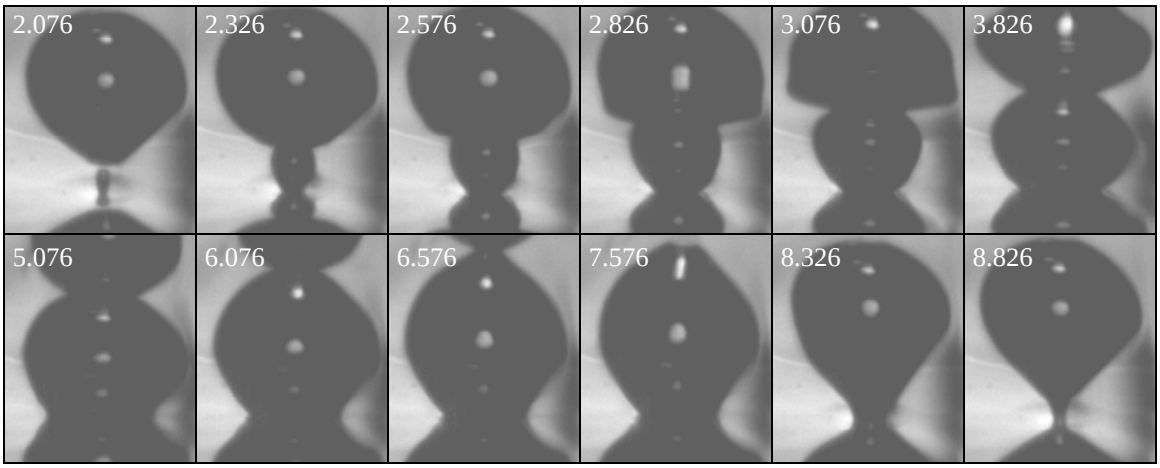

a- Images of a bubbling event during the time period t=2.076 ms and t=8.826 ms

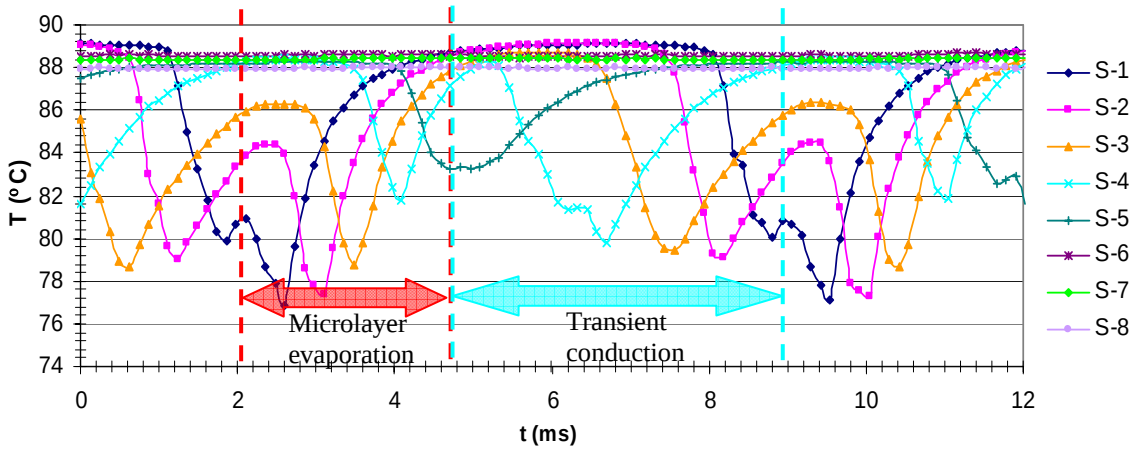

b- Temperature data corresponding to the bubbling event shown in (a)

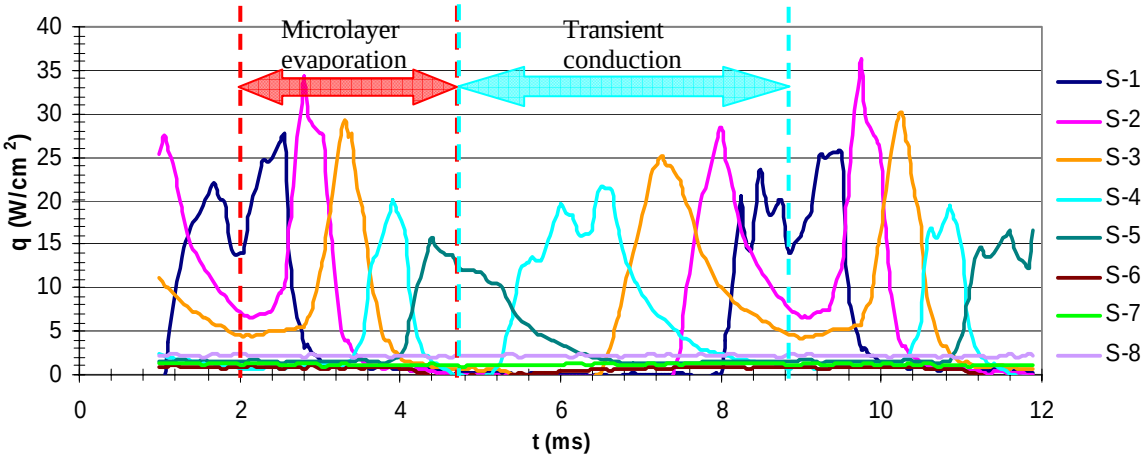

c- Heat flux results corresponding to the bubbling event shown in (a)

Figure B-6: Bubble images and surface temperature and heat flux at average surface temperature of 87.5 ºC and liquid temperature of 51.5 ºC (5.2 ºC subcooled, Test No. 6).

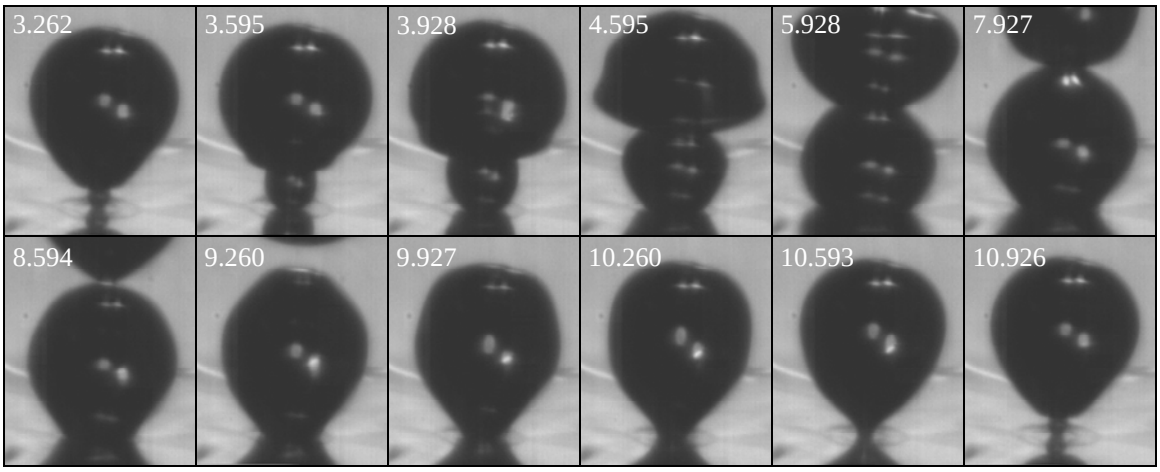

a- Images of a bubbling event during the time period of t=3.262 ms and t=10.926 ms

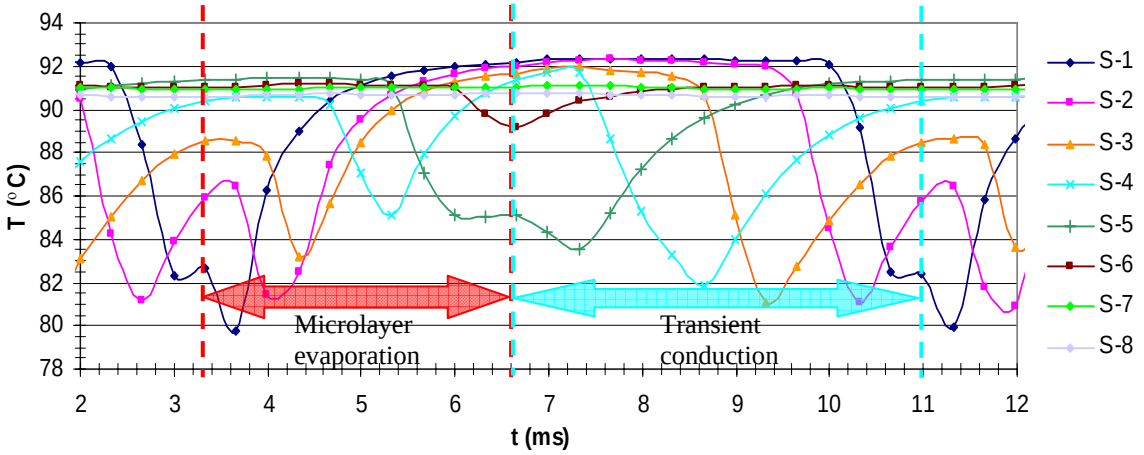

b- Temperature data corresponding to the bubbling event shown in (a)

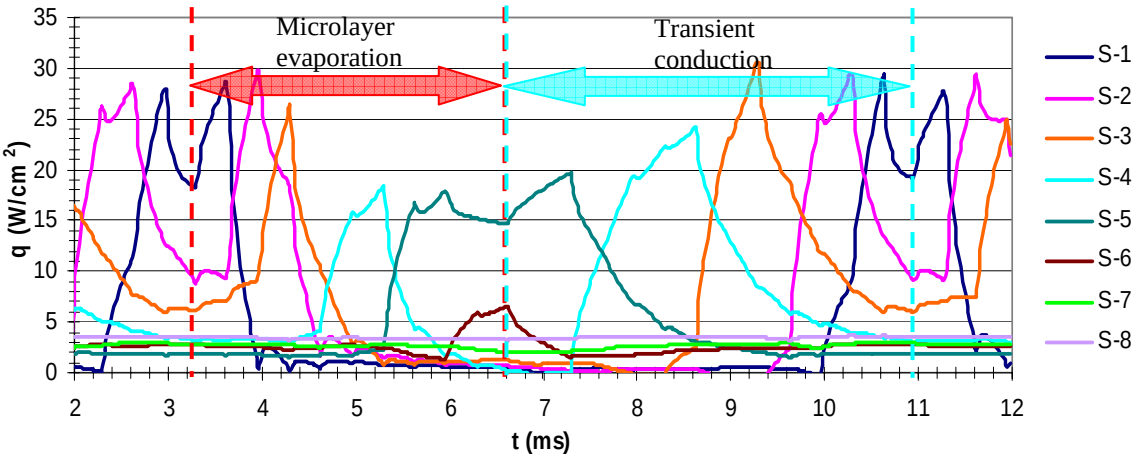

c- Heat flux results corresponding to the bubbling event shown in (a)

Figure B-7: Bubble images and surface temperature and heat flux at average surface temperature of 90.1 ºC and liquid temperature of 52.7 ºC (4.0 ºC subcooled, Test No. 7).

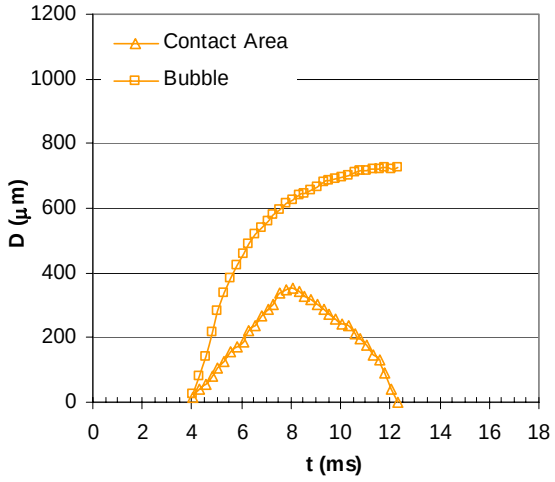

a- Test No. 1

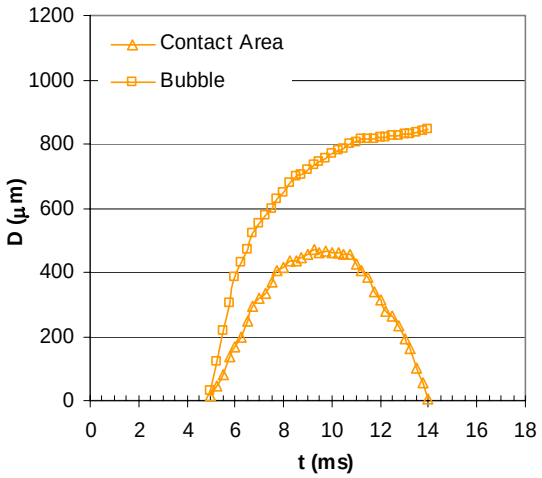

b- Test No. 2

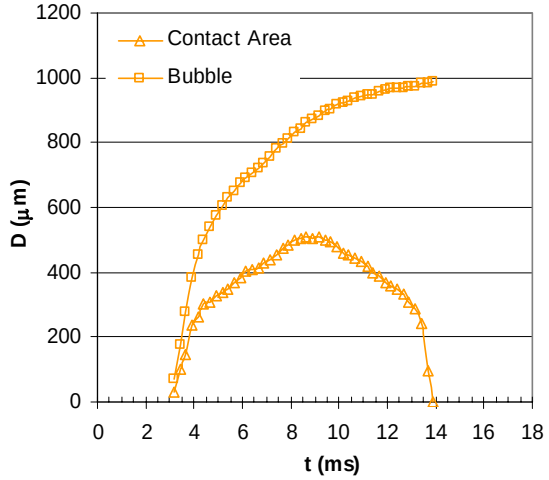

c- Test No. 3

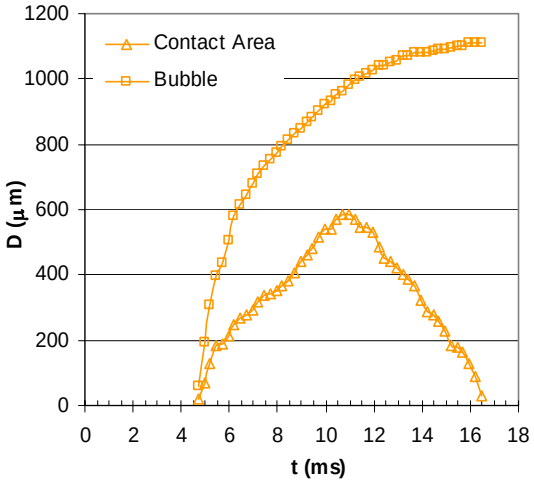

d- Test No. 4

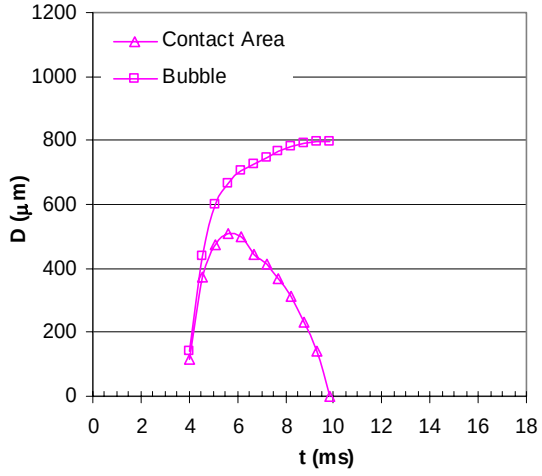

e- Test No. 5

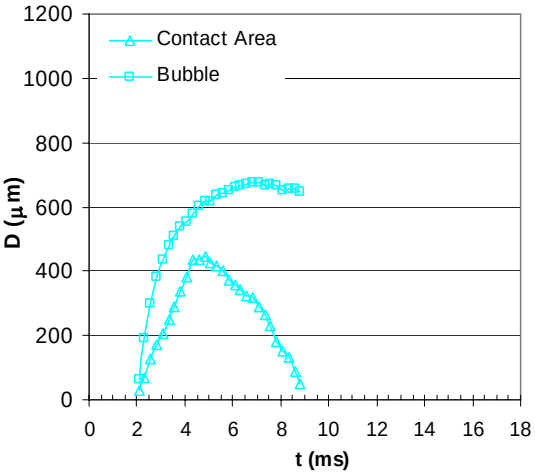

f- Test No. 6

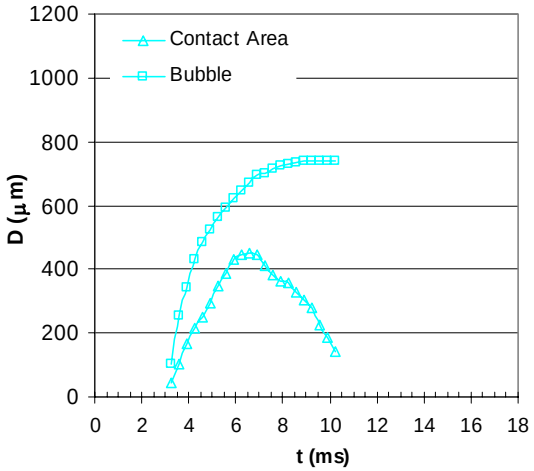

g- Test No. 7

Figure B-8: Diameter of contact area and bubble at different experimental conditions.

References:

Bankoff, S.G. (1958). "Entrapment of Gas in the Spreading of a Liquid Over a Rough Surface." AIChE J. **4**: 24-26.

Bankoff, S. G., Mikesell, R. D. (1958). Growth of Bubbles in Liquid of Initially Nonuniform Temperature. ASME Meeting Nov 30-Dec 5: 58-A105.

Bosnjakovic, F. (1930). "Verdampfung und Flussigkeitsuberhitzung." Tech. Mech. Thermodyn. Bevl. **1**: 358-362.

Carey, V. P. (1992). Liquid-Vapor Phase-Change Phenomena: An Introduction to the Thermophysics of Vaporization and Condensation Processes in Heat Transfer Equipment. Taylor & Francis, Hebron, KY.

Carslaw, H. S., and Jaeger, J. C. (1959). Conduction of Heat in Solids. 2nd ed. Oxford University Press, Oxford.

Clark, H.B., Strenge, P.H., and Westwater, J.W. (1958). Active Sites for Nucleate Boiling. AIChE-ASME Heat Transfer Conference, Preprint No. 13, Chicago, IL, USA.

Cole, R. (1960). "Photographic Study of Boiling in the Region of Critical Heat Flux." AIChE J. **6**: 533-542.

Cole, R., and Shulman, H. L. (1966). "Bubble Departure Diameters at Subatmospheric Pressures." Eng. Prog. Symp. Ser. **62**(64): 6-16.

Cooper, M. G. (1969). "The Microlayer and Bubble Growth in Nucleate Pool Boiling." Int. J. Heat Mass Transfer. **12**: 915-933.

Cooper, M. G., and Lloyd, A. J. P. (1969). "The Microlayer in Nucleate Pool Boiling." Int. J. of Heat Mass Transfer. **12**: 895-913.

Cornwell, K. (1977). "Naturally formed boiling site cavities." Letters in Heat and Mass Transfer. **4**: 63-71.

Cornwell, K. (1982). "On boiling due to contact angle hysteresis." Int. J. Heat Mass Transfer. **25:** 205-211.

Corty, C., Foust, A.S. (1955). "Surface Variables in Nucleate Boiling." Chem. Eng. Prog. Symp. Ser. **51:** 1-12.

Dalle Donne, M., and Ferranti, M. P. (1975). "The Growth of Vapor Bubbles in Superheated Sodium." Int. J. Heat mass Transfer. **18**: 477- 493.

Demiray, F., and Kim, J. (2002). Heat Transfer from a Single Bubble Nucleation Site During Saturated Pool Boling of FC-72 Using an Array of 100 Micron Heaters. 8th AIAA/ASME Joint Thermophysics and Heat Transfer Conference, Missouri, USA.

Demiray, F., and Kim, J. (2004). "Microscale Heat Transfer Measurements during Pool Boiling of FC-72: Effect of Subcooling." Int. J. of Heat Mass Transfer. **47**: 3257-3268.

Dergarabedian, P. (1953). "The Rate of Growth of Vapor Bubbles in Superheated Water." J. Appl. Mech. **20**: 537-574.

Forster, H. K., and Zuber, N. (1955). "Dynamic of Vapor Bubbles and Boiling Heat Transfer." AIChE J. **1**: 531-539.

Forster, H. K., and Greif, R. (1959). "Heat Transfer to a Boiling Liquid-Mechanism and Correlations." J. of Heat Transfer. **81**: 43-54.

Forester, H. K., and Zuber, N. (1954). "Growth of Vapor Bubbles in Superheated Liquid." J. Appl. Phys. **25**: 474- 478.

Forester, H. K., and Zuber, N. (1955). "Dynamics of Vapor Bubbles and Boiling Heat Transfer." Amer. Inst. Chem. Engrs. J. **1**: 531-535

Fritz, W., and Ende, W. (1936). "Verdampfungsvorgang nach Kinematographischen Aufnahmen und Dampfblasen." Phys. Z. **37**: 391.

Graham, R. W., and Hendricks, R. C. (1967). "Assessment of Convection and Evaporation in Nucleate Boiling." NASA TN D-3943.

Griffith, P. (1958). "Bubble Growth Rates in Boiling." J. Heat Transfer. **80**: 721-726.

Guo, Z., and El-Genk, M. (1994). "Liquid Microlayer Evaporation During Nucleate Boiling on the Surface of a Flat Composite Wall." Int. J. Heat Mass Transfer. **37**: 1641-1655.

Han, C., and Griffith, P. (1965). "The Mechanism of Heat Transfer in Nucleate Pool Boiling." Int. J. of Heat Mass Transfer. **8**: 905-913.

Hendricks, R C., and Sharp, R. R. (1964). "Initiation of Cooling Due to Bubble Growth on a Heating Surface." NASA TN D-2290.

Hospeti, N. B., and Mesler, R. B. (1965). "Deposits Formed Beneath Bubbles During Nucleate Boiling of Radioactive Calcium Sulfate Solutions." AIChE J. **11**: 662-665.

Hsu, S. T., and Schmidt, F. W. (1961). "Measured Variations in Local Surface Temperatures in Pool Boiling of Water." J. Heat Transfer. **83**: 245-254.

Hsu, Y.Y. (1962). "On the Size Range of Active Nucleation Cavities on a Heating Surface." J. Heat Transfer. **84**: 207-215.

Ivey, H. J. (1967). "Relationships between Bubble Frequency, Departure Diameter and Rise Velocity in Nucleate Boiling." Int. J. Heat Mass Transfer. 10: 1023-1040.

Jakob, M., and Fritz, W. (1931). "Frosh. Geb. Ingenieurwes." **2**: 434.

Jakob, M., and Linke, W. (1935). "Boiling Heat Transfer." Phys. Z. **636**: 267-273.

Jawurek, H. H. (1969). "Simultaneous Determination of Microlayer Geometry and Bubble in Nucleate Boiling." Int. J. of Heat Mass Transfer. **12**: 843-848.

Jenson, M. K., and Memmel, G. J. (1986). Evaluation of Bubble Departure Diameter Correlations. Proc. 8th Int. Heat Transfer Conf. 4: 1907-1912.

Johnson, M. A., De La Pena, J., Mesler, R. B. (1966). "Bubble Shapes in Nucleate Boiling." AIChE J. **12**: 344-348.

Judd, R. L., and Hwang, K. S. (1976). "A Comprehensive Model for Nucleate Pool Boiling Heat Transfer Including Microlayer Evaporation." J. Heat Transfer. **98**: 623-629.

Katto, Y., Yokoya, S. (1966). "Experimental Study of Nucleate Pool Boiling in Case of Making Interference-Plate Approach to Heating Surface." International Heat Transfer Conference – Proceedings. **3**: 219-227.

Kutateladze, S. S., and Gogonin, I. I. (1979). "Growth Rate and Detachment Diameter of a Vapor Bubble in Free Convection Boiling of a Saturated Liquids." High Temperature. **17**: 667-671.

Lee, H. S., and Merte, H. (1996). "Spherical Vapor Bubble Growth in Uniformly Superheated Liquids." Int. J. Heat Mass Transfer. **39**: 2427-2447.

Lien, Y. (1969). Bubble Growth Rates at Reduced Pressure. Sc.D. Thesis, Mech. Eng. Dept., M.I.T.

Malkus, W. R. (1954). "Discrete Transition in Turbulent Convection," Proc. Roy. Soc. **A. 225**: 185-195.

Malkus, W. R. (1954). "The Heat Transport and Spectrum of Thermal Turbulence," Proc. Roy. Soc. A. **225**: 196-205.

Mann, M., Stephan, K., Stephan, P. (2000). "Influence of Heat Conduction in the Wall on Nucleate Boiling Heat Transfer," Int. J. of Heat Mass Transfer. **43**: 2193-2203.

Mei, R., Chen, W., and Klausner, J. F. (1995). "Vapor Bubble Growth in Heterogeneous Boiling-I. Formulation." Int. J. of Heat Mass Transfer. **38**: 909-919.

Mei, R., Chen, W., and Klausner, J. F. (1995). "Vapor Bubble Growth in Heterogeneous Boiling-II. Growth Rate and Thermal Fields," Int. J. of Heat Mass Transfer. **38**: 921-934.

Merte, H., Lee, H. S., Keller, R. B. (1995). Pool Boiling Experiment Flown on STS-47-57-60, Report No. UM-MEAM-95-01. Dept. of Mech. Eng. and Appl. Mechanics, The University of Michigan, Ann Arbor, MI.

Mikic, B. B., and Rohsenow, W. M. (1969). "A New Correlation of Pool-Boiling Data Including the Effect of Heating Surface Characteristics," J. of Heat Transfer. **91**: 245-250.

Mikic, B. B., and Rohsenow, W. M. (1969). "Bubble Growth Rates in Non-Uniform Temperature Field," Prog. Heat Mass Transfer. **2**: 283-292.

Mikic, B. B., Rohsenow, W. M., and Griffith, P. (1970). "On Bubble Growth Rates." Int. J. of Heat Mass Transfer. **13**: 647-666.

Mitrovic, J. (2002). "On the Profile of the Liquid Wedge Underneath a Growing Vapor Bubble and the Reversal of the Wall Heat Flux." Int. J. Heat Mass Transfer. **45:** 409-415.

Moghaddam, S., Ohadi, M., Qi, J. (2003). Pool Boiling of Water and FC-72 on Copper and Graphite Foams. Proceedings of ASME InterPACK'3 International Electronic Packaging Technical Conference and Exhibition. Maui, Hawaii, July 6-11.

Moore, F. D., and Mesler, R. B. (1961). "The Measurement of Rapid Surface Temperature Fluctuation During Nucleate Boiling of Water." AIChE J. **7**: 620-624.

Murali, V., Gasparek, M., Bhansali, A., Chen, S. H., Dias, R., (1992). Wire Bonding of Aluminum/Polyimide Multi-layer Structures. Proceedings of the 30th Annual International Reliability Physics Symposium, San Diego, CA, USA.

Peebles, F. N., and Garber, H. J. (1953). "Studies on Motion of Gas Bubbles in Liquids." Chem. Eng. Prog. **49**: 88-97.

Pinel, S., Marty, A., Tasselli, J., Bailbe, J. P., Beyne, E., Van Hoof, R., Marco, S., Morante, J. R., Vendier, O., and Huan, M. (2002)."Thermal Modeling and Management in Ultrathin Chip Stack Technology." IEEE Transactions on Components and Packaging Technologies. **25**(2): 244-253.

Plesset, M. S. (1949). "The Dynamics of Cavitation Bubbles." J. Appl. Mech. **16**: 277-282.

Plesset, M. S., and Zwick, S. A. (1952). "A Nonsteady Heat Diffusion Problem with Spherical Symmetry." J. Appl. Phys. **23**: 95-98.

Plesset, M. S., and Zwick, S. A. (1954). "The Growth of Vapor Bubbles in Superheated Liquids." J. Appl. Phys. **25**: 493- 500.

Prosperetti, A., and Plesset, M. S. (1978). "Vapor-Bubble Growth in a Superheated Liquid." J. Fluid Mech. **85**: 349-368.

Rayleigh, L. (1917). "On the Pressure Developed in a Liquid During the Collapse of a Spherical Cavity." Phil. Mag. **34**: 94- 98.

Riznic, J., Kojasoy, G., and Zuber, N. (1999). "On the Spherically Symmetric Phase Change Problem." Int. J. Fluid Mech. Res. **26:** 110- 145.

Robinson, A. J., and Judd, R. L. (2001). "Bubble Growth in a Uniform and Spatially Distributed Temperature Field." Int. J. Heat Mass Transfer. **44**: 2699- 2710.

Rohsenow, W. M. (1951). "A Method of Correlating Heat Transfer Data for Surface Boiling of Liquids." ASME J. of Heat Transfer. **74**: 969-976.

Rohsenow, W. M. (1998). Handbook of Heat Transfer. McGraw-Hill, New York, 15-47.

Rogers, T. F., and Mesler, R. B. (1964). "An Experimental Study of Surface Cooling by Bubbles During Nucleate Boiling of Water." AIChE J. **10**: 656-660.

Savic, P. (1958). "Discussion on Bubble Growth Rates in Boiling." Int. J. Heat Mass Transfer. **80**: 726- 728.

Scriven, L. E. (1959). "On the Dynamics of Phase growth." Chem. Eng. Sci. **10**: 1-13.

Sharp, R. R. (1964). The Nature of Liquid Film Evaporation During Nucleate Boiling. NASA TN D-1997.

Schlichting, H. (1960). Boundary Layer Theory. McGraw-Hill, New York.

Shoji, M., and Takagi, Y. (2001). "Bubbling Features from a Single Artificial Cavity." Int. J. of Heat and Mass Transfer. **44**: 2763-76.

Shoukri, M., and Judd, R. L. (1975). "Nucleation Site Activation in Saturated Boiling." J. of Heat Transfer. **97**: 93-98.

Singh, A., Mikic, B. B., and Rohsenow, W. M. (1976). "Effect of Superheat and Cavity Size on Frequency of Bubble Departure in Boiling." J. of Heat Transfer. **99**: 401-406.

Son, G., Dhir, V. K., and Ramanujapu, N. (1999). "Dynamics and Heat Transfer Associated With a Single Bubble During Nucleate Boiling on a Horizontal Surface." J. of Heat Transfer. **121**: 623-631.

Theofanous, T. G., and Patel, P. D. (1976). "Universal Relations for Bubble Growth." Int. J. Heat Mass Transfer. **2**: 83-98.

Thomas, D. B., and Townsend, A. A. (1957). "Turbulent Convection Over a Heated Horizontal Surface." J. Fluid Mech. **2**: 473- 492.

Tien, C. L. (1962) "Hydrodynamic Model for Nucleate Pool Boiling." Int. J. of Heat Mass Transfer. **5**: 533-540.

Tong, W., Bar-Cohen, A., Simon, T.W., and You, S. M. (1990). "Contact Angle Effects on Boiling Incipience of Highly-Wetting Liquids." Int. J. of Heat and Mass Transfer. **33**: 91-103.

Torikai, K., Tamazaki, T. (1965). "Temporal Variation of Boiling Heat Transfer Caused by Generation of Bubbles." Japan Society of Mechanical Engineers – Bulletin. **8**: 669-676.

Townsend, A. A. (1959). "Temperature Fluctuation Over a Horizontal Heated Surface." J. Fluid Mech. **5**: 209-221.

Touloukian, Y. S. (1970). Thermophysical Properties of Matter-Volume 2. IFI/Plenum, New York.

Van Ouwerkerk, H. J. (1971). "The Rapid Growth of a Vapor Bubble at a Liquid-Solid Interface." Int. J. of Heat Mass Transfer. **14**: 1415-1431.

Van Stralen, S. J. D., Sohal, M. S., Cole, R., and Sluyter, W. M. (1975). "Bubble Growth Rates in Pure and Binary Systems: Combined Effect of Relaxation and Evaporation Microlayers." Int. J. Heat Mass Transfer. **18**: 453-467.

Westwater, J. W. (1959). "Boiling Heat Transfer." American Scientist. 427-446.

Zuber, N. (1963). "Nucleate Boiling- the Region of Isolated Bubbles - Similarity with Natural Convection." Int. J. of Heat Mass Transfer. **6**: 53-65.

Zuber, N. (1964). "Recent Trends in Boiling Heat Transfer Research. Part I: Nucleate Pool Boiling." Appl. Mech. Rev. **17**: 663-672.